

**COMPUTATIONAL AND RHEOLOGICAL STUDY OF WAX DEPOSITION
AND GELATION IN SUBSEA PIPELINES**

by

Hyun Su Lee

A dissertation submitted in partial fulfillment
of the requirements for the degree of
Doctor of Philosophy
(Chemical Engineering)
in The University of Michigan
2008

Doctoral Committee:

Professor H. Scott Fogler, Chair
Professor Werner J.A. Dahm
Professor Robert M. Ziff
Assistant Professor Joerg Lahann

© Hyun Su Lee 2008
All Rights Reserved

To
My wife Myung-Jin

ACKNOWLEDGEMENTS

First and foremost, I would like to express my sincere gratitude to my advisor Professor H. Scott Fogler for his guidance and encouragement throughout the course of my graduate studies. I am very thankful to him for his exceptional research philosophy and high standard of excellence that he has instilled in me. I consider myself blessed to have been part of his research group.

I thank my doctoral committee members, Professors Robert Ziff, Werner J.A. Dahm and Joerg Lahann for their valuable inputs. I also thank Drs. William H. Thomason, Probjot Singh and Mike Scribner in ConocoPhillips Research Center for providing me an opportunity to work with for six months in which time I have obtained a lot of knowledge about wax deposition and gelation. I thank the technical staffs of ConocoPhillips for their help in the laboratory.

The members of the Fogler research group, past and present, have been extremely helpful both in and out of the lab. First of all, I am grateful to Dr. Rama Venkatesan for many useful and pleasant discussions about wax and many other interesting issues. I thank previous members Dr. Nihat Gurmen, Dr. Duc Nguyen, Dr. Piyarat Wattana (Ann), Dr. Veerapat Tantayakom (Five), Dr. Kris Paso, and Dr. Ryan Hartman and current members Michael, Lizzie, Kriang, Tabish, Jason and Abdulla.

I thank the excellent staff of our department for taking care of many needs, especially Laura Bracken, Susan Hamlin, Leslie Cypert, Pablo LaValle and Mike Africa. They are all acknowledged for their help.

I would like to thank my family members-my adorable daughters Suhyun & Sujin (Grace), my sister Hyun Ju & brother-in-law (Dr. Chang-Sun Kim), Myung-Hun Kim, parents-in-law and parents. I also thank many friends in Korean Bible Church in Ann Arbor for their friendship with me and prayer. Above all, I thank my wife Myung-Jin for providing unlimited support during my Ph.D. studies. Without her love and support, the completion of this work would not have been possible.

TABLE OF CONTENTS

DEDICATION	ii
ACKNOWLEDGEMENTS	iii
LIST OF FIGURES	viii
LIST OF TABLES	xii
LIST OF APPENDICES	xiii
ABSTRACT	xiv
CHAPTER	
I. INTRODUCTION	1
Motivation	1
Wax Deposition Problem in Flow Conditions	2
Wax Gelation and Restart Problem after Shut-in	5
Research Objectives	7
Thesis Overview	7
References.....	10
II. BACKGROUND	12
Wax in Crude Oil	12
Wax Crystallization and Wax-Oil Gel Formation.....	13
Gel Failure Strength.....	14
Restart of Gelled Pipelines.....	15
Physics of Wax Deposition Phenomena	16
Radial Mass Transport.....	17
Aging of Wax Deposit.....	18
Wax Deposition Model under Laminar Flow.....	19

Wax Deposition Model under Turbulent Flow.....	21
References.....	24
III. WAXY OIL GEL BREAKING MECHANISMS : ADHESIVE VERSUS COHESIVE FAILURE.....	27
Introduction.....	27
Experimental Section.....	31
Results and Discussion.....	35
Restart Model.....	44
Field Considerations.....	52
Summary.....	53
Nomenclature.....	54
References.....	55
IV. COMBINED CONVECTIVE HEAT AND MASS TRANSFER ANALYSIS OF WAX DEPOSITION UNDER TURBULENT FLOW CONDITIONS	58
Introduction.....	58
Theory - Wax deposition model.....	64
Results and Discussion.....	79
Summary.....	93
Nomenclature.....	93
References.....	96
V. CONCLUSIONS	99
Gel Breaking Phenomena.....	99
Wax Deposition Phenomena.....	100
References.....	102

VI. FUTURE WORK	103
Single Phase Wax Deposition under Low Heat Flux Conditions...	103
Multiphase Wax Deposition Experiments and Modeling.....	104
Impact of Wax Inhibitors on Paraffin Precipitation Kinetics.....	106
Impact of Surface Roughness on Wax-Oil Gel Breaking Mechanism.....	107
Restart of Non-uniformly Gelled Pipeline.....	109
References.....	111
 APPENDICES	 113

LIST OF FIGURES

Figure 1.1:	Oil production in deep sea areas.	2
Figure 1.2:	Wax deposit reducing the effective diameter in a retrieved pipeline (Singh et al., 2000).	3
Figure 1.3:	Pigging method to remove wax deposits from pipelines (Nguyen, 2004).	4
Figure 1.4:	Usage of a fused chemical reaction to remediate the paraffin plugging in subsea pipelines (Nguyen, 2004).	4
Figure 1.5:	Cross-polarized microscope photo of wax-oil gel.	6
Figure 2.1:	Cross-polarized microscope photo of wax-oil gel (Lee et al., 2007).	13
Figure 2.2:	Wax deposition occurs when the inner wall temperature is below the cloud point temperature.	17
Figure 2.3:	Schematic of the wax deposition process.	19
Figure 2.4:	Theory vs. experiment for the wax deposition under a laminar flow condition (Singh et al., 2000).	20
Figure 2.5:	Comparison of the Chilton-Colburn analogy and the solubility method in the solubility as a function of temperature space.	22
Figure 3.1:	Schematic of pressure propagation during restart (modified from experimental results by Borghi et al., 2003).	30
Figure 3.2:	Carbon number distribution of the model wax-oil mixture.	32
Figure 3.3:	Schematic of the model pipeline system.	33
Figure 3.4:	Typical gel breaking experimental results with different gel temperatures.	36
Figure 3.5:	Gelation temperature vs. volume required to break the gel.	38
Figure 3.6:	Gel failure stress vs. cooling rate obtained by the controlled stress rheometer.	40

Figure 3.7:	Cross-polarized microscope photo of wax-oil gel at.....41 (a) T=19.1°C under cooling rate of 3.5°C/hr (b) T=19.0°C under cooling rate of 20°C/hr.
Figure 3.8:	Restart pressure obtained by model pipeline and controlled stress rheometer.43
Figure 3.9:	Sketch of compressed gel due to an applied pressure both of displacement and deformation.45
Figure 3.10:	(a) P_{in} is constant and greater than $\Delta P_{restart}$ (c) P_{in} as a function of time.46
Figure 3.11:	Schematic of pressure propagation during restart (modified from experimental results by Borghi et al. 2003).48
Figure 3.12:	Volume change of waxy oil due to the applied pressure presented in Hénaut et al (2003) and Tait equation (Hayward, 1967) given in Equation (3.5).50
Figure 3.13:	Compressed volume during the restart process for lab-scale pipeline. ...51
Figure 3.14:	Strategy for the restart of a gelled pipeline.52
Figure 4.1:	Wax deposit in a retrieved pipeline (Singh et al., 2000).59
Figure 4.2:	Schematic of convective heat and mass transfer suggested by Singh et al. (2000).62
Figure 4.3:	Theory vs. experiment for the wax deposition under a laminar flow condition (Singh et al., 2000).66
Figure 4.4:	Comparison of the Chilton analogy and the solubility method in the solubility as a function of temperature space.68
Figure 4.5:	Heat and mass transfer boundary layer for turbulent waxy oil flow.68
Figure 4.6:	Sherwood number profile as a function of axial distance.73
Figure 4.7:	Wax concentration profile in the turbulent boundary layer (Re=7350). 75
Figure 4.8:	The ratio of Sherwood Number to Nusselt number as a function of precipitation rate constant (Re=7350).76
Figure 4.9:	Comparison between theory and experiment for the wax deposition under a flow rate of 1 gpm and wall temperature of 7.2 °C

	(Re=535).	79
Figure 4.10:	Wax deposit growth and aging under turbulent condition (Re=7350). ...	81
Figure 4.11:	Comparison between the Chilton-Colburn analogy, Solubility method and improved model with precipitation kinetics (Re=7350) $A = \frac{\bar{F}_w(t_{final}) - \bar{F}_w(t=0)}{(\alpha_{final} - 1)^2} = 0.0045$	83
Figure 4.12:	Comparison between model prediction and flow loop experiments for various flow rates (Q=10gpm, 15gpm and 20gpm).	83
Figure 4.13:	Deposit thickness versus time under turbulent flow. Theoretical predictions with the Chilton-Colburn analogy, the solubility method (Venkatesan and Fogler, 2004) and the theoretical model with precipitation kinetics.	85
Figure 4.14:	Wax % in the deposit after 24 hours (Lund, 1998).	85
Figure 4.15:	Sketch of radial temperature profile in a field pipeline.	86
Figure 4.16:	Growth of wax deposit for the baseline case at t= 1 day, 7 days, 14 days, 30 days, and 60 days.	87
Figure 4.17:	Aging of wax deposit for the baseline case.	89
Figure 4.18:	Solubility as a function of temperature for South Pelto crude oil (Lund, 1998), Garden Banks condensates (Hernandez Perez, 2002) and model oil (Venkatesan, 2003).	90
Figure 4.19:	Axial thickness profiles for various oils. The input parameters used for these calculations of the wax deposition in a field pipeline are same as that of the baseline case as summarized in Table 4.2.	91
Figure 4.20:	Axial wax fraction profiles for various oils. The input parameters used for these calculations of the wax deposition in a field pipeline are same as that of the baseline case as summarized in Table 4.2.	92
Figure 6.1:	General flow regimes seen in water/oil flow for various flow rates. ...	106
Figure 6.2:	Preliminary sketch of effect surface roughness on the delineation point.	108
Figure A.1:	Diffusion occurs through regularly spaced slits or pores.	115
Figure A.2:	Comparison between Aris's and Cussler's effective diffusivity	

model as a function of wax fraction in the deposit

$$A = \frac{\bar{F}_w(t_{final}) - \bar{F}_w(t=0)}{(\alpha_{final} - 1)^2} = 0.0045 \dots\dots\dots 116$$

Figure B.1: The precipitation rate constant as a function of temperature,
 $\ln \left[\frac{k_r(T)}{k_r(T_{cloud})} \right]$ vs. $1/T$ 118

Figure B.2: The precipitation rate constant as a function of temperature,
 $\frac{k_r(T)}{k_r(T_{cloud})}$ vs. T119

Figure D.1: Image of a 5% wax in oil mixture cooled down at the cooling rate of 6°C/min. The maximum crystal length is about 17 μm and average size is about 13.5 μm (Venkatesan et al., 2005)123

Figure E.1: Axial thickness profile with various insulation thicknesses.125

Figure E.2: Axial bulk temperature profile with various insulation thicknesses. ...126

Figure E.3: Axial thickness and temperature profiles with two insulation conductivities ($k_{ins} = 0.29$ W/m⁰K and $k_{ins} = 1.0$ W/m⁰K).127

LIST OF TABLES

Table 4.1:	Input parameters for the baseline case TU flow loop calculation.....	84
Table 4.2:	Input parameters for the baseline case for a field scale pipeline system	87
Table 6.1:	Single phase flow loop experimental conditions with a large scale flow loop system.	104

LIST OF APPENDICES

Appendix

- A. Calculation of the Effective Diffusivity of Wax in Oil114
- B. Temperature Dependency of the Precipitation Rate Constant $k_p(T)$ 117
- C. Calculation of the Critical Nucleus Size120
- D. The Precipitation Rate Constant at the Cloud Point Temperature122
- E. Effects of Thermal Insulation on the Wax Deposition in Field Pipelines...125

ABSTRACT

Highly waxy crude oils can cause significant problems such as blockage of a pipeline because of the precipitation and deposition of select wax components during the production and transportation of the crude oil. The cost of wax management is enormous and rapidly increasing because of increased oil production in deep sea areas. Wax management costs can be significantly reduced if wax deposition and gelation in pipeline can be accurately predicted. In this research, a rigorous wax deposition model combined with the wax precipitation kinetics in the boundary layer was developed using a computational heat and mass transfer analysis. This model accurately predicted the deposition and aging rates for lab scale and pilot plant scale flow loop tests under laminar and turbulent flows. The model was also extended to make prediction in subsea field pipelines. Studies of wax deposition under turbulent flow conditions showed that the deposition rate is significantly reduced by the precipitation of waxes in the thermal boundary layer. Furthermore, this analysis proved that the convective mass flux is bounded by the Venkatesan-Fogler solubility method as the lower bound and the Chilton-Colburn analogy method as the upper bound. The challenging issue of the restart of a gelled subsea pipeline after shut-in period was also studied experimentally and theoretically. The gel inside the pipeline formed during a stoppage of oil flow must be broken to restart the flow. The gel breaking mechanisms during the restart of a pipeline were investigated and were found to be a function of cooling rate. The existence of a delineation point between cohesive and adhesive failures was found by measuring the gel

strengths using various cooling rates. Using a controlled stress rheometer and a cross-polarized microscope, we elucidated the phenomena behind the existence of a delineation point between cohesive and adhesive failures. This study has shown that the controlled stress rheometer can predict the restart pressure of a gelled pipeline when the cooling rate is low and breakage occurs adhesively. Finally, we developed a restart model that can predict the relationship between the amount of injection fluid and the pressure applied to the pipeline.

CHAPTER I

INTRODUCTION

Motivation

Crude oil is a complex mixture of saturates (paraffins/waxes), aromatics, naphthenes, asphaltenes and resins. Among these components, high molecular weight paraffins (interchangeably referred to as waxes throughout this work) and asphaltenes are typically responsible for production and transportation problems in subsea pipeline systems. At reservoir temperatures (70-150 °C) and pressures (50-100 MPa), wax molecules are dissolved in the crude oil. However, as the crude oil flows through a subsea pipeline resting on the ocean floor at a temperature of 4 °C, the temperature of oil eventually decreases below its cloud point temperature (or wax appearance temperature, WAT) because of the heat losses to the surroundings. The solubility of wax decreases drastically as the temperature decreases and wax molecules start to precipitate out of the crude oil.

Because oil reservoirs near the shoreline have become depleted, oil production in deep sea areas has increased significantly. Forecasters expect that, by 2017, oil production from deep sea areas will exceed 8 million barrels per day which is about three times greater than deep sea production in year 2002 (2.4 million barrels per day) (Moritis, 2002). Recent advances in the exploration and production technologies in deep sea areas have made deep water drilling economically feasible and the oil industry has drilled subsea oil wells as far as 160 miles away from the shore (Nguyen, 2004). As oil wells are

developed further offshore as illustrated in Figure 1.1, wax problems will become more severe and extensive due to the increased transportation lines on the cold ocean floor.

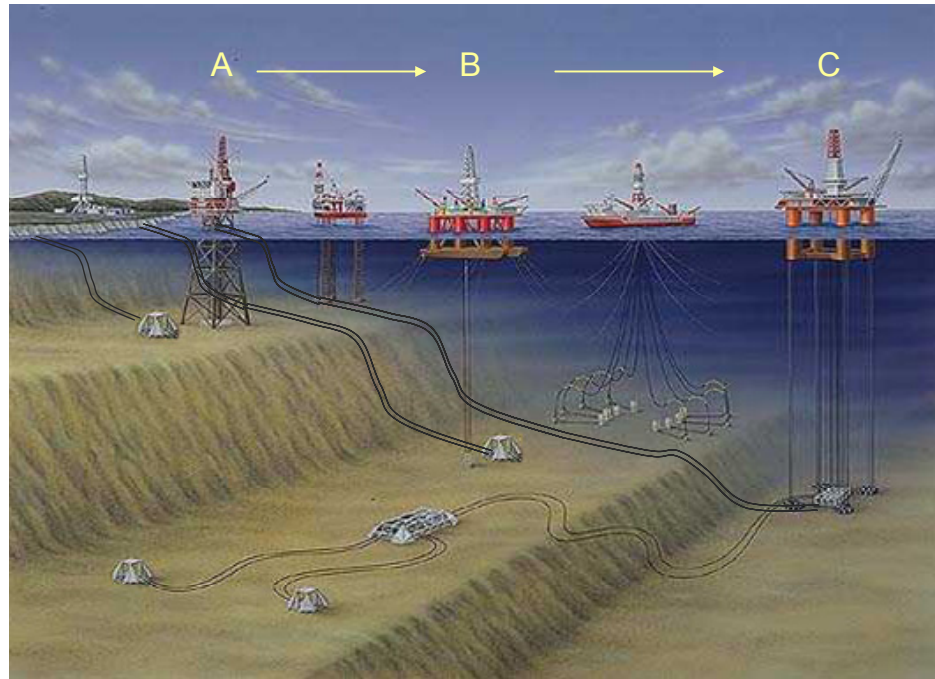


Figure 1.1: Oil production in deep sea areas.

The research in this dissertation elucidates the fundamental understanding of problems in the production and transportation of waxy crude oil. More specifically, the flow assurance problems incurred by the precipitation of wax molecules during the production and transportation in the field pipelines can be categorized as: (1) wax deposition in flow conditions and (2) wax gelation and restart problem after shut-in period.

Wax Deposition Problem in Flow Conditions

Wax deposition occurs when paraffin components in crude oil (alkanes with carbon numbers greater than 20) precipitate and deposit on the cold pipeline wall when

the inner wall temperature falls below the cloud point temperature (solubility limit). If preventive methods for wax deposition (e.g. insulation of pipeline, injection of wax inhibitor, or combination of both) are not successful, a wax gel layer grows rapidly in thickness and impedes the flow of oil due to the flow restriction, as shown in Figure 1.2. In the Lasso field in the UK, wax deposition was so severe and frequent that the entire field was abandoned at a cost of over \$100,000,000 (Singh et al., 2000; Nguyen et al., 2001).

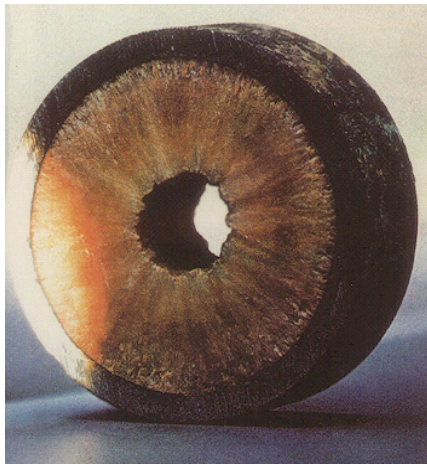


Figure 1.2: Wax deposit reducing the effective diameter in a retrieved pipeline (Singh et al., 2000).

Once the wax deposit starts to impede the production and transportation due to the flow restriction, corrective methods to remediate the wax deposit are generally necessitated. One of the most commonly used corrective methods used in the fields is pigging. In pigging, a pig (a solid object with the diameter smaller than the inner diameter of the pipe) passes through the pipeline to scrape off the wax deposit as shown in Figure 1.3. However, the pigging method can not efficiently be utilized without a proper wax deposition prediction.

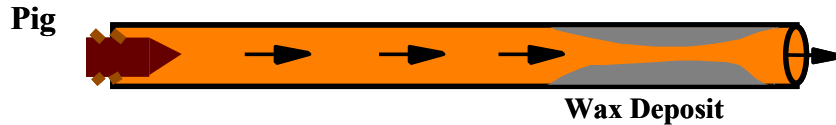


Figure 1.3: Pigging method to remove wax deposits from pipelines (Nguyen, 2004).

For example, pigs at times get stuck inside the pipeline in the presence of thick hard deposits making the situation worse, which occurred in a Gulf of Mexico pipeline (Fung et al., 2006). In the worst cases, production must be stopped in order to replace the plugged portion of the line, which is estimated to cost approximately \$40,000,000 per incident as reported by Elf Aquitaine.

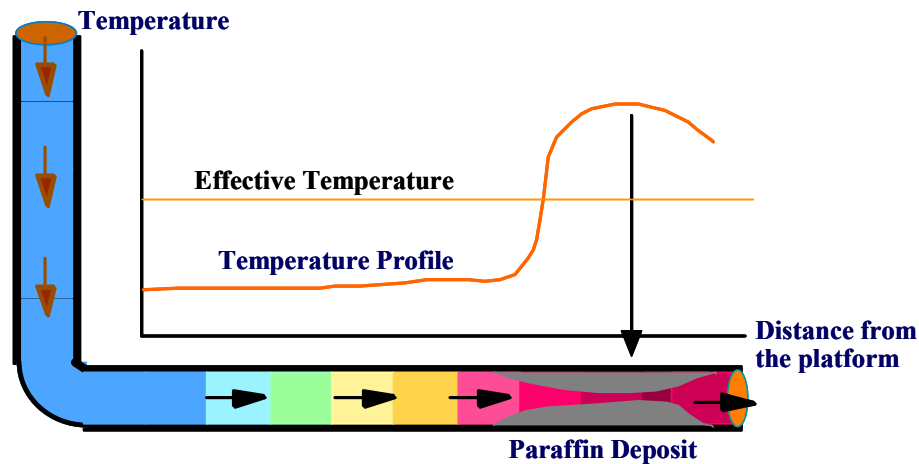


Figure 1.4: Usage of a fused chemical reaction to remediate the paraffin plugging in subsea pipelines (Nguyen, 2004).

Another notable remediation technique is to use a fused chemical reaction with controlled heat emission (Singh and Fogler, 1998; Nguyen et al., 2001, 2003, 2004; Nguyen and Fogler, 2005) to remove the wax deposit as shown in Figure 1.4. However, in order to successfully use this technique, it is critical to know the thickness profile and the wax fraction of the deposit as a function of axial location and time. If this technique were to be used based on inaccurate information on the location of wax deposit and its

wax fraction, there could be unwanted local high temperature in the pipeline due to the failure of re-dissolving wax deposit.

Successful management of wax deposition will become more important in the future because new explorations and productions are being made farther offshore. The wax deposition management cost to the petroleum production industry is enormous and will increase both in terms of capital costs (e.g. preventive methods) and operating costs (e.g. corrective methods) (Paso, 2005). It is widely recognized that tremendous savings could be realized from accurate wax prediction in offshore systems (Majeed et al., 1990). Consequently, a fundamental understanding of wax deposition phenomena and a comprehensive wax deposition model based on this fundamental understanding is strongly necessitated in order to overcome the challenges in production and transportation of subsea pipelines.

Wax Gelation and Restart Problem after Shut-in

Whereas wax precipitation during oil flow results in wax deposition and flow restriction, wax precipitation during a production shutdown results in problems when attempting to restart the flow. If the transportation in a pipeline is stopped due to a planned maintenance or an emergency situation such as severe weather conditions on the off-shore platforms (Fung et al., 2006; Thomason, 2000), the temperature and solubility of wax decreases and wax molecules precipitate out of liquid phase in a static condition. In the absence of flow, the precipitation of wax molecules leads to the formation of a wax-oil gel as shown in a cross-polarized microscope photo in Figure 1.5 that could

encompass the entire cross-section of the pipe. In order to restart flow and to recover the steady state flow, this wax-oil gel in the pipeline must be broken.

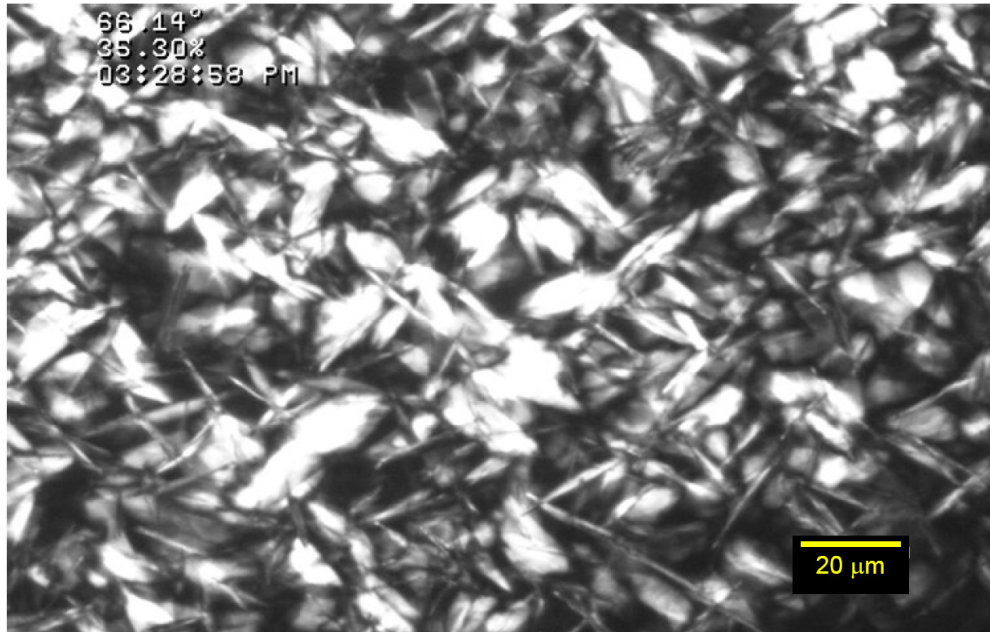


Figure 1.5: Cross-polarized microscope photo of wax-oil gel.

This restart flow problem is especially challenging when the ambient temperature is below the pour point temperature (ASTM D 5853) or the gelation temperature (Venkatesan et al., 2002), which indicates the lowest temperature at which oil is pumpable. In order to prevent this risk and to enhance the restartability after shut-in, chemical agents which can depress the pour point temperature and/or weaken the strength of the wax-oil gel. When assessing the restartability, it is necessary to estimate the pressure required to break the plug of wax-oil gel. The pressure required to break the gel and to restart flow is proportional to the strength of the gel (yield stress) and the aspect ratio of the pipeline. Consequently, a fundamental understanding on the wax-oil gel breaking phenomena is needed to overcome the challenges in production and transportation of subsea pipelines.

Research Objectives

The objectives of the research presented in this dissertation are to establish a fundamental understanding of wax deposition and gelation phenomena and use this understanding to develop theoretical models to simulate both the wax deposition and gel breaking phenomena in subsea pipelines. The unique combination of heat, mass and momentum transport phenomena in wax deposition and gel breaking problems demands rigorous theoretical and experimental investigations.

Specifically, the major goals of this work can be summarized as: (1) to elucidate the gel breaking mechanisms: cohesive vs. adhesive failures (2) to compare restart pressure measured by model pipeline system and the controlled stress rheometer (3) to develop a restart model that can predict the required volume injection during the restart process (4) to develop a computational heat and mass transfer model including the precipitation kinetics in the boundary layer and (5) to develop a computational wax deposition model in field subsea pipelines under turbulent flow conditions. Experimental results are obtained to compare with the simulation results for each objective.

Thesis Overview

The chapters of this thesis are written such that they can be read independently with a general knowledge of the relevant background. Additional theoretical and experimental details are given as they pertain to each chapter. Due to this format, there may be some repetition of introductory material from chapter to chapter. An overview of the main chapters is given below.

Chapter II. This chapter provides overview and background of the wax deposition and restart flow phenomena. Subjects include the wax crystallization and gel formation, the restart of gelled pipelines, the physics of wax deposition phenomena and wax deposition under turbulent flow conditions.

Chapter III. This chapter elucidates wax-oil gel breaking mechanisms using a model pipeline system, controlled stress rheometer and cross polarized microscope. Two yield stress measurement techniques-the model pipeline system and the controlled stress rheometer system-were compared and used to predict the required gel breaking pressure of a gelled pipeline. With microscopic observations and controlled stress rheometer experiments, this chapter elucidates cohesive failure (yielding of gel structure) and adhesive failure (yielding between the gel and pipe wall) and their dependence on cooling rate. Finally, this chapter develops a mathematical model that calculates the relationship between inlet pressure and injection volume using the compressibility of the wax-oil gel.

Chapter IV. This chapter investigates the combined heat and mass transfer phenomenon under laminar and turbulent flow conditions using the FDM (finite difference method) technique in order to exploit Singh et al. (2000)'s wax deposition model without using either a heat and mass transfer analogy or the solubility method. This chapter shows that the impact of precipitation of wax molecules on the convective mass flux in the boundary layer and that the improved wax deposition model is bounded by the solubility model (Venkatesan and Fogler, 2004) at the low end bound and the Chilton-Colburn analogy (Chilton, 1934) at the high end. By comparing the results of improved wax prediction

model with both lab scale and with large scale turbulent wax deposition experiments, this chapter shows that the wax deposition model can successfully predict both the thickness and the aging of wax deposit under various turbulent conditions. Finally, a case study of the computational wax deposition modeling for a field scale pipeline system is provided.

Chapters V and VI. Conclusions are drawn from the experimental and theoretical work presented in the preceding chapters. Recommendations for future work, including a study of single phase wax deposition under low heat flux conditions, multiphase wax deposition experiments and modeling, impact of wax inhibitors on paraffin precipitation kinetics, impact of surface roughness on wax-oil gel breaking mechanism, and restart of non-uniformly gelled pipeline, are proposed.

References

- ASTM D5853-95, "Standard Test Method for Pour Point of Crude Oils" (1995)
- Chilton, T.H., and A.P. Colburn, "Mass Transfer (Absorption) Coefficients Prediction from Data on Heat Transfer and Fluid Friction," *Ind. Eng. Chem.*, **26**, 1183 (1934).
- Fung, G., W.P. Backhaus, S. McDaniel, and M. Erdogmus, "To Pig or Not To Pig: The Marlin Experience with Stuck Pig," 2006 Offshore Technology Conference, Houston, TX (2006).
- Lee, H.S., P. Singh, W.H. Thomason, and H.S. Fogler, "Waxy Oil Gel Breaking Mechanisms: Adhesive versus Cohesive Failure," *Energy and Fuel*, (2007), accepted.
- Majeed, A., B. Bringedal, and S. Overa, "Model Calculates Wax Deposition for N. Sea Oils," *Oil & Gas J.* **88**, 63 (1990).
- Moritis, G., "Flow Assurance Challenges Production from Deeper Water," *Oil & Gas J.* **99**, 66 (2001).
- Nguyen, D. A., Ph.D. Thesis, University of Michigan 2004.
- Nguyen, A.D., H.S. Fogler, and C. Sumaeth, "Fused Chemical Reactions. 2. Encapsulation: Application to Remediation of Paraffin Plugged Pipelines," *Ind. Eng. Chem. Res.* **40**, 5058 (2001).
- Nguyen, A.D., M.A. Iwaniw, and H.S. Fogler "Kinetics and mechanism of the reaction between ammonium and nitrite ions: experimental and theoretical studies," *Chem. Eng. Sci.* **58**, 4351 (2003).
- Nguyen, A.D., H.S. Fogler, and C. Sumaeth, "Fused Chemical Reactions. 3. Controlled Release of a Catalyst To Control the Temperature Profile in Tubular Reactors," *Ind. Eng. Chem. Res.* **43**, 5862 (2004).
- Nguyen, A.D., and H.S. Fogler "Facilitated Diffusion in the Dissolution of Carboxylic Polymers," *AIChE J.* **51**, 415 (2005).
- Paso, K., Ph.D. Thesis, University of Michigan 2005.
- Paso, K., M. Senra, Y.B. Yi, A.M. Sastry, and H.S. Fogler, "Paraffin Polydispersity Facilitates Mechanical Gelation," *Ind. Eng. Chem. Res.* **44**, 7242 (2005).
- Singh, P., and H.S. Fogler, "Fused Chemical Reactions: The Use of Dispersion to Delay Reaction Time in Tubular Reactors," *Ind. Eng. Chem. Res.* **37**, 2203 (1998).

Singh, P., R. Venkatesan, H.S. Fogler, and N.R. Nagarajan, "Formation and Aging of Incipient Thin Film Wax-Oil Gels," *AIChE J.* **46**, 1059 (2000).

Thomason, W.H., "Start-Up and Shut-in Issues for Subsea Production of High Paraffinic Crudes," 2000 Offshore Technology Conference, Houston, TX (2000).

Venkatesan, R., Ph.D. Thesis, University of Michigan, 2003.

Venkatesan, R. and H.S. Fogler, "Comments on Analogies for Correlated Heat and Mass Transfer in Turbulent Flow," *AIChE. J.*, **50**, 1623 (2004).

Venkatesan, R., P. Singh, and H.S. Fogler, "Delineating the Pour Point and Gelation Temperature of Waxy Crude Oils," *SPE J.* **7(4)**, 349 (2002).

CHAPTER II

BACKGROUND

Wax in Crude Oil

Crude oil can be separated into four major chemical group classes: saturates (paraffin/wax), aromatics, resins and asphaltenes (SARA). Saturates are distinguishable from the other three classes because it is the only group that solely consists of non-polar carbons (i.e. alkanes) without double bonds (Wattana, 2004). Among these components in crude oil, high molecular weight paraffins and asphaltenes are the most responsible for the flow assurance issues encountered during transportation and production of crude oil (Singh et al., 2000).

Flow assurance issues with waxy oil are mainly caused by the temperature dependence of the solubility of wax molecules in the crude oil. Wax molecules are dissolved at reservoir temperatures (70-150 °C) and pressures (50-100 MPa). Once the crude oil leaves the reservoir, its temperature begins to drop due to the heat loss to the surroundings. When the oil temperature becomes lower than the cloud point temperature, the wax molecules present in concentrations greater than the solubility limit at the lower temperature become unstable and precipitate out of the liquid phase. This formation of crystals is the first step of both wax gelation and deposition problems.

Wax Crystallization and Wax-Oil Gel Formation

The characteristics of wax-oil gels depend on the crystal morphology and structures of the crystal networks, which are strong functions of both thermal and shear histories (Singh et al., 2000). The crystallization of wax molecules below the cloud point temperature incurs formation of gels with a complex morphology. As shown in Figure 2.1, the structure of the wax-oil gel is an interlocking of various wax forms such as needles, plates and orthorhombic wax crystals, dependent on the cooling rate (thermal history), wax concentration and shear history (Dirand et al., 1998; Singh et al., 2000).

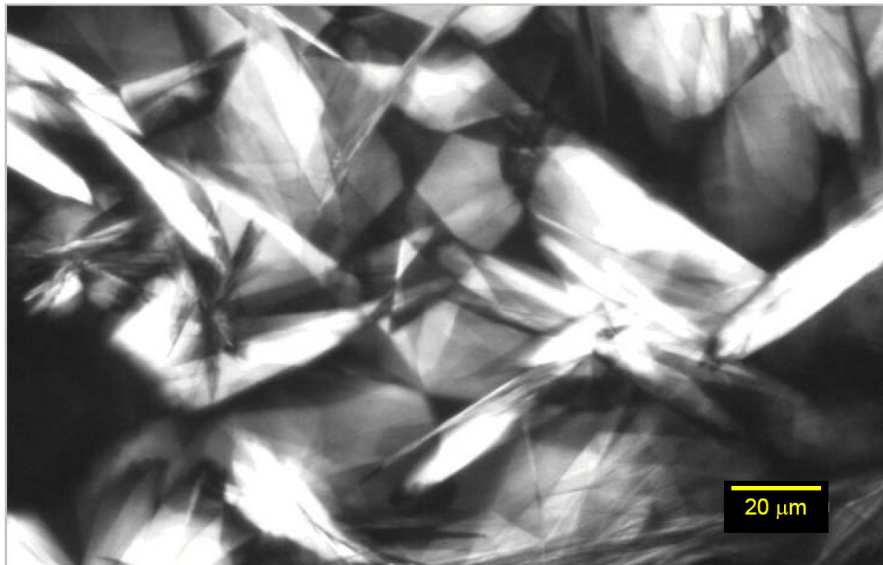


Figure 2.1: Cross-polarized microscope photo of wax-oil gel (Lee et al., 2007).

Cazaux et al. (1998) investigated the gel structure using X-ray diffraction (XRD), Small-angle X-ray scattering (SAXS), a cross-polarized microscopy (CPM) and a controlled stress rheometer (CSR). They reported that the key parameters that determine the structure of wax-oil gel are the crystal shape (aspect ratio) and number density of wax crystals, both of which depend on the temperature and cooling rate. Chang et al. (1999) reported that the morphology of the paraffin crystals strongly depends on both the cooling rate and the shear stress applied to the mixture (Kane et al., 2003; Venkatesan et

al., 2005). Recently Visintin et al. (2005) and Vignati et al. (2005) reported that waxy gels have the characteristics of colloidal gels and the radius of gyration of the wax-oil gel changes with cooling rate.

Gel Failure Strength

As the morphology and structure are strong functions of shear and thermal histories, the gel strength and gel failure mechanisms also depend on the shear and thermal histories (Hénaut et al., 1999; Kane et al., 2003; Venkatesan et al., 2005; Lee et al., 2007). If the cooling rate is low, wax molecules have sufficient time and mobility to form large crystals and as a result the number density of crystals decreases. This crystal morphology affects both the strength of the gel and the failure mechanism of the gel in the pipeline and rheometer experiments (Venkatesan, 2003; Lee et al., 2007). For example, the restart of the gelled oil may result from the breakdown of the gel structure itself (cohesive failure) or it may occur because of the breakage at the pipe-gel interface (adhesive failure) depending on the cooling rate and wax content (Venkatesan, 2003; Lee et al., 2007). The cohesive yielding of the gel occurs when the applied stress exceeds the mechanical strength of the wax-oil gel structure maintained by the mechanical interlocking of wax crystals formed by London dispersion or van der Waals forces of n-alkanes (Venkatesan et al., 2005; Vignati et al., 2005; Visintin et al., 2005; Lee et al., 2007).

Restart of Gelled Pipelines

Wax precipitation and gelation during a production shutdown result in problems while attempting to restart the flow, especially when the subsea temperature is below the pour point temperature. During a shutdown, the crude oil in the pipeline is cooled under static conditions leading to wax precipitation if the oil temperature is below the cloud point temperature. Under these circumstances, the precipitation of waxes leads to the formation of a wax-oil gel that could encompass the whole cross-section of the pipe. Therefore, this wax-oil gel blocking the pipeline must be broken in order to restart flow. The pressure required to break the gel and restart flow depends on the strength of the gel and the aspect ratio (L/D) of the pipe. The gel strength can be expressed in the form of the shear yield stress of the gel. Therefore, understanding the yield stress of the wax-oil gel is essential in determining the pressure required for restarting flow.

Because of the complexity in yielding behavior of the wax-oil gel, many studies have been carried out to estimate the yield strength of the wax-oil gel for various conditions and, ultimately, the pressure required to restart the gelled pipelines in the field (Davenport and Somper, 1971; Uhde and Kopp, 1971; Verschuur et al., 1971; Wardhaugh and Boger, 1991; Rønningsen, 1992; Chang et al., 1998; Chang et al., 1999; Thomason, 2000; Borghi et al., 2003; Davidson et al., 2004). However, previous literature has reported that the reproducibility of measurement of the yield strength obtained from the controlled stress rheometer and the model pipeline have been “extremely” low and inconsistencies exist between yield strength measuring techniques (Davenport and Somper, 1971; Wardhaugh and Boger, 1991). These inconsistencies have been attributed to differences in flow patterns (Couette and Poiseuille), compressibility of

the wax-oil gel and pipe wall, and pressure propagation during the gel yielding in the pipeline (Wardhaugh and Boger, 1991; Borghi et al., 2003). However, Rønningsen (1992) reported reasonably good agreement between the model pipeline experiments and the controlled stress rheometer. Rønningsen (1992) also reported that the stress loading rate, cooling rate, and aging time significantly affect the yield stress and consequently these conditions should be consistently applied for both of the model pipeline and controlled stress rheometer experiments. These inconclusive contradicting experimental results have not been fully explained and thereby hampering the prediction of restart pressure of gelled pipeline by using the controlled stress rheometer (Davenport and Somper, 1971; Wardhaugh and Boger, 1991; Rønningsen, 1992; Borghi et al., 2003). One of the objectives of this dissertation is to clarify this inconsistency by providing an agreement between the model pipeline and the controlled stress rheometer if the gel fails adhesively and the gel has been formed as a continuous gel under a hydrostatic head during cooling and aging period.

Physics of Wax Deposition Phenomena

Wax precipitation during crude oil flow causes wax deposition and flow restriction. Wax deposition during the flow of waxy crude oils through subsea pipelines occurs as a result of the precipitation of wax molecules adjacent to the cold pipe wall. Thus, wax deposition can only occur when the inner pipe wall temperature is below the cloud point temperature. The precipitated wax molecules near the pipe wall start to form an incipient gel at the cold surface. The incipient gel formed at the pipe wall is a 3-D network structure of wax crystals and contains a significant amount of oil trapped in it.

The incipient gel grows as time progresses while there are radial thermal and mass transfer gradients as a result of heat losses to the surroundings as shown in Figure 2.2.

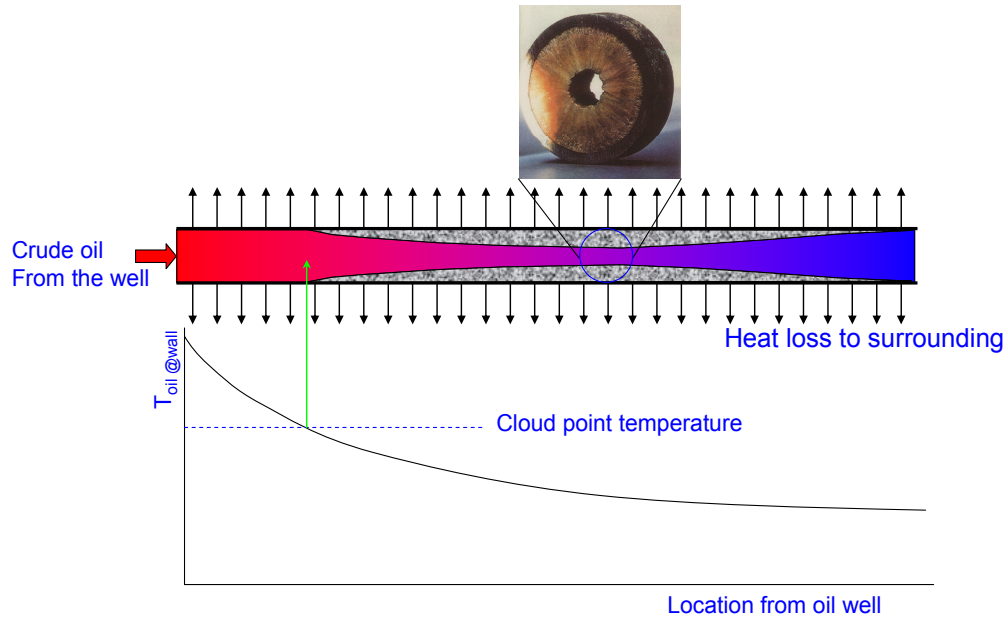


Figure 2.2: Wax deposition occurs when the inner wall temperature is below the cloud point temperature.

Radial Mass Transport

The radial wax concentration gradient is established by the precipitation of wax molecules out of the oil. This lowered wax concentration near the oil-deposit (gel) interface results in a mass flux of the wax molecules towards the surface of the incipient gel layer. This mass flux causes the wax deposit to become thicker as time progresses.

A number of radial mass transportation mechanisms have been suggested to forecast the growth of a wax deposit including radial convective flux (Singh et al., 2000, 2001), molecular diffusion (Bern et al., 1980; Burger et al., 1981; Majeed et al., 1990; Brown et al., 1993; Svendsen, 1993; Ribeiro et al., 1997; Creek et al., 1999), and precipitated wax particle transportation (by shear dispersion, Brownian diffusion, and gravity settling (Todi, 2005)). However, Singh et al., (2000) confirmed that the

contribution of precipitated wax particles on the wax deposition is not significant for flow conditions encountered in oil pipelines on the ocean floor.

Among these radial transportation mechanisms, there is consensus that the convection and molecular diffusion in the laminar sub-layer are the major radial transportation mechanisms (Bern et al., 1980; Burger et al., 1981; Majeed et al., 1990; Brown et al., 1993; Svendsen, 1993; Ribeiro et al., 1997; Creek et al., 1999; Singh et al., 2000, 2001; Venkatesan and Fogler, 2004). In Singh et al. (2000)'s wax deposition model, they calculated the mass flux using the convective mass transfer coefficient obtained from laminar Sherwood number correlations (Hausen, 1943; Seider and Tate, 1936). It is notable that, most of the earlier models before Singh et al. (2000, 2001)'s model calculated the radial wax flux assuming of thermodynamic equilibrium in the mass transfer boundary layer, i.e. the wax concentration is identical with the solubility in the boundary layer. However, this equilibrium assumption is not valid when the difference between the solubility and the wax concentration in the boundary layer is large enough such that the precipitation kinetics of wax molecules in the boundary layer is slow (Paso et al., 2005).

Aging of Wax Deposit

A wax deposit is not a pure solid phase, but a gel-like mixture and acts as a porous medium. The liquid entrapped in the gel provides a pathway for the diffusion of wax molecules within the gel. This internal diffusion and subsequent precipitation of wax molecules inside the gel layer results in an increase in the solid wax content of the gel deposit as shown in Figure 2.3.

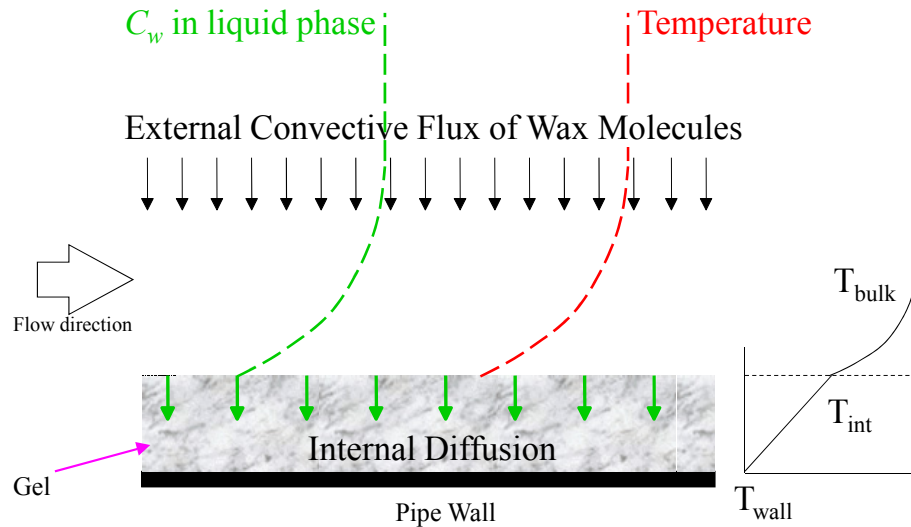


Figure 2.3: Schematic of the wax deposition process.

Many earlier studies have assumed that the wax fraction in the deposit is constant during the wax deposition process (Bern et al., 1980; Burger et al., 1981; Majeed et al., 1990; Brown et al., 1993; Svendsen, 1993; Ribeiro et al., 1997) and have used the wax content as an adjustable parameter (Paso, 2005). However, this assumption has been proven to be invalid (Lund, 1998; Creek et al, 1999; Singh et al., 2000, 2001) both theoretically and experimentally. Generally, higher flow rates enhance aging and wax fractions in the deposit as high as 60-70% have been reported (Lund, 1998).

Wax Deposition Model under Laminar Flow

Singh et al. (2000) developed a comprehensive mathematical model based on the fundamental physics of wax deposition that can predict both wax deposit thickness and wax aging phenomenon under laminar flow. The formation process of wax deposit can be described by following steps as stated by Singh et al. (2000):

1. Gelation of the waxy oil (formation of incipient gel layer) on the cold surface

2. Diffusion of waxes (hydrocarbons with carbon numbers greater than the critical carbon number) towards the gel layer from the bulk
3. Internal diffusion of these wax molecules through the trapped oil
4. Precipitation of these wax molecules within the gel deposit
5. Counter-diffusion of de-waxed oil (hydrocarbons with carbon numbers lower than the critical carbon number) out of the gel deposit

In these steps, the diffusing wax molecules are alkanes with carbon numbers greater than a *critical carbon number*, whereas the de-waxed oil that diffuses out of the deposit consists of alkanes carbon numbers lower than the critical carbon number (Singh et al., 2000; Paso, 2005). Steps 3 to 5 result in the aging of the gel, whereby the solid wax content of the gel increases with time. Figure 2.4 shows excellent agreement between Singh et al. (2000)'s theoretical prediction and experimental results for both effective radius change (thickness) and aging (wax fraction).

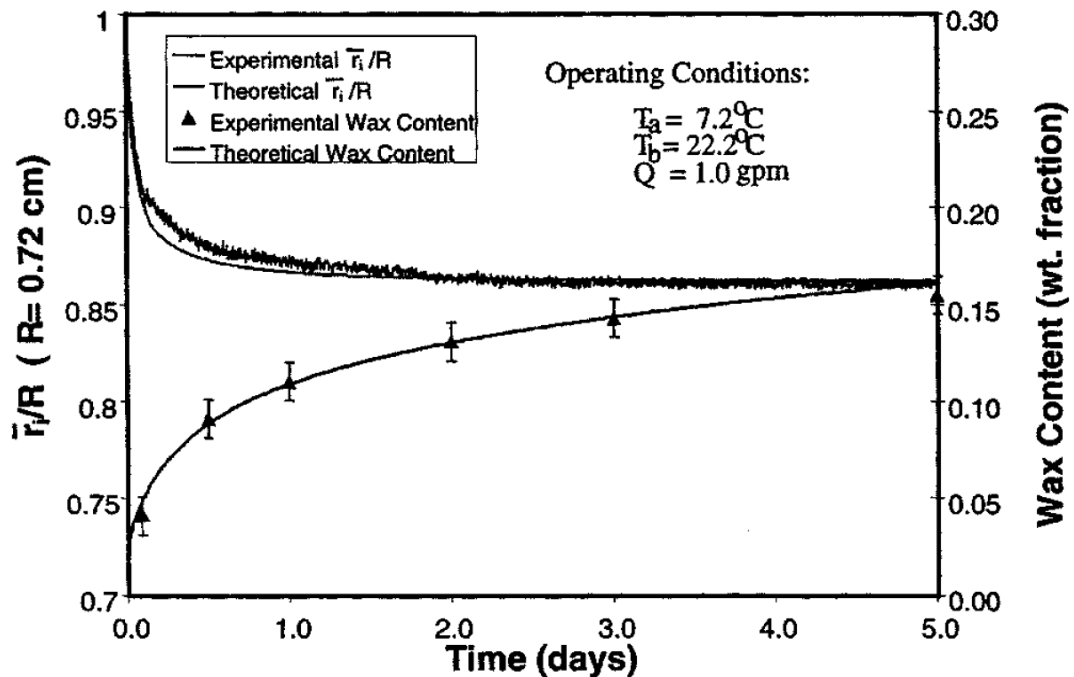


Figure 2.4: Theory vs. experiment for the wax deposition under a laminar flow condition (Singh et al., 2000).

Wax Deposition Model under Turbulent Flow

Venkatesan (2003) reported that direct extrapolation of Singh et al. (2000)'s laminar model to the turbulent conditions overpredicts the wax deposit thickness. The reason for the failure of direct extrapolation is the use of the heat-mass transfer analogies in wax deposition forecast (Venkatesan and Fogler, 2004). The heat-mass transfer analogies such as the Chilton-Colburn analogy shown in Equations (2.1) and (2.2) are generally valid and are frequently used for many chemical engineering problems.

$$Nu = 0.023 Re^{0.8} Pr^{1/3} \quad (2.1)$$

$$Sh = 0.023 Re^{0.8} Sc^{1/3} \quad (2.2)$$

However, the heat-mass transfer analogy is valid only when the temperature and concentration fields are independent. As shown in the wax concentration vs. temperature plot in Figure 2.5, the Chilton-Colburn analogy provides maximum supersaturation (indicated as shaded area) due to the independence of the temperature and concentration fields. In addition, the Lewis number (Sc/Pr) is high (the order of 10^2), which results in a much thinner mass transfer boundary layer than the thermal boundary layer. As a result, the wax concentration adjacent to the oil-deposit interface approaches the bulk wax concentration because the thickness of mass transfer boundary layer approaches zero, which results in the maximum convective mass transfer rate based on Equation (2.2). In this approach, the wax concentration in the boundary layer is not affected by thermodynamics but is solely determined by the transport processes of radial diffusion and axial advection.

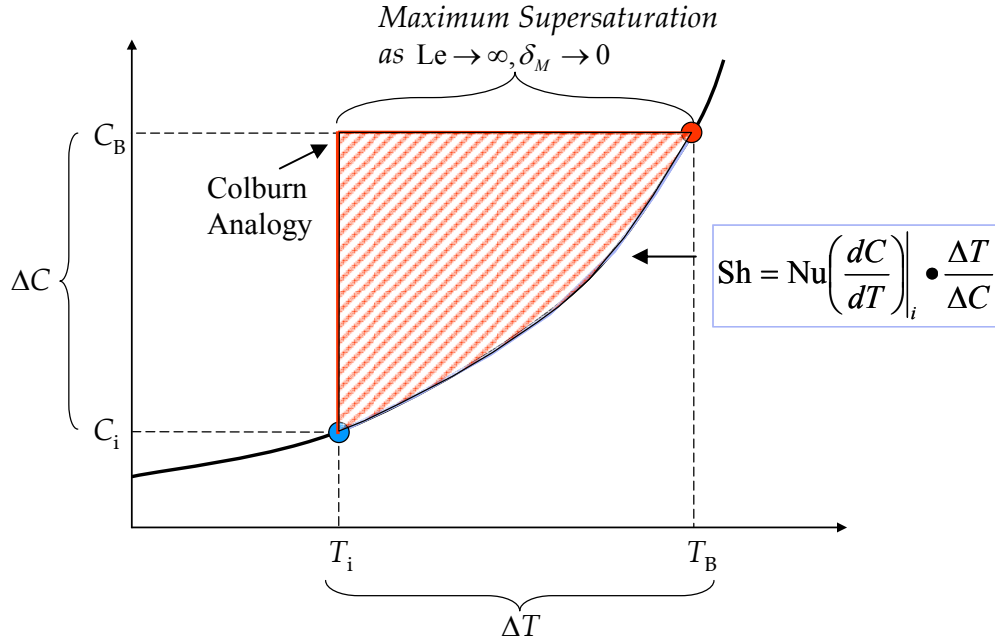


Figure 2.5: Comparison of the Chilton analogy and the solubility method in the solubility as a function of temperature space.

Because heat and mass transfer occur simultaneously in the boundary layer, the wax concentration profile is strongly influenced by the temperature profile (Venkatesan and Fogler, 2004). In order to take into account of this dependency, Venkatesan and Fogler (2004) proposed a new solubility method to calculate convective mass transfer rate when there is a dependency between heat and mass transfer.

$$Sh_{solubility} = Nu \left(\frac{dC}{dT} \right) \Big|_i \cdot \frac{\Delta T}{\Delta C} \quad (2.3)$$

The solubility method used to calculate the convective mass flux assumes that the concentration profile in the mass transfer boundary layer follows the thermodynamic equilibrium limit between temperature and concentration at every point. In the solubility method, the convective mass flux fully depends on the temperature profile and solubility of wax as a function of temperature as given in Figures 2.5. The Chilton-Colburn analogy represents the full supersaturation and the solubility method provides the minimum mass

transfer rate indicating the full heat-mass transfer dependency. The actual concentration profile exists between the concentration profiles of the Chilton-Colburn analogy and the solubility method depending on the precipitation kinetics as illustrated in the shaded area in Figure 2.5.

One of the objectives of this dissertation (Chapter IV) is to elucidate the impact of the precipitation in the boundary layer on the wax deposition model by using the FDM (Finite Difference Method). In Chapter IV, the combined heat and mass transfer phenomenon under laminar and turbulent flow conditions is investigated in order to exploit Singh et al. (2000)'s wax deposition model without using either a heat and mass transfer analogy (e.g. the Chilton-Colburn) or the solubility method (Venkatesan and Fogler, 2004).

References

- Bern, P.A., V.R. Withers, and R.J.R. Cairns, "Wax Deposition in Crude Oil Pipelines," Proc. Eur. Offshore Pet. Conf. Exhib., London, 571 (1980).
- Borghetti, G.-P., S. Corrao, M. Merlini, and C. Carniani, "Prediction and Scaleup of Waxy Oil Restart Behavior," 2003 SPE International Symposium on Oilfield Chemistry Houston, TX. (2003)
- Brown, T.S., V.G. Niesen, and D.D. Erickson, "Measurement and Prediction of the Kinetics of Paraffin Deposition," Proc. SPE Technical Conf. and Exhib., Houston, 353 (1993).
- Burger, E.D., T.K. Perkins, and J.H. Striegler, "Studies of Wax Deposition in the Trans Alaska Pipeline", *J. Petroleum Tech.* **33**, 1075 (1981).
- Cazaux, G., L. Barre, and F. Brucy, 1998 SPE Annual Technical Conference and Exhibition, New Orleans, 27 (1998).
- Chang, C., D.V. Boger, and Q.D. Nguyen, "Yielding of Waxy Crude Oils", *Ind. Eng. Chem. Res.* **37**, 1551 (1998)
- Chang, C., O.D. Nguyen, and H.P. Rønningsen, "Isothermal Start-up of Pipeline Transporting Waxy Crude Oil," *J. Non-Newt. Fluid Mech.* **87**, 127 (1999)
- Creek, J.L., H.J. Lund, J.P. Brill, and M. Volk, "Wax Deposition in Single Phase Flow," *Fluid Phase Equilibria*, **158**, 801(1999).
- Davenport, T. C. and R.S.H. Somper, "The Yield Value and Breakdown of Crude Oil Gels," *J. Inst. of Pet.* **55**, 86-105 (1971)
- Davidson, M. R., Q.D. Nguyen, C. Chang, and H.P. Rønningsen, "A Model for Restart of a Pipeline with Compressible Gelled Waxy Crude Oil," *J. Non-Newt. Fluid Mech.* **123**(2-3), 269-280 (2004)
- Dirand, M., V. Chevallier, E. Provost, M. Bouroukba, and D. Petitjean, "Multicomponent Paraffin Waxes and Petroleum Solid Deposits: Structural and Thermodynamic State," *Fuel* **77**, 1253 (1998).
- Hausen, H., "Darstellung des Wärmeüberganges in Rohren durch Verallgemeinerte Potenzbeziehungen," *VDI Z.*, **4**, 91 (1943).
- Hénaut, I., O. Vincke, and F. Brucy, "Waxy Crude Oil Restart: Mechanical Properties of Gelled Oils", 1999 SPE Annual Technical Conference and Exhibition, Houston, TX (1999)

- Kane, M., M. Djabourov, J.L. Volle, J.P. Lechaire, and G. Frebourg, "Morphology of Paraffin Crystals in Waxy Crude Oils Cooled in Quiescent Conditions and under Flow," *Fuel* **82**(2), 127 (2003)
- Lee, H.S., P. Singh, W.H. Thomason, and H.S. Fogler, "Waxy Oil Gel Breaking Mechanisms: Adhesive versus Cohesive Failure," *Energy and Fuel*, (2007), accepted
- Lund, H.-J., M.S. Thesis, University of Tulsa, 1998
- Majeed, A., B. Bringedal, and S. Overa, "Model Calculates Wax Deposition for N. Sea Oils," *Oil & Gas J* **88**, 63 (1990)
- Maurício, M.H.P., A.M. Teixeira, L.F.A. Azevedo, and S. Paciornik, "In-situ Optical Microscopy of Wax Crystallization," *Acta Microscopica* **12**, Supplement C, September 2003 XIX Congress of the Brazilian Society for Microscopy and Microanalysis
- Paso, K. Ph.D. Thesis, University of Michigan 2005
- Paso, K., M. Senra, Y. Yi, A.M. Sastry, and H.S. Fogler, "Paraffin Polydispersity Facilitates Mechanical Gelation," *Ind. Eng. Chem. Res.* **44**, 7242 (2005).
- Ribeiro, F.S., P.R.S. Mendes, and S.L. Braga, "Obstruction of Pipelines due to Paraffin Deposition during the Flow of the Crude Oil," *Int. J. Heat Mass Transfer* **40**, 4319 (1997).
- Rønningsen, H.P., "Rheological Behaviour of Gelled, Waxy North Sea Crude Oils," *J. Pet. Sci. Eng.* **7**, 177-213 (1992)
- Seider, E.N., and C.E. Tate, "Heat Transfer and Pressure Drop of Liquids in Tubes," *Ind. Eng. Chem.* **28**, 1429 (1936).
- Singh, P., H.S. Fogler, and N.R. Nagarajan, "Prediction of the Wax Content of the Incipient Wax-Oil Gel in a Flowloop: An Application of the Controlled-Stress Rheometer," *J. of Rheology* **43**, 1437 (1999)
- Singh, P., R. Venkatesan, H.S. Fogler, and N.R. Nagarajan, "Formation and Aging of Incipient Thin Film Wax-Oil Gels," *AIChE J.* **46**, 1059 (2000)
- Singh, P., R. Venkatesan, H.S. Fogler, and N.R. Nagarajan, "Morphological Evolution of Thick Wax Deposits during Aging," *AIChE J.* **47**, 6 (2000)
- Svendsen, J. A., "Mathematical Modeling of Wax Deposition in Oil Pipeline Systems," *AIChE J.* **39**, 1377 (1993).

- Thomason, W.H., "Start-Up and Shut-in Issues for Subsea Production of High Paraffinic Crudes," 2000 Offshore Technology Conference, Houston, TX (2000).
- Todi, S., Ph.D. Thesis, University of Utah, 2005
- Uhde, A., and G. Kopp, "Pipeline Problems Resulting from Handling of Waxy Crudes," *J. Inst. of Pet.* **57**(554), 63 (1971)
- Venkatesan, R. Ph.D. Thesis, University of Michigan 2003
- Venkatesan, R. and H.S. Fogler, "Comments on Analogies for Correlated Heat and Mass Transfer in Turbulent Flow," *AIChE. J.* **50**, 1623 (2004).
- Venkatesan, R., N.R. Nagarajan, K. Paso, Y.B. Yi, A.M. Sastry, and H.S. Fogler, "The Strength of Paraffin Gels Formed under Static and Flow Conditions," *Chem. Eng. Sci.* **60**(13), 3587-3598 (2005)
- Verschuur, E., A.P.D. Hartog, and C.M. Verheul, "Effect of Thermal Shrinkage and Compressibility on Yielding of Gelled Waxy Crude Oils in Pipelines," *J. Inst. of Pet.* **57**(554), 131 (1971)
- Vignati, E., R. Piazza, R.F.G. Visintin, R. Lapasin, P. D'Antona, and T.P. Lockhart, "Wax Crystallization and Aggregation in a Model Crude Oil," *J. of Phys.: Condens. Matter* **17**(45), 3651-3660 (2005)
- Visintin, R.F.G., R. Lapasin, E. Vignati, P. D'Antona, and T.P. Lockhart, "Rheological Behavior and Structural Interpretation of Waxy Crude Oil Gels," *Langmuir* **21**(14), 6240-6249 (2005)
- Wattana, P. Ph.D. Thesis, University of Michigan 2004
- Wardhaugh, L.T. and D.V. Boger, "The Measurement and Description of the Yielding Behavior of Waxy Crude-Oil," *J. Rheol.* **35**(6), 1121-1156 (1991)

CHAPTER III
WAXY OIL GEL BREAKING MECHANISMS:
ADHESIVE VERSUS COHESIVE FAILURE

Introduction

The production and transportation of highly waxy crude oil in a cold environment is challenging especially when the ambient, for example sea water, temperature is below the pour point temperature (ASTM D 5853) or gelation temperature (Venkatesan et al., 2002). At reservoir temperatures (above 65 °C) and pressures, wax molecules are soluble and exist in the crude oil as a liquid phase. However, during the transportation in a pipeline, the temperature of oil decreases below the wax appearance temperature due to the heat loss to the surroundings causing wax deposition. If the transportation in a pipeline is stopped due to a planned maintenance or an emergency situation such as severe weather conditions (Venkatesan et al., 2002) on the off-shore platforms (Fung et al., 2006; Thomason, 2000), the temperature and solubility of wax further decrease and wax molecules precipitate out of liquid phase in a static condition. If the crude oil in the pipelines is trapped (shut-in) for a certain period of time below the pour point temperature, the oil inside the pipeline becomes a wax-oil gel because of the interlocking of solid wax crystals (Paso et al., 2005). This gel can not be broken with the original steady state flow operating pressure applied before gelation (Thomason, 2000).

The structure of the wax-oil gel is believed to be an interlocking of various wax forms such as needles, plates and orthorhombic wax crystals which depend on the cooling rate, wax concentration and shear history (Dirand et al. 1998; Singh et al., 2000). Cazaux et al. (1998) investigated the gel structure using a X-ray diffraction (XRD), a small-angle X-ray Scattering (SAXS), a cross-polarized microscope (CPM) and a controlled stress rheometer (CSR). They reported the key parameters that determine the structure of wax-oil gel are the crystal shape (aspect ratio) and number density of wax crystals, both of which depend on the temperature and cooling rate. The size and shape of wax crystal in crude oil also depend on the shear rate (Kane et al., 2003; Venkatesan et al., 2005) and the asphaltene fraction (Venkatesan et al., 2003). Recently Visintin et al. (2005) and Vignati et al. (2005) reported that waxy gels have the characteristics of colloidal gels and the radius of gyration of the wax-oil gel changes with cooling rate. Because many factors determine the wax-oil gel properties, the wax-oil gels formed in pipelines may not be homogenous because of thermal and shear history in the axial and radial locations inside the field pipelines. For example, because of the faster cooling rate near the wall, the size and shape of wax crystals near the pipe wall will be different from those at the center of the pipeline. Furthermore, the volume decrease of a wax-oil gel during cooling can cause local voids in the gel (Hénaut et al., 1999). Verschuur et al. (1971) and Thomason (2000) described non-homogenous wax-oil gel formation in field pipelines and found that the non-uniform gel formation could significantly affect the pressure required for breaking the wax-oil gel.

Because of this complexity in yielding behavior of the wax-oil gel, many studies have been carried out to estimate the yield strength of the wax-oil gel for various

conditions and, ultimately, the pressure required to restart the gelled pipelines in the field (Borghetti et al., 2003; Chang et al., 1998; Chang et al., 1999; Davenport and Somper, 1971; Davidson et al., 2004; Rønningsen, 1992; Thomason, 2000; Uhde and Kopp, 1971; Verschuur et al., 1971; Wardhaugh and Boger, 1991). However, previous literature has reported that the reproducibility of measurement of the static yield strength obtained from the controlled stress rheometer and the model pipeline have been “extremely” low and inconsistencies exist between yield strength measuring techniques (Davenport and Somper, 1971; Wardhaugh and Boger, 1991). These inconsistencies have been attributed to differences in flow patterns (Couette and Poiseuille), compressibility of the wax-oil gel and pipe wall, and pressure propagation during the gel yielding in the pipeline (Borghetti et al., 2003; Wardhaugh and Boger, 1991). On the other hand, Rønningsen (1992) reported reasonably good agreement between the model pipeline experiments and the controlled stress rheometer. Rønningsen (1992) also reported the stress loading rate, cooling rate, and aging time significantly affect the yield stress and consequently these conditions should be consistently applied for both of the model pipeline and controlled stress rheometer experiments. These inconclusive contradicting experimental results have not been fully explained and thereby hampering the prediction of restart pressure of gelled pipeline by using the controlled stress rheometer (Borghetti et al., 2003; Davenport and Somper, 1971; Rønningsen, 1992; Wardhaugh and Boger, 1991). One of the objectives of this study is the clarification of this inconsistency by providing the agreement between the model pipeline and the controlled stress rheometer if the gel fails adhesively and the gel has been formed as a continuous gel under a hydrostatic head during cooling and aging period.

Pressure propagation during the startup process has been an important issue since 1960-1970's. Literature data (Borghi et al., 2003; Davenport and Somper, 1971; Rønningsen, 1992; Uhde and Kopp, 1971; Verschuur et al., 1971) and field observations (Thomason, 2000) confirm the pressure propagation (wave) in a gelled pipeline during the gel breaking process is an important element during restart. The speed of the sound in the wax-oil gel may be slower than that in the pure liquid oil phase depending on the void fraction in the gel (Vinay et al., 2007). Recently Borghi et al. (2003) experimentally showed that the pressure propagation speed in a pipeline during the gel breaking process is slower than the speed of sound. The pressure propagation speed will be low if the injection flow rate is low (in other words, no pressure pulse), which is valid in most field situations. Under these conditions the pipeline can be divided as two sections (Borghi *et al.*, 2003): (1) Linear pressure profile from inlet to $\zeta(t)$ and (2) constant baseline pressure P_0 from $\zeta(t)$ to exit as shown in Figure 3.1. As time progresses and the inlet pressure increases the pressure front travels down to the exit of the pipeline.

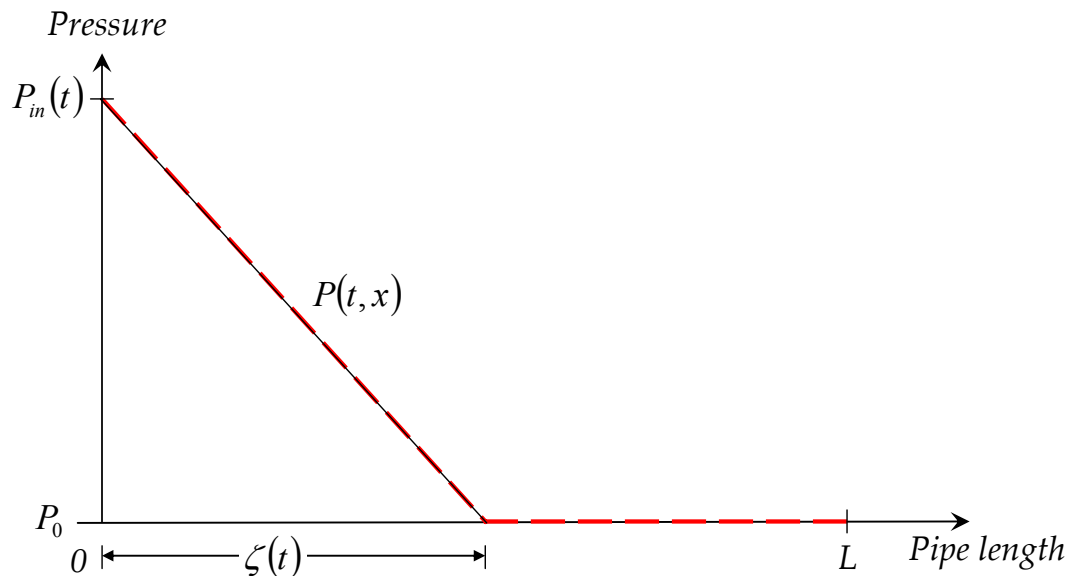


Figure 3.1: Schematic of pressure propagation during restart (modified from experimental results by Borghi et al. (2003)).

In this research, excellent agreement was observed between the two yield stress measurement techniques (the model pipeline system and the controlled stress rheometer system) when the gel is slowly cooled and the wax-oil gel is well aged. Further, microscopic observations and controlled stress rheometer experiments allowed us to observe both cohesive failure and adhesive failure, both of which depend on the cooling rate. Thirdly, we developed a relationship between inlet pressure and injection volume using the compressibility of wax-oil gel.

Experimental Section

Material Used

A model wax-oil mixture was prepared for both of the model pipeline system and the controlled stress rheometer. The model wax-oil mixture is composed of 15% of food grade paraffin (Gulf Wax[®]), 33% of Kerosene and 52% of mineral oil by weight. The molecular weight distribution of the model wax-oil mixture was obtained by an Agilent Technologies 6890N high temperature gas chromatograph (HTGC) and is shown in Figure 3.2. The wax appearance temperature (WAT) and the pour point temperature of the model wax-oil were determined to be 25 °C and 20 °C, respectively using ASTM D5853. The composition of the model wax-oil mixture was chosen to set the pour point temperature close to the room temperature thereby mimicking highly waxy crude oils.

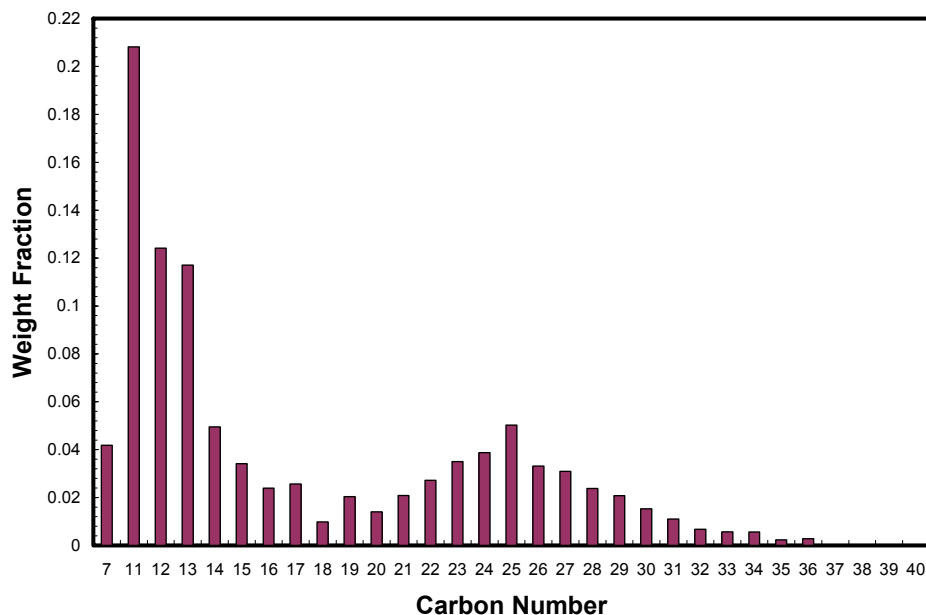


Figure 3.2: Carbon number distribution of the model wax-oil mixture.

Model pipeline system

A lab-scale pipeline system was constructed to determine the required gel breaking pressure of the gelled pipeline as shown in Figure 3.3. The model pipe, a U-shaped stainless steel tube (ID = 0.77 cm, L = 3.77 m), was installed in a water bath. The temperature was initially set above 40 °C and was lowered at a given cooling rate using a programmable temperature controller. The cooling rate of the wax-oil gel was set very low (3.5 °C/hr) to mimic a slow natural cooling situation in a field pipeline. Due to the low cooling rate and small diameter of the model pipeline, the wax-oil gel can be cooled down homogeneously. In field situations the cooling rate can be lower than 3.5 °C/hr; however the oil gel in field situations may be inhomogeneous due to the large pipe length and diameter and variation of the sea floor temperature.

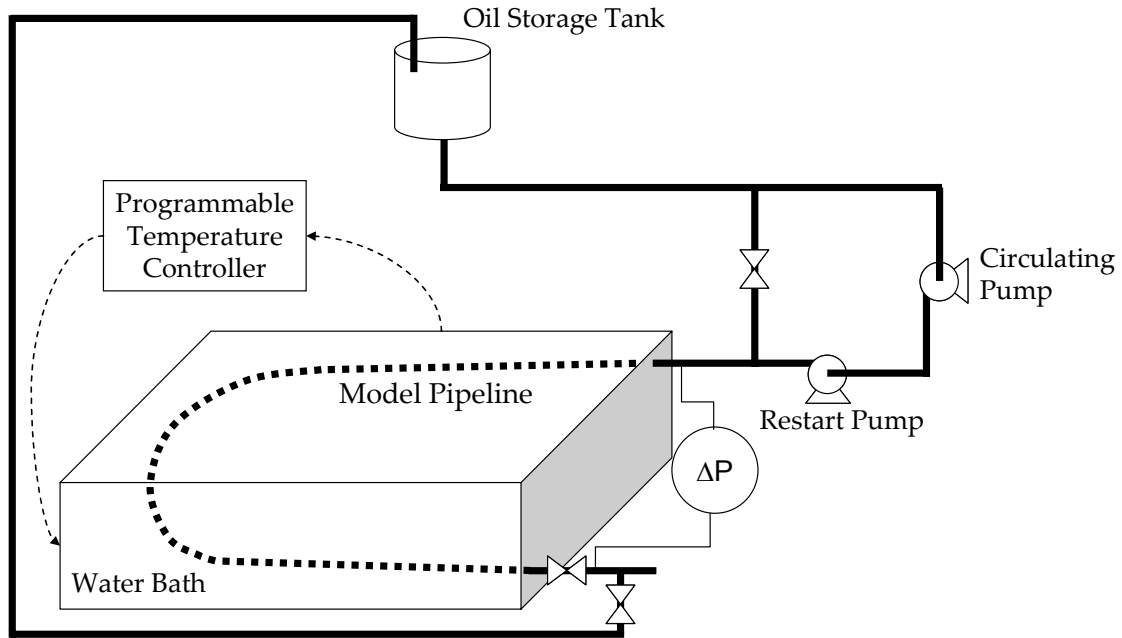


Figure 3.3: Schematic of the model pipeline system.

In order to avoid gel fragmentation resulting from volume reduction (Verschuur et al., 1971) during the gelation, the model pipeline was slightly (about two degrees) declined toward the outlet and connected to the oil storage tank to apply hydrostatic head during the cooling (about 7 hours) and the aging (at least 10 hours) periods. It is notable that the effect of hydrostatic head on the restart pressure was proven to be significant in our system as the gel breaking pressure decreased 50% when the model pipeline was restarted without a hydrostatic head during the cooling and aging period. The reasons for this 50% decrease when there is no hydrostatic head are the creation of discontinuous gel segments and the increased voids in the gel which increase the compressibility of gel.

The aim of this study is to develop an experimental technique and a model to predict the gel breaking and restart pressure for actual offshore pipelines connected to risers. The fluid column inside the offshore risers applies a significant hydrostatic pressure on the fluid in the subsea pipeline during the shut-in period. Therefore the

volume reduction in the subsea pipeline would also occur during gelation similar to our experimental conditions. For on-shore pipelines which are not the focus of this work, however, this experimental condition may not be applied if there is no hydrostatic pressure on the pipeline crude during gelling.

Two pumps were used in the model pipeline system: A Cole-palmer[®] peristaltic pump (maximum flow rate is 800 ml/min) for the transportation of sample oil and a Ruska[®] positive displacement pump (total volume is 100 ml) for the gel breaking. The Cole-palmer[®] peristaltic circulating pump was used to load the oil sample into the pipeline. The water bath and storage tank temperature were maintained higher than the wax appearance temperature while the oil was circulated at 40 °C for at least five minutes in order to avoid wax precipitation/deposition during the sample loading. After the cooling and aging periods, the exit valve was opened and the pressure was applied at the inlet of the pipeline using the Ruska[®] pump. The injection rate was stepwise with 0.1 ml injected every 10 seconds.

Controlled stress rheometer

The gel failure stress was measured with a constant stress rheometer (Haake[®] Model RS150) with a concentric (Couette) geometry and a temperature control system. The wax-oil sample could be kept in a closed system to avoid any loss of light paraffin components of the sample through the use of a magnetic coupling device.

The operating procedure of the constant stress rheometer was equivalent to that of the model pipeline system. After loading the sample in the constant stress rheometer chamber, the sample was heated to a temperature well above the cloud point temperature

(around 40 °C) to erase any thermal history. A high shear rate (300 s^{-1}) was then applied to the sample for about 30 minutes. Next, the temperature was lowered below the pour point temperature at a pre-specified cooling rate, and then was kept constant to allow the gel network to mature (Rønningsen, 1992). After the aging period, a shear stress ramp was applied until the break. The shear rate of the sample was monitored to find the breaking point of the gel. The breakage was considered to have occurred when the shear rate starts to increase rapidly.

Results and Discussion

Model pipeline experiments

The pressure at the inlet of the model pipeline was increased by the known injection of oil in a stepwise manner, thereby allowing the time scale in the x axis in Figure 3.4 to be easily converted to the volume of oil injected into the model pipeline. Figure 3.4 shows typical results of gel breaking experiments after cooling and aging at two temperatures $T=12.7 \text{ °C}$ and $T=15.1 \text{ °C}$. By comparing two different experimental results for the same temperature, we could confirm the reproducibility of the experiments is good ($\pm 10\%$) compared to that of the previous literature ($\pm 20\%$) (Rønningsen, 1992; Wardhaugh and Boger, 1991).

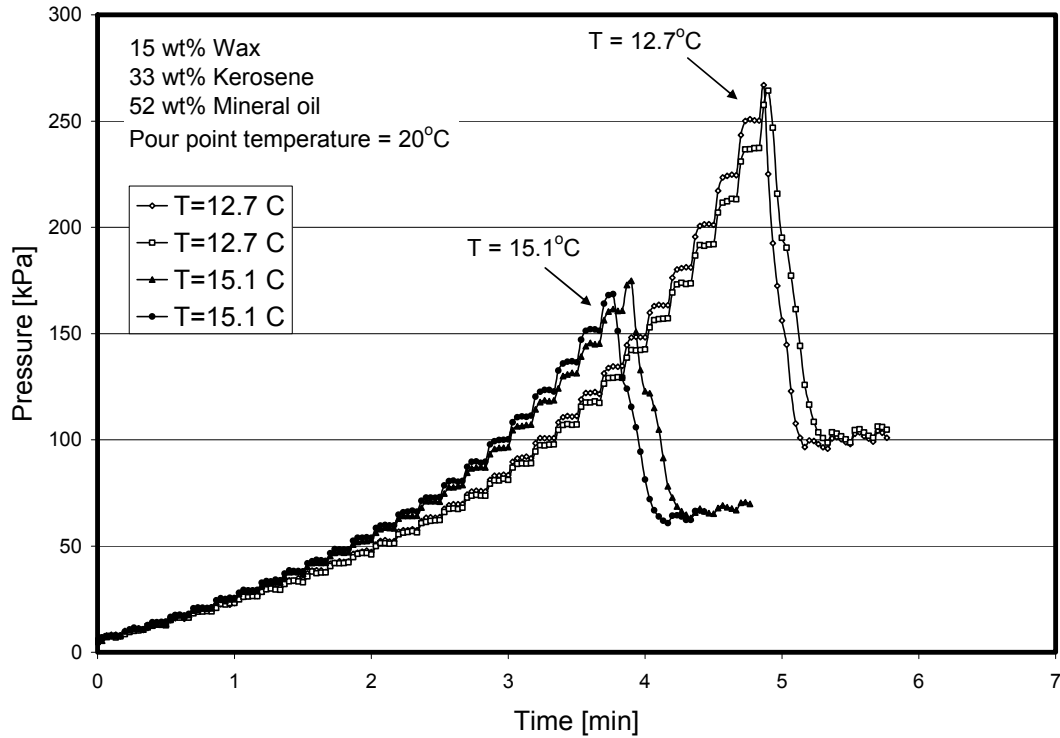


Figure 3.4: Typical gel breaking experimental results with different gel temperatures.

The volume of oil required for the gel breaking is about 2 - 4 ml (about 2% of the gel volume in the model pipeline) depending on the gel temperature. One observes that the gel breaks at 172.4 kPa at 15.1 °C and at 262.0 kPa at 12.7 °C. The restart pressure would increase further as the gel cools down to lower temperatures such as those near sea floor temperatures, typically 4 °C to 16 °C (Cawkwell and Charles, 1987).

Figure 3.4 reveals an important aspect of wax-oil gel compression. In this experiment, the injected oil compresses the gel as a piston at the interface between incoming liquid and gelled sample. No significant liquid penetration was observed through any continuous axial channels, because if there was penetration the inlet pressure could not be maintained constant and would decrease due to the penetration during the intervals of the step injection (Verschuur et al., 1971). No pressure release was observed

due to any liquid penetration for various gel temperatures (12 °C to 16 °C) and wax concentrations even at high pressures close to the gel yielding. In this study a pressure decrease was observed only after the gel ruptures and the broken gel begins to move. The details of this compression during the gel breaking process will be discussed and mathematically incorporated in the restart model in the following modeling section. One important point in Figure 3.4 is that the gel breaking can be described as a fast and drastic phenomenon that occurs in the entire pipeline at the same time in this system.

After gel breaking, the pressure reaches a remnant value required for flow in the pipe clearing process. Note that the pressure during the clearing process depends on the friction between broken gel and pipe wall and on the length of the gel remaining in the pipe after gel breaking. There is also a possibility of the gel structure recovery during the clearing step because of the continuation of the heat loss to the cold surrounding. This recovery is particularly feasible when the pour point temperature is much higher than the bath temperature and flow rate is not sufficiently high enough to overcome the gel structure recovery. In order to achieve a steady state pressure condition during displacement of the gel, the amount of oil injected should be 150-200% of the total volume of the gel according to a rule of thumb observed in the field (Thomason, 2000).

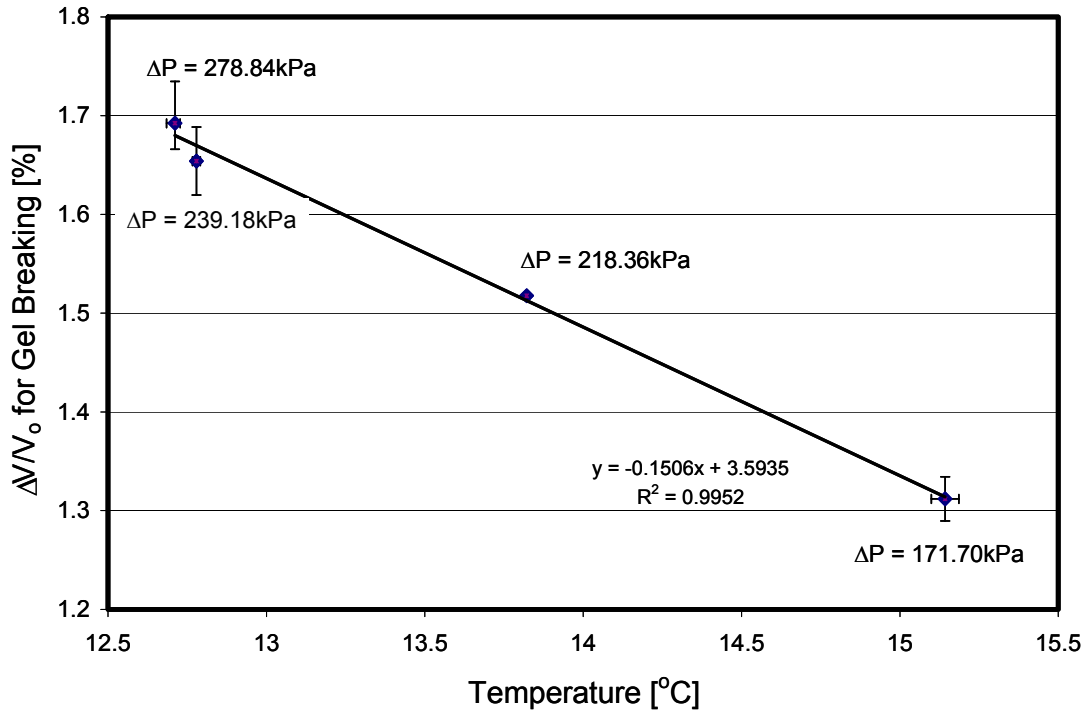


Figure 3.5: Gelation temperature vs. volume required to break the gel.

Figure 3.5 shows the percentage decrease in gel volume at the point of gel rupture. One observes in Figures 3.4 and 3.5 that at the lower temperatures the gel is more compressible and/or deformable for the same applied pressure (Hénaut et al., 1999; Venkatesan et al., 2005). The increase of volume change during the restart process at lower temperature is due to the increase of voids in the gel resulting from the volume reduction during gelation at lower temperature and additional pressure required to break and compress the gel at lower temperature. Zhu et al. (2005) reported the isobaric compressibility $\alpha(T, P) \equiv 1/V_m (\partial V_m / \partial T)_P$ of organic liquids such as trans-decahydronaphthalene ($C_{10}H_{18}$) and showed the volume reduction of $C_{10}H_{18}$ for a temperature decrease from 40 °C to 0 °C is about 4%. Hénaut et al. (1999) also reported that the shrinkage results in the void spaces which can be varied in various shapes and

sizes depending on the cooling rate and temperature. For example, they reported for a waxy crude oil sample at high pressures ($P > 700$ kPa), the void spaces were 8% of the total volume of the gel at $T=23$ °C and 12% at $T=8$ °C. They also reported that the volume reduction in low pressure regime ($P < 280$ kPa) was reported to be less than 5% which is consistent with the present experimental results.

Gel failure mechanism

As discussed in the previous section, the restart pressure and gel strength depend on the cooling rate under quiescent conditions (Venkatesan et al., 2005). If the cooling rate is low, wax molecules have sufficient time and mobility to form large crystals and as a result the number density of crystals decreases. This crystal morphology affects the strength of the gel and the failure mechanism of the gel in the pipeline and rheometer experiments (Venkatesan, 2003). For example, the restart of the gelled oil may result from the breakdown of the gel structure itself (cohesive failure) or it may occur because of the breakage at the pipe-gel interface (adhesive failure) (Venkatesan, 2003). The cohesive yielding of the gel occurs when the applied stress exceeds the mechanical strength of the wax-oil gel structure maintained by the mechanical interlock of wax crystals formed by London dispersion or van der Waals forces of n-alkanes (attractive potential proportional to r^{-6}) (Venkatesan et al., 2005; Vignati et al., 2005; Visintin et al., 2005). Using a plate-plate rheometer with grooved surfaces Venkatesan (2005) has reported the decrease of cohesive failure strength and the increase of adhesive failure strength as the cooling rate increases and an existence of a delineation point between cohesive and adhesive failure.

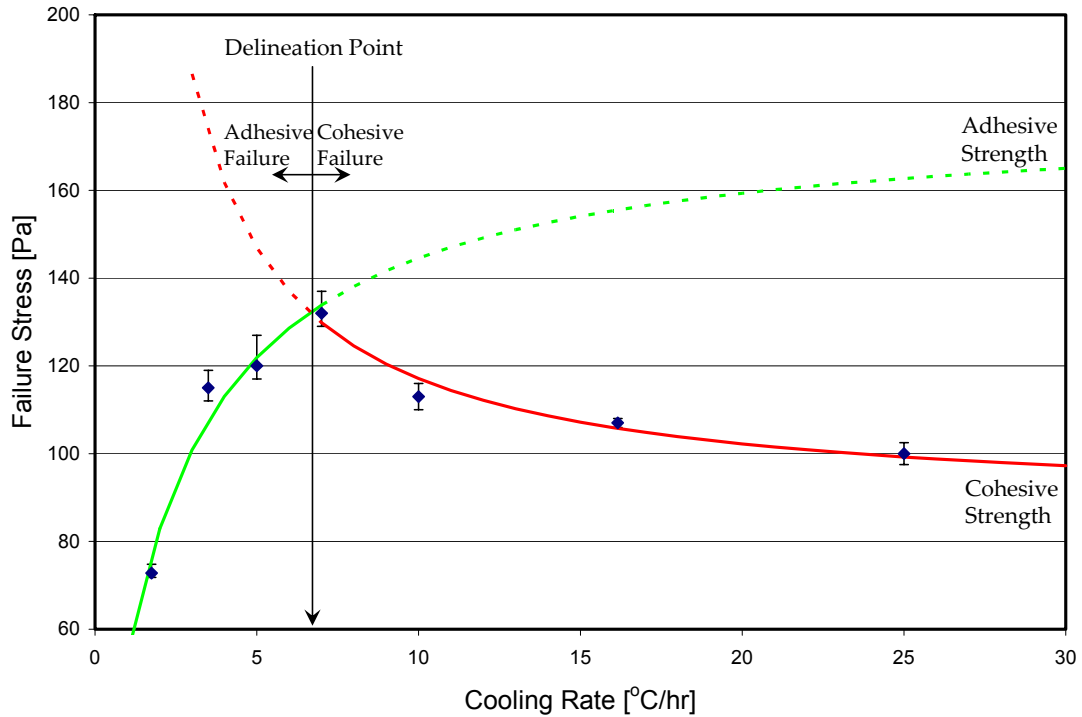
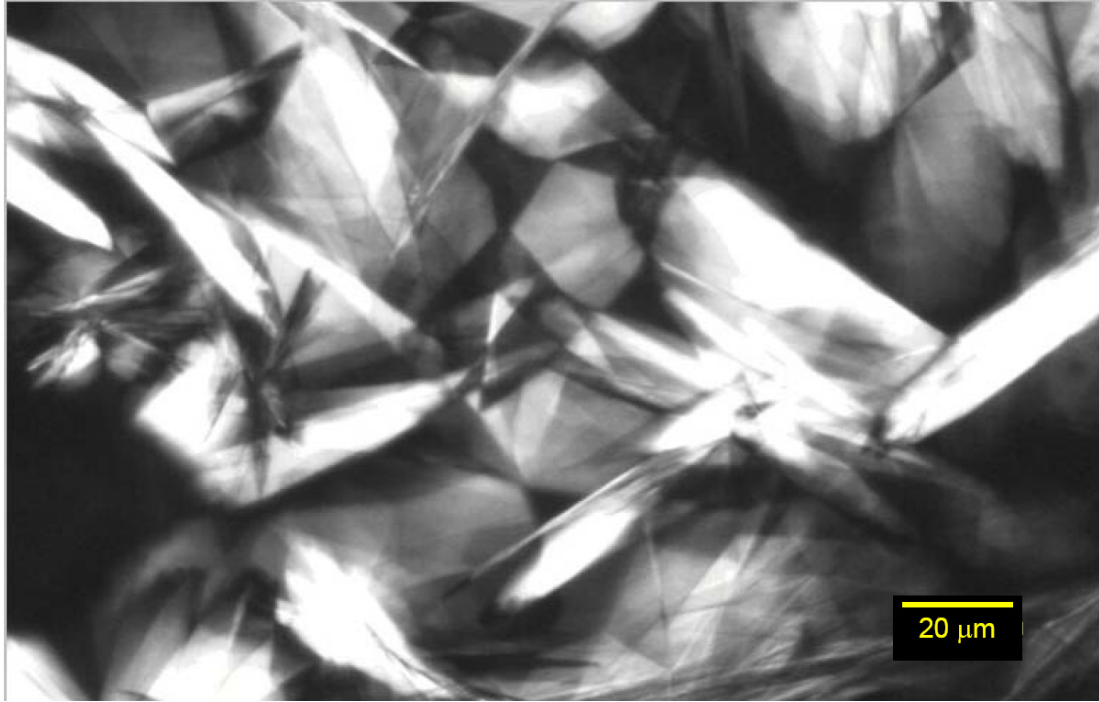


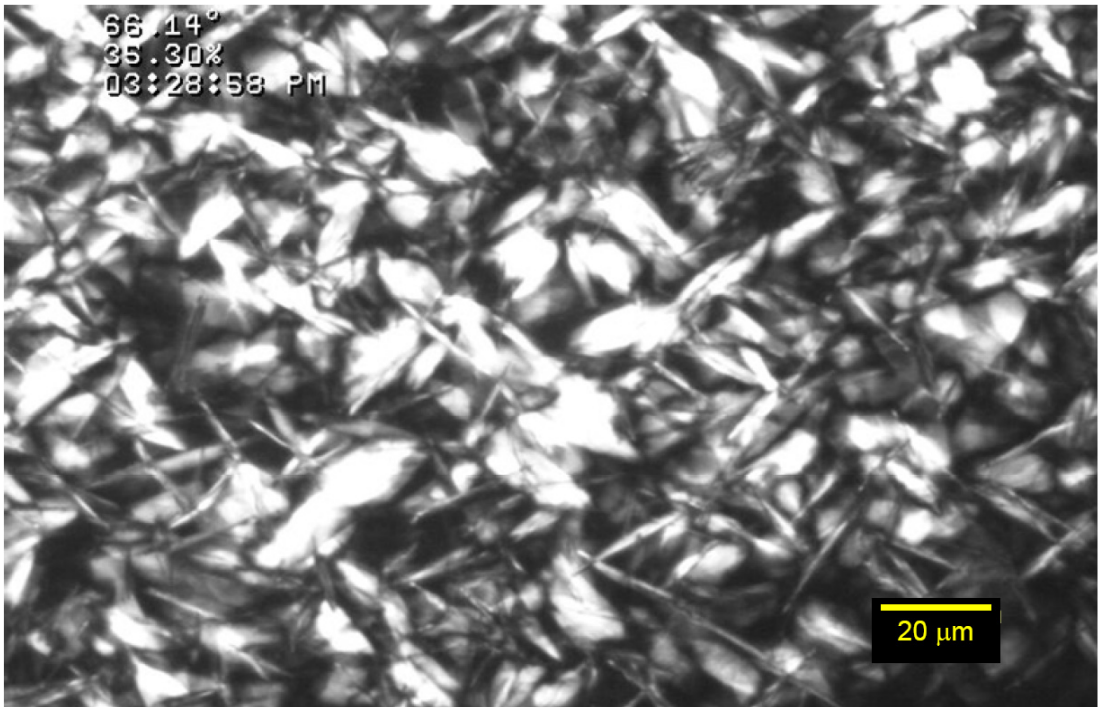
Figure 3.6: Gel failure stress vs. cooling rate obtained by the controlled stress rheometer.

In order to further investigate the failure mechanism, we measured the wax-oil gel failure strength with the constant stress rheometer for various cooling rates as shown in Figure 3.6. The results in Figure 3.6 show that the gel failure strength increases with increasing cooling rates at low cooling rates and decreases at high cooling rates and there is a delineation point between two (Venkatesan, 2003).

When the cooling rate is below the delineation point (about 7 °C/hr in this particular system), the cohesive gel strength is much larger (brittle) than adhesive failure strength, and the gel breaks adhesively at the interface between metal surface and gel network. If the cooling rate is higher than the delineation point, the cohesive strength becomes smaller than the adhesive strength; the gel breaks within the gel structure cohesively.



(a) Cooling rate = 3.5 °C/hr



(b) Cooling rate = 20 °C/hr

Figure 3.7: Cross-polarized microscope photo of wax-oil gel at (a) $T=19.1$ °C under cooling rate of 3.5 °C/hr (b) $T=19.0$ °C under cooling rate of 20 °C/hr.

The photographs of the wax-oil gel structures in Figures 3.7 (a) and (b) for two different cooling rates ((a) 3.5 °C/hr and (b) 20 °C/hr) were compared using the cross-polarized microscope to help elucidate the relationship between failure stress and cooling rate. At the lower cooling rate the wax crystals are larger and the shape of crystal is sheet-like (average surface area of the crystals is 20 $\mu\text{m} \times 50 \mu\text{m}$). On the other hand, at the higher cooling rate, the number density of crystals is increased but the crystal sizes are smaller and the shape of crystal is needle-like (average surface area of the crystals is 1 $\mu\text{m} \times 20 \mu\text{m}$).

These observations help explain the decrease of cohesive strength and the increase of adhesive strength as the cooling rate increases shown in Figure 3.6. As we increase the cooling rate, the size of wax crystals decreases and, as a result, the network of wax-crystal structure loses its interconnectivity. At the same time, the crystal shape becomes more needle-like and the number density of crystals increases as we increase the cooling rate. The increased number density of crystals and the needle-like morphology result in the increase of adhesive strength as the needle-like crystals allow larger effective surface area at the interface between gel and wall (Greiner et al., 2007). These observations are consistent with those of Longhenry et al. (1997), who observed a lower “crack growth rate” at the interface between Polychlorotrifluoroethylene (PCTFE)/PCTFE copolymeric films and microwave circuits under fast cooling rates. All the gel breaking experiments, except those in Figure 3.6, have been performed under a fixed cooling rate (3.5 °C/hr) which is in the adhesive failure regime. Consequently, the gel failures in the discussion that follows were adhesive failure.

Comparison between model pipeline and controlled stress rheometer

Figure 3.8 shows the restart pressure obtained directly from the model pipeline experiment and from the constant stress rheometer. The yield stress, τ_y , measured by the controlled stress rheometer system was converted to the restarting pressure using the following relationship (Thomason, 2000).

$$\text{Break Pressure} = \frac{\text{Break Force}}{\pi R^2} = \frac{\text{Failure Strength} \times 2 \times \pi \times R \times L}{\pi R^2} \quad (3.1)$$

$$\Delta P = \frac{4L}{D} \tau_y$$

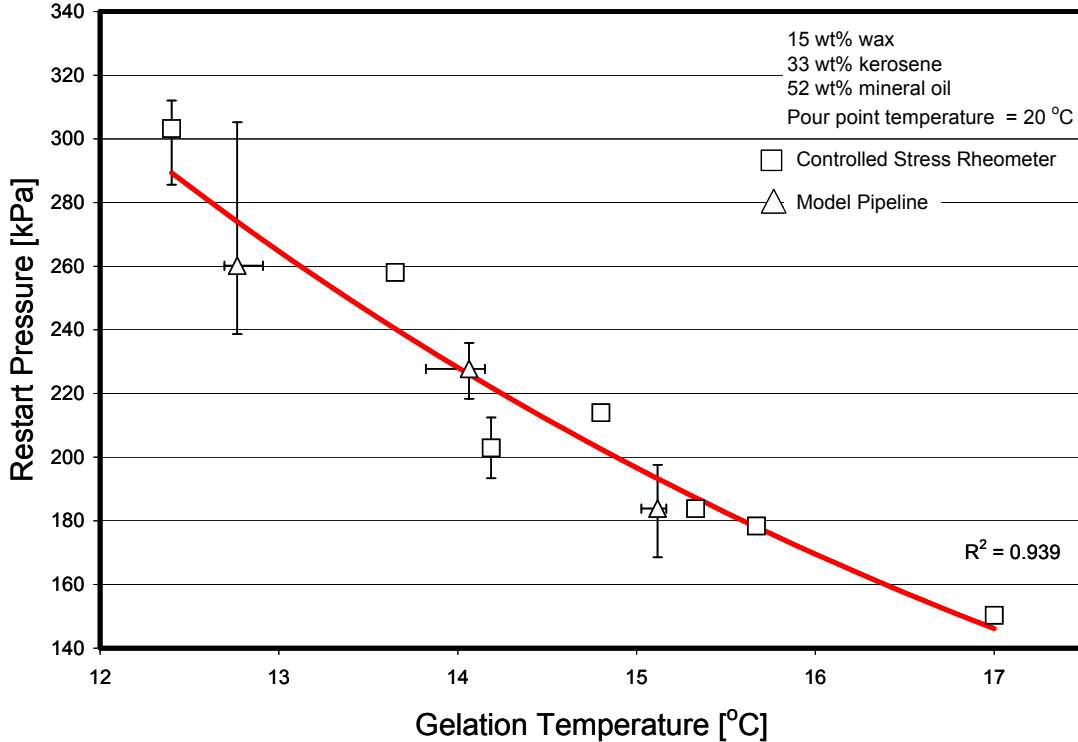


Figure 3.8: Restart pressure obtained by model pipeline and controlled stress rheometer.

The restart pressure predicted using Equation (3.1) from the controlled stress rheometer shown in Figure 3.8 is in good agreement with the restart pressure obtained from the model pipeline experiments. Although Equation (3.1) is based on an assumption

that the gel breaking occurs at the pipeline wall it has successfully predicted the restart pressure of gelled pipeline based on yield stress measurements by rheometer experiments (Davenport and Somper, 1971; Thomason, 2000; Uhde and Kopp, 1971). Thomason (2000) has reported that Equation (3.1) is valid if the failure is an adhesive failure at the pipe wall. While the flow characteristics of the controlled stress rheometer are of a Couette type instead of pipe flow (Poiseuille type), the controlled stress rheometer can successfully be used to predict the restart pressure if the failure mechanism is adhesive failure for both cases. If the failure mechanism between two cases were not consistently same, the pressure drop predicted by the controlled stress rheometer and Equation (3.1) would be larger than that of model pipeline experiments as reported in Venkatesan's thesis (Venkatesan, 2003).

Restart Model

In the present research two key unknowns to describe a gel breaking process in a pipeline have been discussed: the restart pressure and the amount of injected fluid required to break the gel. The previous section described how the restart pressure could be predicted by using Equation (3.1) and the controlled-stress rheometer study for the case of adhesive gel breaking. The amount of injected fluid required for gel breaking can be estimated using model pipeline experiments (Figures 3.4 and 3.5) and the compressibility of the wax-oil gel. Highly waxy oil is generally more compressible due to the fact that the shrinkage during the gelation results from a phase change of wax molecules. The compressibility of the wax-oil gel is also a function of temperature and pressure. For example, hydrostatic pressure applied to the gel can minimize the voids in

the gel generated by the volume reduction that occurs during the cooling and aging periods. In this section, we describe a model that predicts the pressure profile in the pipeline during the gel breaking as a function of injected oil volume for the case that the voids in the gel is minimized due to the hydrostatic head.

Pressure propagation

Data from the literature (Borghi et al., 2003; Davenport and Somper, 1971; Ronningsen, 1992; Uhde and Kopp, 1971; Verschuur et al., 1971) and field operations (Thomason, 2000) confirm the pressure propagation (wave) in the gelled pipeline is an important process during restart. The gel compression due to the applied pressure induces both **displacement** and **deformation** of the gel (Verschuur et al., 1971) as shown in Figure 3.9.

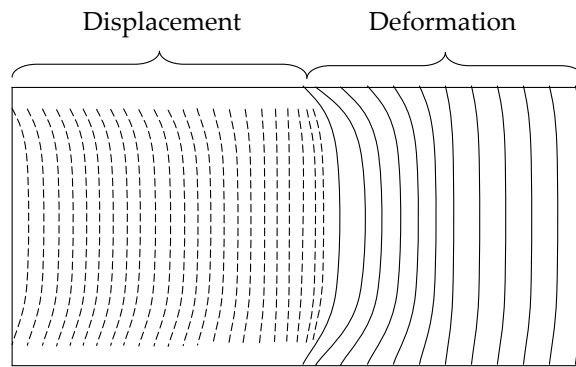


Figure 3.9: Sketch of compressed gel due to an applied pressure both of displacement and deformation.

The **displacement** due to the injection essentially requires yielding inside the gel (cohesive failure) followed by breaking at the interface between the gel and the pipe wall (adhesive failure) in order to accommodate the dislocation. Unlike **displacement**, the **deformation** of the gel occurs without yielding at the gel-wall interface (Verschuur et al., 1971). Depending on the gel structure and the applied pressure, the pressure can

propagate down the pipe outlet either by the deformation or the displacement of the gel (Verschuur et al., 1971). In the following paragraphs, we discuss two gel breaking scenarios: (1) inlet pressure is increased instantaneously and maintained at a constant value greater than a restart pressure, and (2) inlet pressure is increased gradually as a function of time from a baseline pressure to the restart pressure.

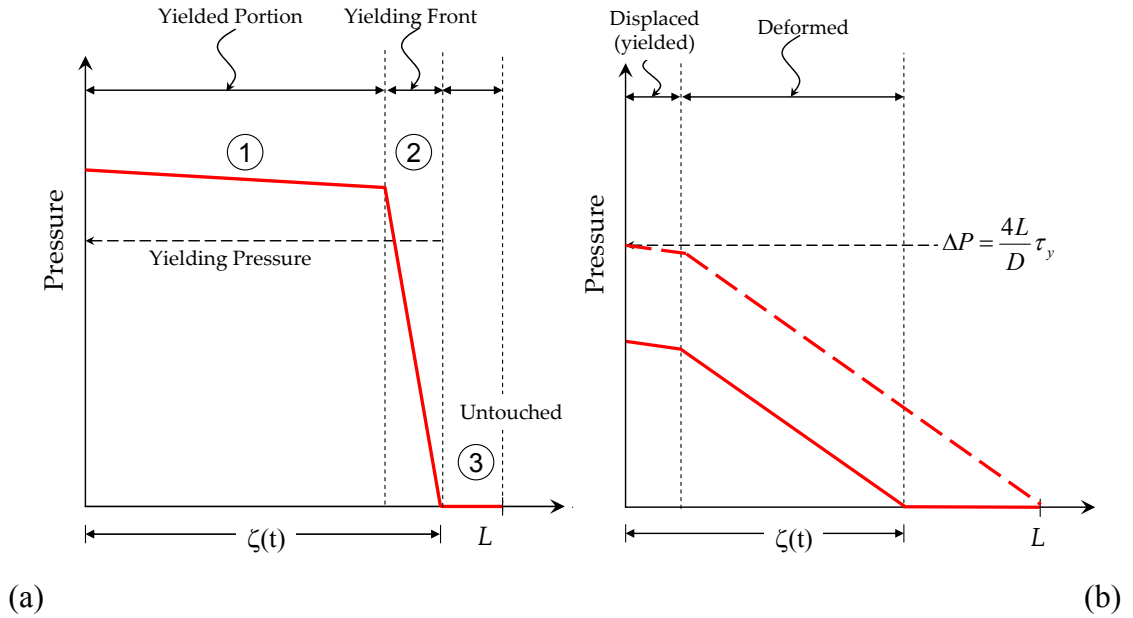


Figure 3.10: (a) P_{in} is constant and greater than $\Delta P_{restart}$, (b) P_{in} as a function of time.

First consider the case where the inlet pressure is instantaneously increased to a pressure and greater than a restart pressure and then maintained constant at a time t after this jump, the gel in the pipeline can be represented by three sections as a snapshot as shown in Figure 3.10 (a). These sections are (1) the yielded portion, (2) the yielding front, and (3) the undisturbed section from $\zeta(t)$ to L (Vinay et al., 2006, 2007). The axial pressure gradient in the **yielded portion** ① is much smaller than that of the **yielding front** because the gel structure or the gel-wall adhesion has been broken, thereby, significantly reducing the pressure drop. In the yielding front section ζ , the pressure

changes significantly from the inlet pressure in the yielded portion to the baseline pressure in the undisturbed section. In this scenario, due to the significant pressure gradient in the yielding front section, the pressure front is expected to propagate much more rapidly than the following scenario.

Next consider the case where the inlet pressure increases gradually as a function of time from a baseline pressure at the start of compression, P_0 to a restart pressure, P_{yield} . Under these conditions, the axial pressure profile can be described as Figure 3.10 (b). In Figure 3.10 (b), the solid line is a pressure profile at time t , and the dashed line is the pressure profile established just before restart occurs as shown in the Figure 3.10 (b). Gel structure will be broken in the **displaced portion** by the injected oil and as a result the pressure gradient in this portion will be low because of the loss of adhesion at the gel-wall interface. The displaced portion at the restart is about 2% of the total volume of the pipeline in this study. The pressure gradient in the **deformed portion** is higher than the displaced portion because the gel structure and the gel-wall interface are not broken. The axial pressure profile and pressure propagation given in Figure 3.10 (b) are due to the deformation of the gel under an applied pressure which is lower than the yielding pressure. In this case, the gel breaking occurs at the same time in the entire gel when $\zeta(t)$ reaches the exit of the pipeline and the pressure drop across the pipe reaches the restart pressure $P_{yield} = 4L / D\tau_y$.

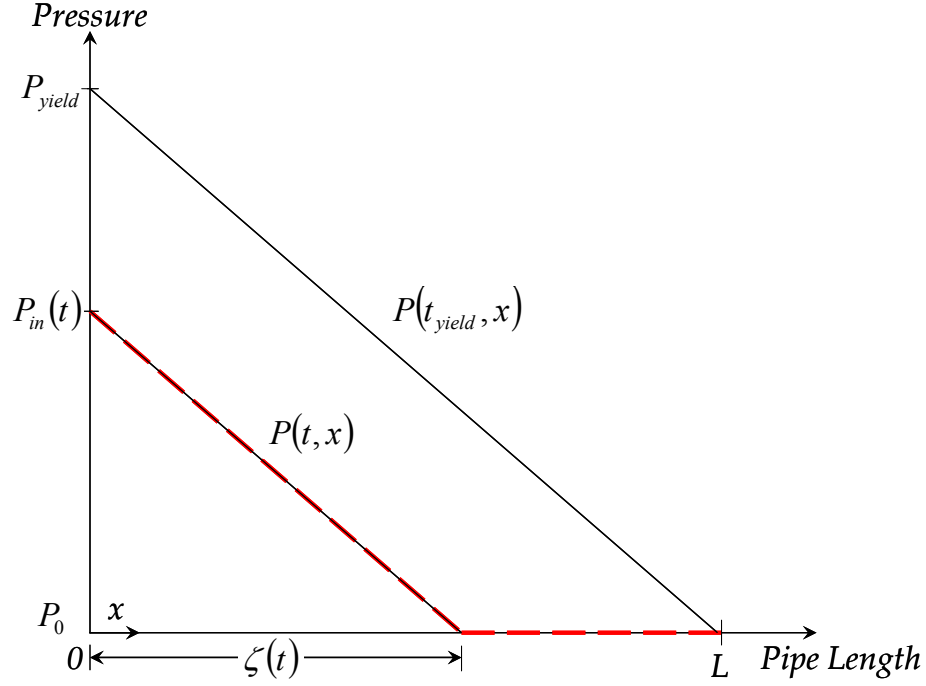


Figure 3.11: Schematic of pressure propagation during restart (modified from experimental results by Borghi et al. 2003).

We may assume the length of displaced section is negligible for the gel breaking modeling purpose because the injection volume is about 2% of total volume of the pipeline, and the simplified axial pressure profile can be shown as Figure 3.11 (Borghi et al., 2003). For any time t , the pressure inside the gelled pipeline at any position x between 0 to $\zeta(t)$ is

$$P(t, x) = P_{in}(t) - \frac{P_{yield}}{L} x \quad 0 < x < \zeta(t) \quad (3.2)$$

where $P_{in}(t)$ is inlet pressure at time t and P_{yield} is the yielding pressure which can be measured by rheometer as described in the previous section (Figure 3.8 and Equation (3.1)), and x is the axial coordinate. If we assume that the pressure gradient is invariant with time t , the location of the pressure front, $\zeta(t)$, can be obtained as

$$\zeta(t) = \frac{P_{in}(t)}{P_{yield}} L \quad (3.3)$$

The assumption used in Equation (3.3) is valid when the inlet pressure is increased slowly (and the resulting pressure wave front propagates at a speed slower than the speed of sound), as is the case for field conditions and for our model pipeline experiments. The gradient is also invariant when the wax-oil gel is homogenous. The amount of oil injected is given by

$$\Delta V(t) = \int_{P_0}^{P(t,x)} V_0 \frac{\partial(V/V_0)}{\partial P} dP(t,x) = V_0 \frac{1}{\zeta(t)} \int_0^{\zeta(t)} \frac{\Delta V(P(t,x))}{V_0} dx \quad (3.4)$$

where $\Delta V(P)$ is the compressed volume due to the applied pressure and V_0 is the total volume of gel in the pipeline. The gel inside the pipeline is compressed as pressure is applied to the gel, and the average volume change from inlet to the location of the pressure front, $\zeta(t)$, due to the applied pressure $P_{in}(t)$ as given in Equation (3.2). The derivative of $(\Delta V(P)/V_0)$ in Equation (3.4) with respect to pressure is the compressibility factor of gel. Hayward (1967) reported the volume change of a crude oil as a function of pressure and the relationship follows a simplified version of the Tait equation.

$$\frac{\Delta V(P)}{V_0} = \frac{aP}{b+P} \quad (3.5)$$

Compression in the model pipeline

Hénaut *et al.*, (2003) provided a relationship between the volume change and applied pressure for a waxy crude oil as shown in Figure 3.12. Once the gel is completely compact, its volume remains constant even if the pressure is increased further, and the

compressibility of the gel approaches the compressibility of oil. The pressure - volume-change relationship of Hénaut et al., (2003) can be described by Equation (3.5).

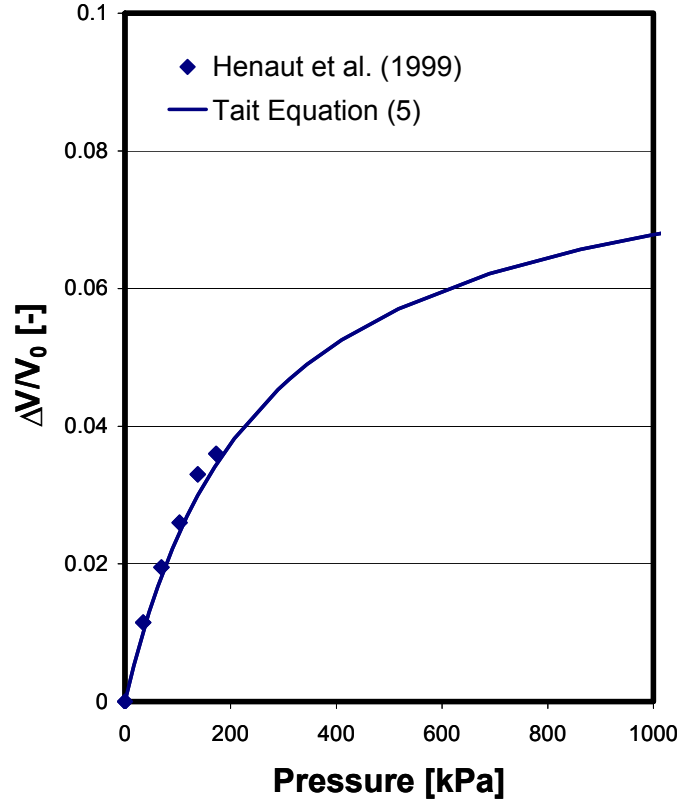


Figure 3.12: Volume change of waxy oil due to the applied pressure presented in Hénaut et al (2003) and Tait equation (Hayward, 1967) given in Equation (3.5).

Regression of Hénaut et al (2003)'s experimental data using Equation (3.5) gave the Tait equation parameters a as 0.051 (dimensionless) and b as 80.952 (kPa).

Substituting Equation (3.5) into Equation (3.4) yields

$$\Delta V(t) = \frac{\pi D^2 L}{4} \frac{1}{\zeta(t)} \int_0^{\zeta(t)} \frac{aP(t,x)}{b + P(t,x)} dx. \quad (3.6)$$

By using Equation (3.2), we can change the independent variable x into applied pressure $P(t,x)$ in order to integrate Equation (3.6).

$$\Delta V(t) = \frac{\pi D^2 L}{4} \frac{L}{P_{yield}} \frac{1}{\zeta(t)} \int_{P_0}^{P_{in}(t)} \frac{aP(t,x)}{b+P(t,x)} dP \quad (3.7)$$

Integrating Equation (3.7) as follows,

$$\Delta V(t) = \left(\frac{\pi D^2 L}{4} \right) \left(\frac{a}{P_{in}(t)} \right) \left[P_{in}(t) + b \ln \left(\frac{b}{P_{in}(t) + b} \right) \right] \quad (3.8)$$

Figure 3.13 shows good agreement between the model pipeline experimental data and our model Equation (3.8). The restart pressure is predicted by using Equation (3.1) and the yield stress obtained from the controlled stress rheometer.

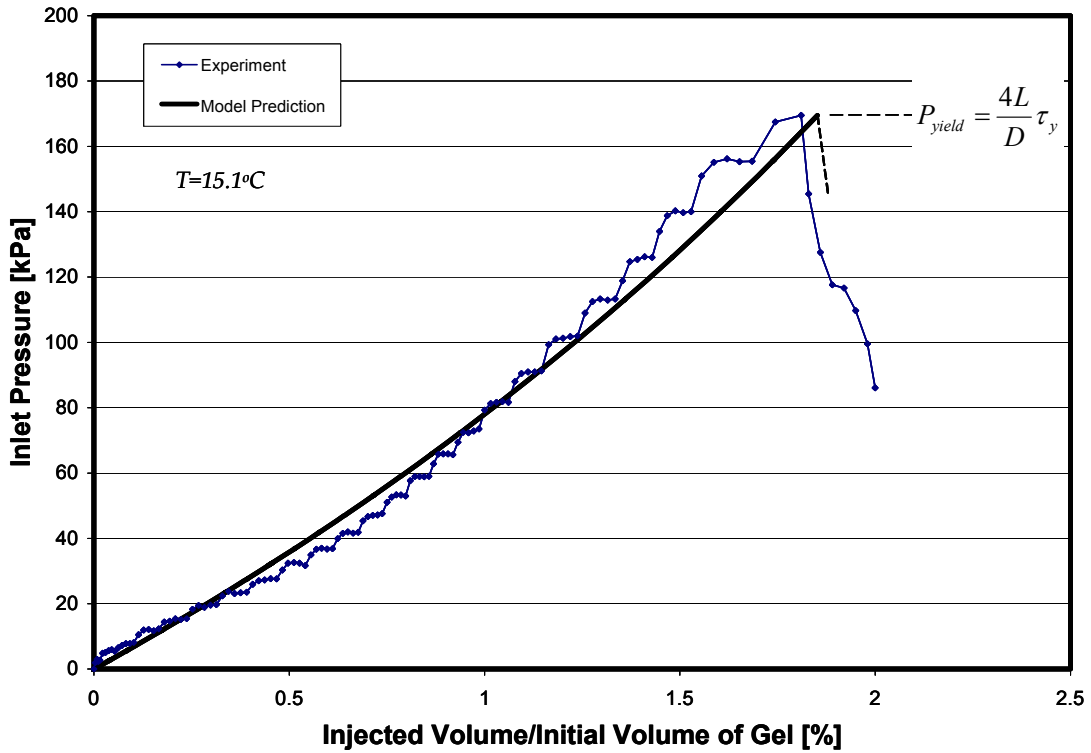


Figure 3.13: Compressed volume during the restart process for lab-scale pipeline.

Field Considerations

The merit of the model is to provide the pressure increase prediction as a function of injected volume of fluid or time for a given injection rate. Therefore with the present model we can design optimum pump specifications for minimizing down time. For example if a low flow rate pump were used for the initial compression, the gel breaking requires significant amount of time because of the low flow rate. However as illustrated in Figure 3.14, this time could be reduced by a low pressure and high flow rate pump for initial gel compression up to a time t using our ΔP as a function of ΔV prediction. After reaching to the limit of low pressure pump, the low pressure pump can be switched to a high pressure low flow rate pump for the rest of time to complete the gel breaking.

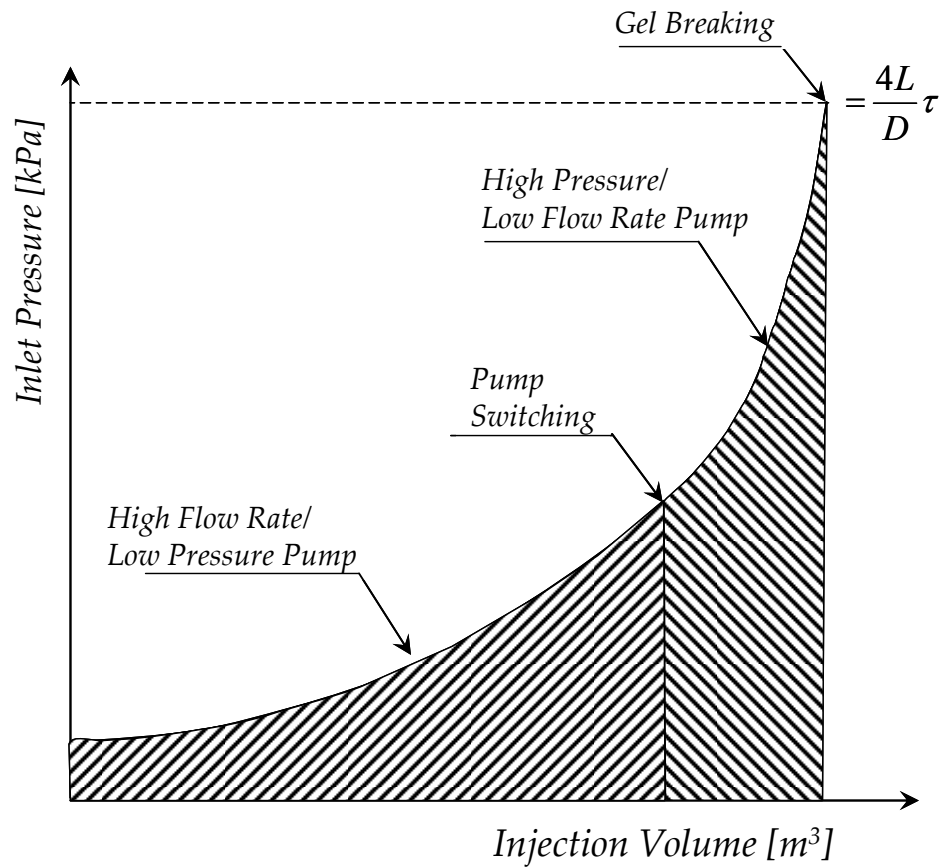


Figure 3.14: Strategy for the restart of a gelled pipeline.

Summary

In this research, we have investigated the gel breaking mechanism at various temperatures and cooling rates using a model pipeline, a controlled stress rheometer and a cross-polarized microscope. This study has revealed that the controlled stress rheometer and classical restart pressure drop equation (Equation (3.1)) can successfully predict the required gel breaking pressure of a gelled pipeline if the cooling rate is low and the gel breaking occurs at the pipe wall (adhesive failure). Furthermore, we have experimentally shown that there exists a delineation point between cohesive and adhesive failures when the measured gel strength is plotted as a function of cooling rate. Using the controlled stress rheometer experiments and the cross-polarized microscope, this study has also investigated the possible reasons why there exists a delineation point between cohesive and adhesive failures. Based on the results of model pipeline experiments and compressibility of the wax-oil system, a theoretical model has been developed that can explain the gel breaking process in pipelines. The gel breaking model incorporates the pressure propagation phenomenon and can predict the required time to break the gel. These results can be utilized to predict the restart time and the restart pressure in field pipelines.

Nomenclature

a	Parameter used in Equation (3.5) [-]
b	Parameter used in Equation (3.5) [kPa]
D	Pipe radius [m]
L	Pipe length [m]
$m_{deposit}$	Mass of the wax deposit [kg]
P	Pressure [kPa]
P_{in}	Inlet pressure [kPa]
P_0	Baseline pressure [kPa]
P_y	Yield pressure [kPa]
V_0	total volume of gel in the pipeline [m ³]
ζ	Location of the pressure front [m]
τ_y	Yield stress [kPa]
ΔV	Compressed volume due to the applied pressure [kPa]

References

- Borghì, G.-P., S. Corraera, M. Merlini, and C. Carniani, "Prediction and Scaleup of Waxy Oil Restart Behavior", 2003 SPE International Symposium on Oilfield Chemistry Houston, TX. (2003)
- Cawkwell, M.G. and M.E. Charles, "Characterization of Canadian Arctic Thixotropic Gelled Crude Oils Utilizing an Eight-Parameter Model", *J. Pipelines* **7**, 251-264 (1989)
- Cazaux, G., L. Barre, and F. Brucy, 1998 SPE Annual Technical Conference and Exhibition, New Orleans, 27 (1998).
- Chang, C., D.V. Boger, and Q.D. Nguyen, "Yielding of Waxy Crude Oils," *Ind. Eng. Chem. Res.* **37**, 1551 (1998)
- Chang, C., O.D. Nguyen, and H.P. Ronningsen, "Isothermal Start-up of Pipeline Transporting Waxy Crude Oil," *J. Non-Newt. Fluid Mech.* **87**, 127 (1999)
- Davenport, T.C. and R.S.H. Somper, "The Yield Value and Breakdown of Crude Oil Gels," *J. Inst. of Pet.* **55**, 86 (1971)
- Davidson, M.R., Q.D. Nguyen, C. Chang, and H.P. Rønningsen, "A Model for Restart of a Pipeline with Compressible Gelled Waxy Crude Oil," *J. Non-Newt. Fluid Mech.* **123**(2-3), 269 (2004)
- Dirand, M., V. Chevallier, E. Provost, M. Bouroukba, and D. Petitjean, "Multicomponent Paraffin Waxes and Petroleum Solid Deposits: Structural and Thermodynamic State," *Fuel* **77**(12), 1253 (1998)
- Fung, G., W.P. Backhaus, S. McDaniel, and M. Erdogmus, "To Pig or Not To Pig: The Marlin Experience with Stuck Pig", 2006 Offshore Technology Conference, Houston, TX (2006)
- Greiner, C., A. del Campo, and E. Arzt, "Adhesion of Bioinspired Micropatterned Surfaces: Effects of Pillar Radius, Aspect Ratio, and Preload," *Langmuir* **23**(7), 3495 (2007)
- Hayward, A.T., "Compressibility Equations for Liquids - a Comparative Study," *Brit. J. of Appl. Phys.* **18**(7), 965 (1967)
- Hénaut, I., O. Vincke, and F. Brucy, "Waxy Crude Oil Restart: Mechanical Properties of Gelled Oils," 1999 SPE Annual Technical Conference and Exhibition, Houston, TX (1999)

- Kane, M., M. Djabourov, J.L. Volle, J.P. Lechaire, and G. Frebourg, "Morphology of Paraffin Crystals in Waxy Crude Oils Cooled in Quiescent Conditions and under Flow," *Fuel* **82**(2), 127 (2003)
- Longhenry, J.L., B.J. Love, and N.S. Murthy, "Cooling Rate-induced Glass-adhesion Variations using Crystallizing Hot-melt Adhesives," *J. Mater. Sci.* **32**(9), 2283 (1997)
- Paso, K., M. Senra, Y.B. Yi, A.M. Sastry, and H.S. Fogler, "Paraffin Polydispersity Facilitates Mechanical Gelation," *Ind. Eng. Chem. Res.* **44**(18), 7242 (2005).
- Rønningsen, H.P., "Rheological Behaviour of Gelled, Waxy North Sea Crude Oils," *J. Pet. Sci. Eng.* **7**, 177 (1992)
- Singh, P., R. Venkatesan, H.S. Fogler, and N. Nagarajan, "Formation and Aging of Incipient Thin Film Wax-oil Gels," *AIChE J.* **46**(5), 1059 (2000)
- Thomason, W.H., "Start-Up and Shut-in Issues for Subsea Production of High Paraffinic Crudes," 2000 Offshore Technology Conference, Houston, TX (2000).
- Uhde, A., and G. Kopp, "Pipeline Problems Resulting from Handling of Waxy Crudes," *J. Inst. of Pet.* **57**(554), 63 (1971)
- Venkatesan, R., Ph.D. Thesis, University of Michigan (2003)
- Venkatesan, R., N.R. Nagarajan, K. Paso, Y.B. Yi, A.M. Sastry, and H.S. Fogler, "The Strength of Paraffin Gels Formed under Static and Flow Conditions," *Chem. Eng. Sci.* **60**(13), 3587 (2005)
- Venkatesan, R., J.A. Ostlund, H. Chawla, P. Wattana, M. Nyden, and H.S. Fogler, "The Effect of Asphaltenes on the Gelation of Waxy Oils," *Energy and Fuels* **17**(6), 1630 (2003)
- Venkatesan, R., P. Singh, and H.S. Fogler, "Delineating the Pour Point and Gelation Temperature of Waxy Crude Oils," *SPE J.* **7**(4), 349 (2002)
- Verschuur, E., A.P.D. Hartog, and C.M. Verheul, "Effect of Thermal Shrinkage and Compressibility on Yielding of Gelled Waxy Crude Oils in Pipelines," *J. Inst. of Pet.* **57**(554), 131 (1971)
- Vignati, E., R. Piazza, R.F.G. Visintin, R. Lapasin, P. D'Antona, and T.P. Lockhart, "Wax Crystallization and Aggregation in a Model Crude Oil," *J. of Phys.: Condens. Matter* **17**(45), 3651 (2005)

- Visintin, R.F.G., R. Lapasin, E. Vignati, P. D'Antona, and T.P. Lockhart, "Rheological Behavior and Structural Interpretation of Waxy Crude Oil Gels," *Langmuir* **21**(14), 6240 (2005)
- Wardhaugh, L.T. and D.V. Boger, "The Measurement and Description of the Yielding Behavior of Waxy Crude-Oil," *J. Rheol.* **35**(6), 1121 (1991)
- Zhu, H.G., Z.H. Liu, Y.L. Tian, Y. Xue, and L. Yin, "Molar Volume, Thermal Expansivity and Isothermal Compressibility of trans-Decahydronaphthalene up to 200MPa and 446K," *Chinese Physics* **14**(12), 2433 (2005)

CHAPTER IV

COMBINED CONVECTIVE HEAT AND MASS TRANSFER ANALYSIS OF WAX DEPOSITION UNDER TURBULENT FLOW CONDITIONS

Introduction

Highly waxy crude oil can cause significant problems during the production and transportation of crude oil as a result of the precipitation and deposition of wax (or paraffin) components that can block the pipeline (Singh et al., 2000). Crude oil is a mixture of paraffins, aromatics, naphthenes, asphaltenes and resins. Wax deposition occurs when the paraffin components in crude oil (alkanes of carbon number in the range of 20 to 70 or higher) precipitate and deposit on the cold pipeline wall. At reservoir temperatures (70 °C-150 °C) and pressures wax molecules are dissolved in the crude oil. However, as the crude oil flows through a sub-sea pipeline resting on the ocean floor which is at temperature of 4 °C, the temperature of oil decreases below its cloud point temperature (or wax appearance temperature, WAT) due to the heat loss to the surroundings. The solubility of wax decreases drastically as the temperature decreases and wax molecules starts to precipitate on the pipeline wall.

As the deposited wax layer grows in thickness within a crude oil pipeline, the flow of oil is impeded due to the flow restriction, as shown in Figure 4.1. In the worst cases, production must be stopped in order to replace the plugged portion of the pipeline. The cost of this replacement and downtime is estimated approximately \$30,000,000 per

incident (Venkatesan, 2003). In one case, the wax deposition was so severe and frequent that an off-shore platform in the North Sea had to be abandoned at a cost of about \$100,000,000 (Singh et al., 2000).



Figure 4.1: Wax deposit in a retrieved pipeline (Singh et al., 2000).

Because highly waxy crude oils represent a significant portion of the annual petroleum production, the remediation of wax deposits is a vital element of production assurance research (Lee et al., 2007). One of the most conventional mechanical methods used is pigging. In pigging, an iron of pig passes through the pipeline to scrape off the wax. However, if the wax deposit builds up fairly rapidly and hardens, the pig can become stuck as was the case in one of the Gulf of Mexico pipelines (Fung et al., 2006). A fused chemical reaction technique to use exothermic reaction with controlled heat emission has been proposed (Singh and Fogler, 1998; Nguyen et al., 2001, 2003, 2004; Nguyen and Fogler, 2005) to remove the wax deposit. However, in order to successfully use this technique as well as pipeline section replacement, it is crucial to know the thickness profile and the wax fraction of the deposit.

One of the most important factors in predicting wax deposition is calculating radial transportation of wax molecules in the boundary layer in order to determine the growth of wax deposit. A number of radial transportation mechanisms have been suggested including radial convective flux (Singh et al., 2000, 2001), molecular diffusion (Bern et al., 1980; Burger et al., 1981; Majeed et al., 1990; Brown et al., 1993; Svendsen, 1993; Ribeiro et al., 1997; Creek et al, 1999), and precipitated wax particle transportation (by shear dispersion, Brownian diffusion, and gravity settling (Todi, 2005)). Venkatesan and Fogler (2004) have reported the importance of the decrease of the radial mass flux under turbulent flow conditions where there is high shear at the interface between wax deposit and oil. Furthermore, in the turbulent flow regime, the wax deposited on the pipeline wall can be sloughed off due to the high shear at the oil-deposit interface. This phenomenon is considered as a random event and has not been mathematically modeled (Venkatesan, 2003).

Among these radial transportation mechanisms there is consensus that the convection and molecular diffusion in the laminar sub-layer are the major radial transportation mechanisms (Bern et al., 1980; Burger et al., 1981; Majeed et al., 1990; Brown et al., 1993; Svendsen, 1993; Ribeiro et al., 1997; Creek et al, 1999; Singh et al., 2000, 2001; Venkatesan and Fogler, 2004). It is notable that, except Singh et al. (2000, 2001), most of previous models calculated the radial wax flux with the assumption of thermodynamic equilibrium in the mass transfer boundary layer, i.e. the wax concentration follows the solubility, $C_{ws}(T(r))$ in the boundary layer.

$$\frac{dm_{deposit}}{dt} = (-2\pi r_i L) D_{wo} \frac{\partial C}{\partial r} = (-2\pi r_i L) D_{wo} \frac{dC_{ws}}{dT} \frac{\partial T}{\partial r} \quad (4.1)$$

where C is the wax concentration, T is the oil temperature, r is the radial coordinate, r_i is the effective radius of a pipe, $m_{deposit}$ is the mass of the wax deposit, D_{wo} is the molecular diffusivity of wax in oil, and L is the pipe length. However, this equilibrium assumption is not valid when the difference between the solubility and the wax concentration in the boundary layer is significant such that the precipitation kinetics of wax molecules in the boundary layer is slow (Paso et al., 2005). Many studies have assumed that wax fraction in the deposit is constant during the wax deposition process (Bern et al., 1980; Burger et al., 1981; Majeed et al., 1990; Brown et al., 1993; Svendsen, 1993; Ribeiro et al., 1997). However, the assumption has been proved to be invalid (Lund, 1998; Creek et al, 1999; Singh et al., 2000, 2001) both theoretically and experimentally. The wax deposit is a 3-D network structure of the wax crystals that contain a significant amount of oil inside of the crystal structure. Therefore wax molecules diffuse into the deposit at the deposit-fluid interface because of the radial concentration gradient. This increase of the wax fraction in the deposit with time is called “aging”. Generally, higher flow rates enhance aging and wax fractions in the deposit can be as high as 60-70% (Lund, 1998).

In order to overcome these limitations of previous models, Singh et al. (2000, 2001) developed a comprehensive mathematical model of wax deposition phenomenon that can predict both wax deposit thickness and wax aging phenomenon under laminar/low shear conditions. They calculated the mass flux using the convective mass transfer coefficient obtained from laminar Sherwood number correlations (Hausen, 1943; Seider and Tate, 1936). The formation process of wax deposit can be described by following steps as stated by Singh et al. (2000).

- (1) Gelation of the waxy oil (formation of incipient gel layer) on the cold surface
- (2) Diffusion of waxes (hydrocarbons with carbon numbers greater than the critical carbon number) towards the gel layer from the bulk
- (3) Internal diffusion of these molecules through the trapped oil
- (4) Precipitation of these molecules in the deposit
- (5) Counter diffusion of de-waxed oil (hydrocarbons with carbon numbers lower than the critical carbon number) out of the gel layer

Figure 4.2 shows the schematic of radial transportation of wax molecules suggested by Singh et al. (2000).

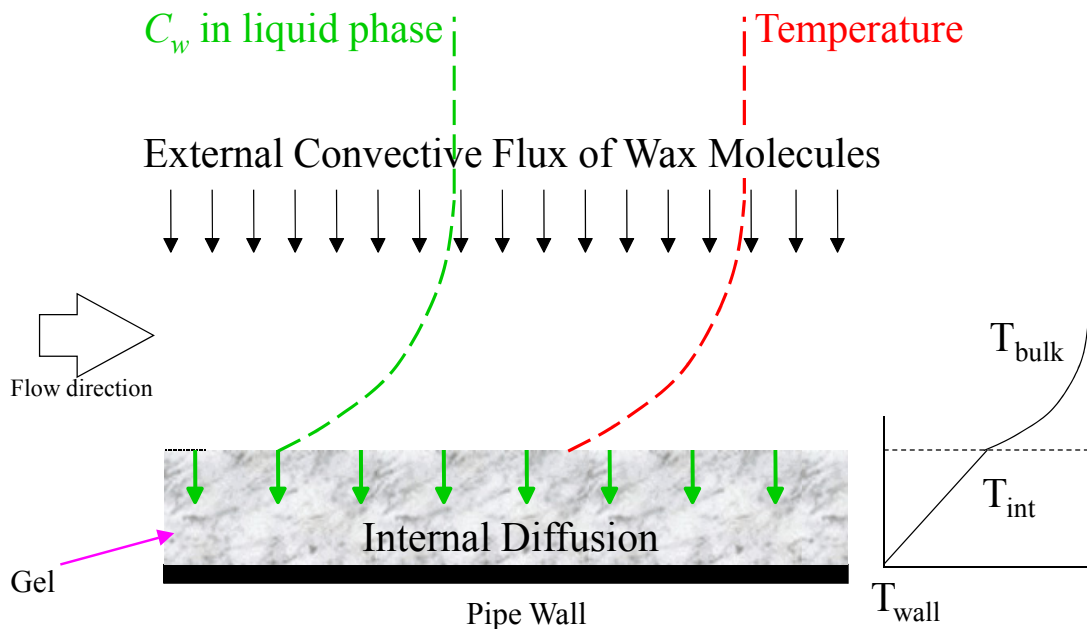


Figure 4.2: Schematic of convective heat and mass transfer suggested by Singh et al. (2000).

Under turbulent flow conditions and/or if wax is abundant in the boundary layer, the direct use of a heat and mass transfer analogy (e.g. the Chilton-Colburn analogy) to

calculate the convective mass flux in the Singh et al. (2000)'s wax deposition model results in overprediction of the wax deposit thickness and its fraction (Venkatesan and Fogler, 2004). This failure of the heat and mass transfer analogies in the wax deposition prediction is due to the fact that the analogies cannot be applied when heat and mass transfer occur simultaneously (Venkatesan and Fogler, 2004). In order to resolve this limitation, Venkatesan and Fogler (2004) proposed a method to estimate the convective mass transfer rate (i.e. the Sherwood number) using the Nusselt number and the solubility curve obtained experimentally. This solubility method, however, is based on the thermodynamic equilibrium in the mass transfer boundary layer, and as we discussed earlier, it implies that the mass transfer is fully dictated by heat transfer.

In this research, we have investigated the combined heat and mass transfer phenomenon under laminar and turbulent flow conditions using the FDM (finite difference method) technique in order to exploit Singh et al. (2000)'s wax deposition model without using either a heat and mass transfer analogy or the solubility method. In this paper, we will first show that the impact of precipitation of wax molecules on the convective mass flux in the boundary layer and that the improved wax deposition model is bounded by the solubility model (Venkatesan and Fogler, 2004) at the low end bound and the Chilton-Colburn analogy (Chilton and Colburn, 1934) at the high end. Secondly, by comparing the results of improved computational wax prediction model with both lab scale and with large scale turbulent wax deposition experiments, we show that the wax deposition model can successfully predict both the thickness and the aging of wax deposit under various turbulent conditions (Venkatesan, 2003; Lund 1998). Finally, we will provide a case study of improved wax deposition modeling for a field scale pipeline

system. This paper will describe the details of the combined heat and mass transfer analysis in the boundary layer, explain the simulation results under turbulent conditions, and show the comparison between experimental results for various scales of flow loop systems and theoretical predictions.

Theory - Wax deposition model

In this section, we will briefly review the limiting cases of our models which are the Chilton-Colburn analogy method and the solubility method. We then describe the computational heat and mass transfer analysis for both laminar and turbulent flow that includes precipitation in the boundary layer which falls between the two limiting cases. In each of these models the equations describing growth and aging of the gel layer that describes grow and aging of the gel is essentially the same for all models as only k_M is different for each of the models. We shall discuss this balance on the gel layer first.

Balance of the gel layer

The convective flux of wax molecules to the gel deposit-oil interface is responsible for both the aging and growth of wax deposit. The difference between convective flux to the surface of the gel layer and the internal diffusion away from the interface of gel layer gives the growth of the deposit. The wax deposition mechanism has been formulated using the following mass and energy balances (Singh et al., 2000).

(Growth rate)

$$(-2\pi r_i)\rho_{gel}\bar{F}_w \frac{dr_i}{dt} = (2\pi r_i)k_M(C_b - C_{ws}(T_i)) - (2\pi r_i)\left(-D_e \frac{dC_{ws}}{dr}\Big|_i\right) \quad (4.2)$$

(Aging)

$$\pi\rho_{gel}(R^2 - r_i^2)\frac{d\bar{F}_w}{dt} = -2\pi r_i\left(-D_e \frac{dC_{ws}}{dr}\Big|_i\right) \quad (4.3)$$

(Energy Balance)

$$2\pi r_i h_i [T_b - T_i] = \frac{2\pi k_e [T_i - T_w]}{\ln(R/r_i)} - 2\pi r_i k_M [C_b - C_{ws}(T_i)] \Delta H_f \quad (4.4)$$

where \bar{F}_w is the wax fraction in the deposit, R is the radius of a pipe, ρ_{gel} is the density of the wax deposit, k_M is the inner convective mass transfer coefficient, C_b is the bulk concentration of wax, h_i is the inner convective heat transfer coefficient, ΔH_f is the heat of solidification of wax and D_e is the effective diffusivity in the deposit as given by Aris (1985):

$$D_{eff} = \frac{D_{wo}}{1 + \frac{\alpha^2 F_w^2}{1 - F_w} + \frac{\alpha F_w}{\sigma} + \frac{4\alpha F_w}{\pi(1 - F_w)} \ln\left[\frac{\pi\alpha^2 F_w}{\sigma(1 - F_w)}\right]} \quad (4.5)$$

where α is the aspect ratio of the wax crystals in the deposit (width to thickness) and σ is the ratio between slit and the thickness of wax crystals. If we were to neglect third and fourth terms in the denominator, equation (4.5) is identical with the simpler form suggested by Cussler et al. (1986).

$$D_{eff} = \frac{D_{wo}}{1 + \frac{\alpha^2 F_w^2}{1 - F_w}} \quad (4.6)$$

The details of calculation of the effective diffusivity are given in Appendix A. By solving Eq. (4.2)–(4.4) numerically, the thickness of the wax-oil deposit, $(R - r_i(t))$, and the wax fraction, $\bar{F}_w(t)$ can be obtained. Figure 4.3 shows that the Singh et al. (2000)’s model predicts the wax deposit thickness and its fraction successfully.

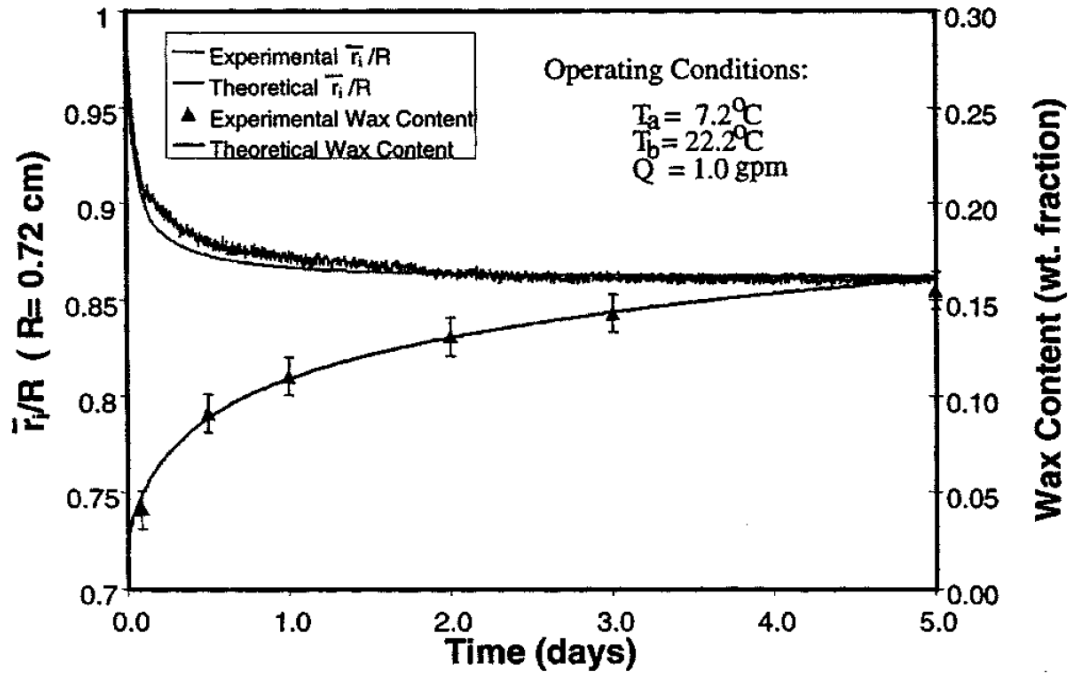


Figure 4.3: Theory vs. experiment for the wax deposition under a laminar flow condition (Singh et al., 2000).

Limiting Cases in Turbulent Flow Deposition

In order to solve Equations (4.2) - (4.4) to obtain the thickness of wax deposit and its fraction, the inner convective heat and mass transfer coefficient, h_i and k_M must first be calculated. Before we develop a rigorous computational method to calculate heat and mass transfer rate in the following sections, we introduce the two bounding conventional approaches- the Chilton-Colburn analogy (Chilton and Colburn, 1934) and solubility method (Venkatesan and Fogler, 2004) – in order to highlight the necessity of a rigorous

computational approach to calculate convective heat and mass transfer rate for wax deposition modeling.

Chilton-Colburn Method

The heat-mass transfer analogies such as the Chilton-Colburn analogy shown in Equations (4.7) and (4.8) are generally valid and are frequently used for many chemical engineering problems.

$$Nu = 0.023 Re^{0.8} Pr^{1/3} \quad (4.7)$$

$$Sh = 0.023 Re^{0.8} Sc^{1/3} \quad (4.8)$$

where Re is the Reynolds number ($Re \equiv Dv_{avg} / \nu$), Pr is the Prandtl number ($Pr \equiv \nu / \alpha_T$) and Sc is the Schmidt number ($Sc \equiv \nu / D_{wo}$). However the heat-mass transfer analogy is valid only when the temperature and concentration fields are independent. As shown in the wax concentration vs. temperature plot in Figure 4.4, the Chilton-Colburn analogy provides maximum supersaturation (indicated as shaded area) due to the independence of the temperature and concentration fields. In addition the Lewis number (Sc/Pr) is large, the order of 10^2 , which results in a much thinner mass transfer boundary layer than a thermal boundary layer. As a result, the wax concentration adjacent to the oil-deposit interface approaches to bulk wax concentration because the thickness of mass transfer boundary layer becomes very small as shown in Figure 4.5. In this approach, the wax concentration in the boundary layer is not affected by thermodynamics but is solely determined by the transport processes of radial diffusion and axial advection.

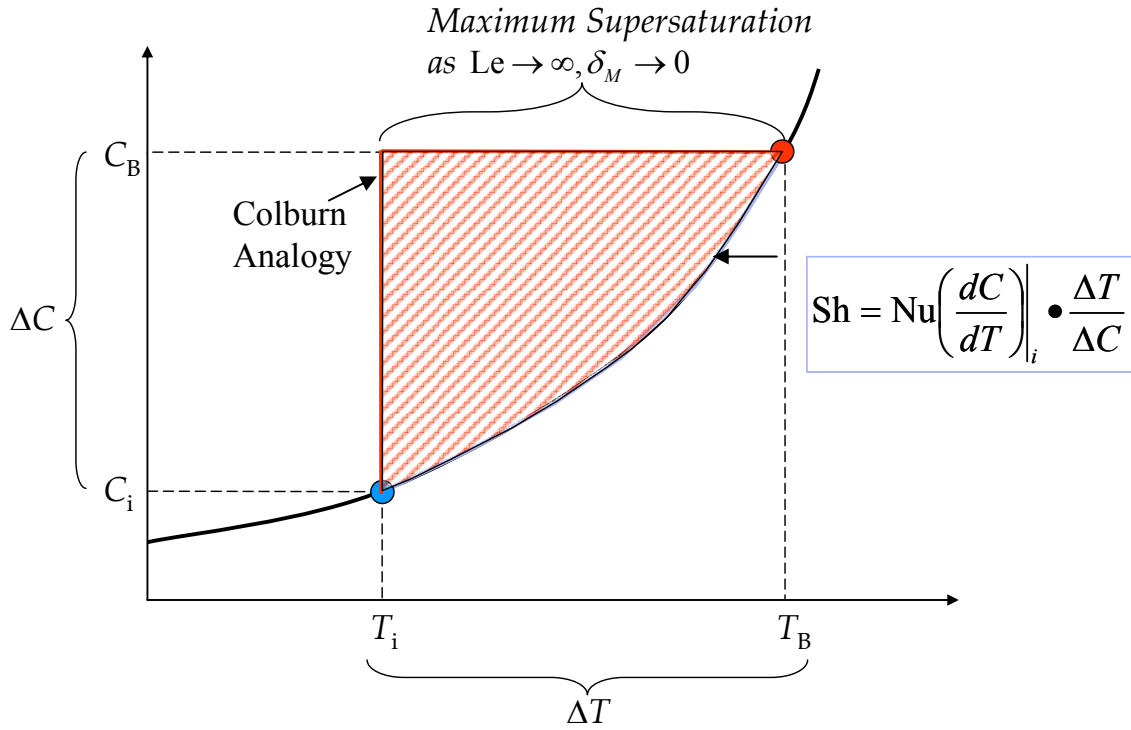


Figure 4.4: Comparison of the Chilton-Colburn analogy and the solubility method in the solubility as a function of temperature space.

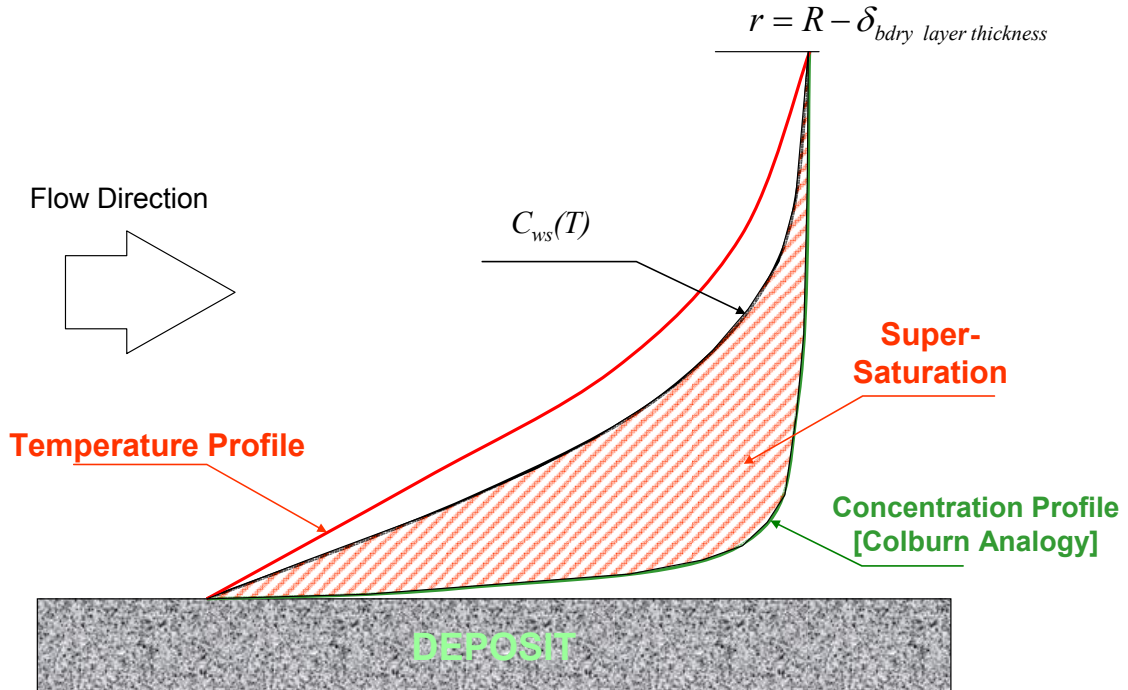


Figure 4.5: Heat and mass transfer boundary layer for turbulent waxy oil flow.

Solubility Method

Because heat and mass transfer occur simultaneously in the boundary layer, the wax concentration profile is strongly influenced by the temperature profile (Venkatesan and Fogler, 2004). When the temperature falls below the cloud point temperature, precipitation of wax molecules occurs in the thermal boundary layer. In order to take into account of this dependency, Venkatesan and Fogler (2004) proposed a solubility method to calculate convective mass transfer rate when there is a dependency between heat and mass transfer.

$$Sh_{solubility} = Nu \left(\frac{dC}{dT} \right) \Big|_i \cdot \frac{\Delta T}{\Delta C} \quad (4.9)$$

The solubility method used to calculate the convective mass flux (i.e. the Sherwood number) assumes that the concentration profile in the mass transfer boundary layer follows the thermodynamic equilibrium limit between temperature and concentration at every point. In the solubility method, the convective mass flux fully depends on the temperature profile and solubility of wax as a function of temperature as shown in Figures 4.4 and 4.5. At any time t , the Sherwood number can be calculated using the tangent of the solubility curve at the interface temperature multiplied by $\Delta T / \Delta C$. The actual concentration profile exists between the concentration profiles of the Chilton-Colburn analogy and the solubility method and depends on the precipitation kinetics as illustrated in the shaded area in Figures 4.4 and 4.5. In the following section, we introduce the details of the calculation approach to calculate the combined heat and mass transfer rigorously.

Computational heat and mass transfer approach in the laminar flow regime

Instead of using the limiting cases of the heat and mass transfer analogy method and the solubility method (Venkatesan and Fogler, 2004) to calculate the Nusselt number and the Sherwood number, a new computational approach is used.

$$Nu = \frac{(-2r_i) \frac{\partial T}{\partial r} \Big|_{r=r_i}}{T_b - T_i} = \frac{(2r_i)h_i}{k} \quad (4.10)$$

$$Sh = \frac{(-2r_i) \frac{\partial C}{\partial r} \Big|_{r=r_i}}{C_b - C_i} = \frac{(2r_i)k_M}{D_{wo}} \quad (4.11)$$

In order to obtain the temperature and concentration gradients at the fluid-deposit interface as given in Equations (4.10) and (4.11), we solve the mass balance and energy balance equations (Equations (4.12) and (4.13)).

(Mass Transfer)

$$v_z \frac{\partial C}{\partial z} = \frac{1}{r} \frac{\partial}{\partial r} \left[r D_{wo} \frac{\partial C}{\partial r} \right] - k_r (C - C_{ws}) \quad (4.12)$$

(Heat Transfer)

$$v_z \frac{\partial T}{\partial z} = \frac{1}{r} \frac{\partial}{\partial r} \left[r \alpha_T \frac{\partial T}{\partial r} \right] - \beta (C - C_{ws}) \quad (4.13)$$

,where v_z is the axial velocity which has the parabolic velocity profile for the oil phase

for a laminar flow. $v_z = 2v_{avg} \left[1 - \left(\frac{r}{r_i} \right)^2 \right]$ if $r < r_i$ and $v_z = 0$ if $r_i < r < R$,

$$\alpha_T \equiv \frac{k}{\rho C_p}, \text{ and } \beta \equiv \frac{k_r \Delta H_f}{\rho C_p}$$

Note that the precipitation term $\beta(C - C_{ws})$ in the energy balance equation (4.13) can be neglected because the precipitation term is insignificant (less than 0.1%) compared to the advection and diffusion terms. The corresponding boundary conditions are given as follows.

$$\left\{ \begin{array}{ll} C = C_b & \text{at } z = 0 \\ \frac{\partial C}{\partial r} = 0 & \text{at } r = 0 \\ C = C_{ws}(T_i) & \text{at } r = r_i \\ C = C_{wall} = C_{ws}(T_{wall}) & \text{at } r = R \end{array} \right. , \quad (4.14a)$$

$$\left\{ \begin{array}{ll} T = T_b & \text{at } z = 0 \\ \frac{\partial T}{\partial r} = 0 & \text{at } r = 0 \\ T = T_{wall} & \text{at } r = R \end{array} \right. \quad (4.14b)$$

Note that the wax concentration at the oil-deposit interface is in thermodynamic equilibrium and the interface temperature and the effective radius change as time progresses. The interface temperature increases due to the thermal resistance of the wax deposit. Equation (4.15) is the discretized form of the mass transfer equation (Oosthuizen and Naylor, 1999).

$$A_j^c C_{ij} + B_j^c C_{ij+1} + C_j^c C_{ij-1} = D_j^c \quad (4.15)$$

$$A_j^c = \frac{v_{z,j}}{\Delta z_i} + \frac{1}{r_j} \frac{2}{\Delta r_{j+1} + \Delta r_j} \left\{ \left[\frac{r_{j+1} D_{wo,j+1} + r_j D_{wo,j}}{2} \right] \left(\frac{1}{\Delta r_{j+1}} \right) + \left[\frac{r_j D_{wo,j} + r_{j-1} D_{wo,j-1}}{2} \right] \left(\frac{1}{\Delta r_j} \right) \right\} + k_r \quad (4.15a)$$

$$B_j^c = -\frac{1}{r_j} \frac{2}{\Delta r_{j+1} + \Delta r_j} \left\{ \left[\frac{r_{j+1} D_{wo,j+1} + r_j D_{wo,j}}{2} \right] \left(\frac{1}{\Delta r_{j+1}} \right) \right\} \quad (4.15b)$$

$$C_j^c = -\frac{1}{r_j} \frac{2}{\Delta r_{j+1} + \Delta r_j} \left\{ \left[\frac{r_j D_{wo,j} + r_{j-1} D_{wo,j-1}}{2} \right] \left(\frac{1}{\Delta r_j} \right) \right\} \quad (4.15c)$$

$$D_j^c = \frac{v_{z,j} C_{i-1,j}}{\Delta z_i} + k_r C_{ws}(T_{ij}) \quad (4.15d)$$

If we re-write the governing equation and the corresponding boundary conditions in matrix form,

$$\begin{bmatrix} 1 & -1 & 0 & 0 & 0 & \dots & 0 & 0 & 0 & 0 \\ C_2^c & A_2^c & B_2^c & 0 & 0 & \dots & 0 & 0 & 0 & 0 \\ 0 & C_3^c & A_3^c & B_3^c & 0 & \dots & 0 & 0 & 0 & 0 \\ 0 & 0 & C_4^c & A_4^c & B_4^c & \dots & 0 & 0 & 0 & 0 \\ \vdots & \vdots & \vdots & \vdots & \vdots & \ddots & \vdots & \vdots & \vdots & \vdots \\ 0 & 0 & 0 & 0 & 0 & \dots & C_{NFLUID-1}^c & A_{NFLUID-1}^c & B_{NFLUID-1}^c & 0 \\ 0 & 0 & 0 & 0 & 0 & \dots & 0 & 0 & 1 & 0 \end{bmatrix} \begin{bmatrix} C_{i1} \\ C_{i2} \\ C_{i3} \\ C_{i4} \\ \vdots \\ C_{iNFLUID-1} \\ C_{iNFLUID} \end{bmatrix} = \begin{bmatrix} 0 \\ D_2^c \\ D_3^c \\ D_4^c \\ \vdots \\ D_{NFLUID-1}^c \\ C_{ws}(T_i) \end{bmatrix} \quad (4.16)$$

where NFLUID is the nodal point of the deposit-oil interface. The concentration profile from NFLUID to N (i.e. NFLUID < j < N) is determined solely by the solubility and temperature profiles in the deposit.

We can build the matrix equation for the heat transfer calculation in a similar manner.

$$A_j^T T_{ij} + B_j^T T_{ij+1} + C_j^T T_{ij-1} = D_j^T \quad (4.17)$$

$$A_j^T = \frac{v_{z,j}}{\Delta z_j} + \frac{1}{r_j} \frac{2}{\Delta r_{j+1} + \Delta r_j} \left\{ \left[\frac{r_{j+1} \alpha_{T,j+1} + r_j \alpha_{T,j}}{2} \right] \left(\frac{1}{\Delta r_{j+1}} \right) + \left[\frac{r_j \alpha_{T,j} + r_{j-1} \alpha_{T,j-1}}{2} \right] \left(\frac{1}{\Delta r_j} \right) \right\} \quad (4.17a)$$

$$B_j^T = -\frac{1}{r_j} \frac{2}{\Delta r_{j+1} + \Delta r_j} \left\{ \left[\frac{r_{j+1} \alpha_{T,j+1} + r_j \alpha_{T,j}}{2} \right] \left(\frac{1}{\Delta r_{j+1}} \right) \right\} \quad (4.17b)$$

$$C_j^T = -\frac{1}{r_j} \frac{2}{\Delta r_{j+1} + \Delta r_j} \left\{ \left[\frac{r_j \alpha_{T,j} + r_{j-1} \alpha_{T,j-1}}{2} \right] \left(\frac{1}{\Delta r_j} \right) \right\} \quad (4.17c)$$

$$D_j^T = \frac{v_{z,j} T_{i-1,j}}{\Delta z_j} \quad (4.17d)$$

$$\begin{bmatrix} 1 & -1 & 0 & 0 & 0 & \dots & 0 & 0 & 0 \\ C_2^T & A_2^T & B_2^T & 0 & 0 & \dots & 0 & 0 & 0 \\ 0 & C_3^T & A_3^T & B_3^T & 0 & \dots & 0 & 0 & 0 \\ 0 & 0 & C_4^T & A_4^T & B_4^T & \dots & 0 & 0 & 0 \\ \vdots & \vdots & \vdots & \vdots & \vdots & \ddots & \vdots & \vdots & \vdots \\ 0 & 0 & 0 & 0 & 0 & \dots & C_{N-1}^T & A_{N-1}^T & B_{N-1}^T \\ 0 & 0 & 0 & 0 & 0 & \dots & 0 & 0 & 1 \end{bmatrix} \begin{bmatrix} T_{i1} \\ T_{i2} \\ T_{i3} \\ T_{i4} \\ \vdots \\ T_{iN-1} \\ T_{iN} \end{bmatrix} = \begin{bmatrix} 0 \\ D_2^T \\ D_3^T \\ D_4^T \\ \vdots \\ D_{N-1}^T \\ T_{wall} \end{bmatrix} \quad (4.18)$$

By inverting the matrices (Equations (4.16) and (4.18)), we obtain the radial temperature and concentration profiles, and by numerically marching from the inlet of the tube to the exit we can obtain the complete set of temperature and concentration profile with respect to r and z .

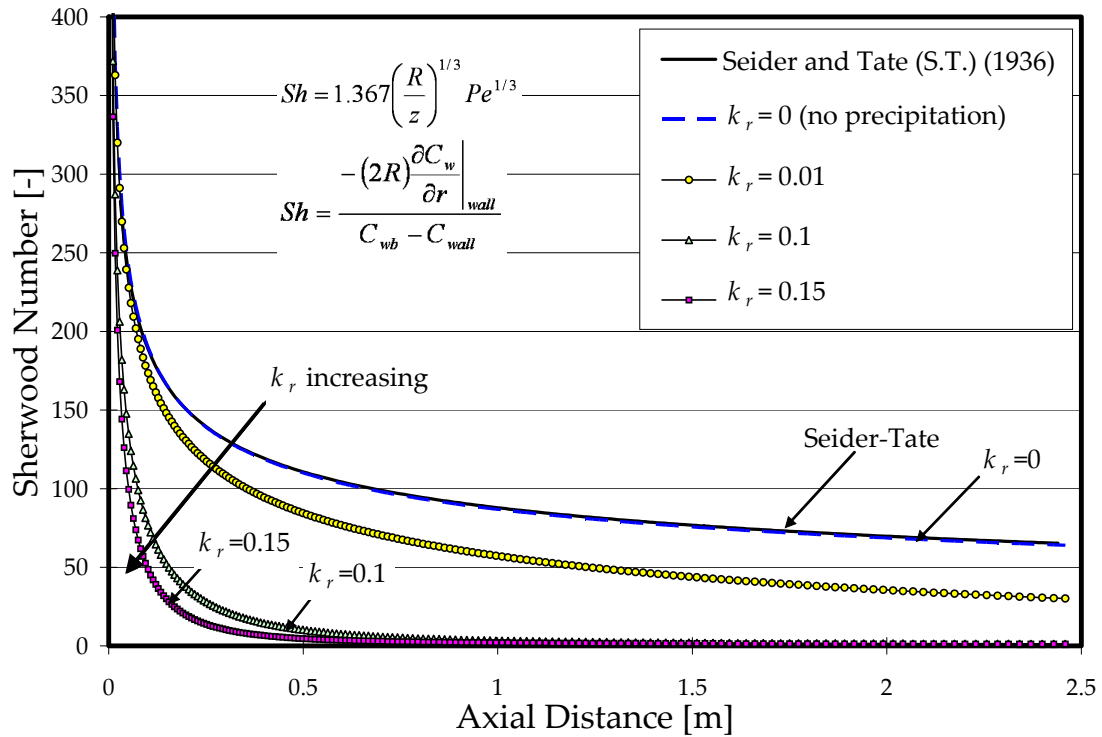


Figure 4.6: Sherwood number profile as a function of axial distance.

Figure 4.6 shows the Sherwood number as a function of the axial distance for various precipitation rate constants for laminar flow. If there is no precipitation in the boundary layer ($k_r = 0$) resulting in the fluid being supersaturation curve, then the heat and mass transfer rates becomes independent each other. As a result, the laminar convective mass transfer rate calculated by the Finite Difference Method developed in this study agrees well with the Seider-Tate correlation (i.e., independent mass transfer correlation). As k_r increases, the precipitation rate increases and, as a result, wax molecules do not reach the oil-deposit interface but instead flow down to exit as solid particles.

Heat and mass transfer under turbulent flow regime

In order to obtain the Sherwood number and the Nusselt number under turbulent conditions, we must solve the heat and mass transfer equations in a manner similar to that for laminar flow. The governing equations (4.12) and (4.13) for laminar flow must be modified for turbulent flow to include the turbulent axial velocity profile and the thermal and mass transfer eddy diffusivities.

$$\textbf{(Mass Transfer)} \quad v_z \frac{\partial C}{\partial z} = \frac{1}{r} \frac{\partial}{\partial r} \left[r(\varepsilon_M + D_{wo}) \frac{\partial C}{\partial r} \right] - k_r (C - C_{ws}) \quad (4.19)$$

$$\textbf{(Heat Transfer)} \quad v_z \frac{\partial T}{\partial z} = \frac{1}{r} \frac{\partial}{\partial r} \left[r(\varepsilon_H + \alpha_T) \frac{\partial T}{\partial r} \right] \quad (4.20)$$

,where $\frac{\varepsilon_M}{D_{wo}} \equiv \frac{Sc}{Sc_T} \frac{\varepsilon}{\nu}$, $\frac{\varepsilon_H}{\alpha_T} \equiv \frac{Pr}{Pr_T} \frac{\varepsilon}{\nu}$, $Sc_T = 0.85 + \frac{0.015}{Sc}$, $Pr_T = 0.85 + \frac{0.015}{Pr}$, and

$v_z = v_z^+ \sqrt{\frac{\tau_w}{\rho}}$ in the oil phase and $v_z = 0$ in the deposit. The momentum eddy

diffusivity, ε/ν , can be obtained as a function of dimensionless distance from the

deposit-oil interface, y^+ (Van Driest, 1956) and also the dimensionless turbulent velocity, v_z^+ is obtained from the Nikuradse equation (Deen, 1998),

$$\frac{\varepsilon}{\nu} = (\kappa y^+)^2 \left[1 - \exp\left(-\frac{y^+}{A}\right) \right]^2 \left| \frac{dv_z^+}{dy^+} \right| \quad (4.21a)$$

$$v_z^+ = \begin{cases} y^+ & y^+ \leq 5 \\ 5 \ln y^+ - 3.05 & 5 < y^+ \leq 30 \\ 2.5 \ln y^+ + 5.5 & y^+ \geq 30 \end{cases} \quad (4.21b)$$

where $y^+ = \frac{y}{\nu} \sqrt{\frac{\tau_w}{\rho}} = \left(1 - \frac{r}{R}\right) \frac{Re}{2} \sqrt{\frac{f}{8}}$, $f = \frac{0.305}{Re^{0.25}}$, $\kappa = 0.4$ and $A = 26$ (Deen, 1998).

The boundary conditions for the governing equations are identical with that of laminar case as given in Equation (4.14). After solving equations (4.19) and (4.20) numerically we obtain the radial and axial temperature and concentration profiles.

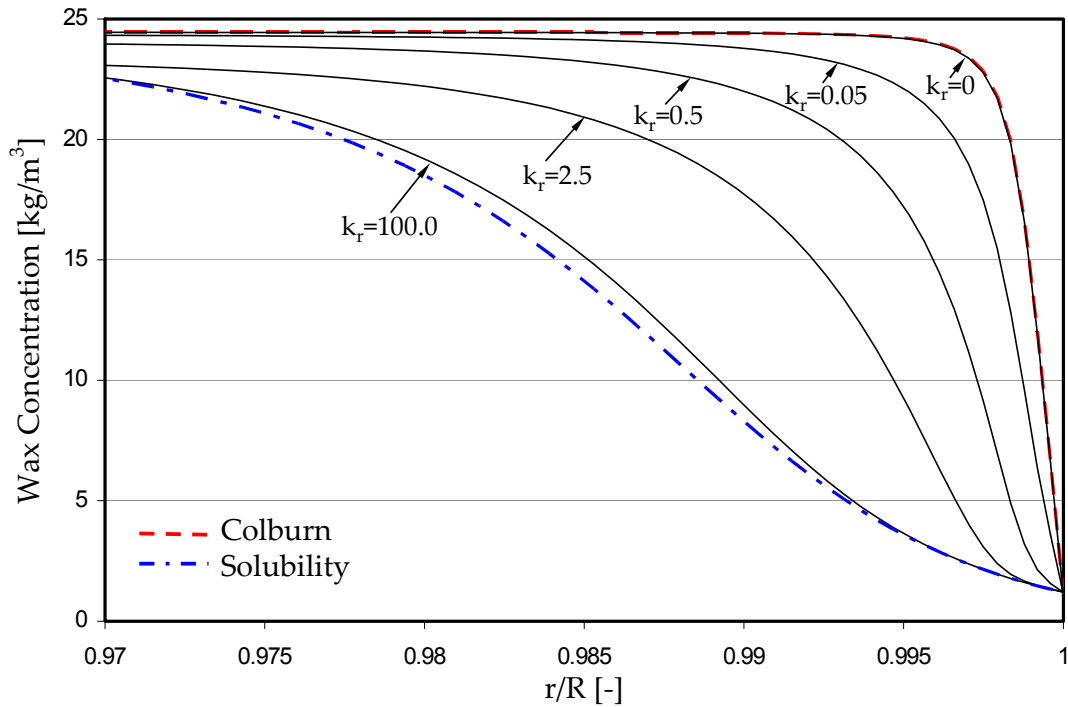


Figure 4.7: Wax concentration profile in the turbulent boundary layer (Re=7350).

Effect of wax precipitation in the turbulent boundary layer

The effect of wax precipitation in the boundary layer was studied by solving the governing equations for the wax concentration profile with various precipitation rate constants. As shown in Figure 4.7, as the precipitation rate constant k_p approaches zero the wax molecules do not precipitate in the boundary layer and the heat and mass transfer equations become independent. As k_p increases precipitation in the boundary layer increases and as a result both the wax concentration and its gradient decrease. If k_p increases further, the wax concentration approaches to the thermodynamic equilibrium, $C_{ws}(T(r, z))$, which is the solubility limit of wax molecules at a given temperature. We can calculate convective heat and mass transfer rates directly from Equation (4.9) using the wax concentration, $C(r, z)$, and the temperature $T(r, z)$ profiles. Figure 4.8 shows the ratio of the Sherwood number to the Nusselt number as a function of the precipitation rate constant.

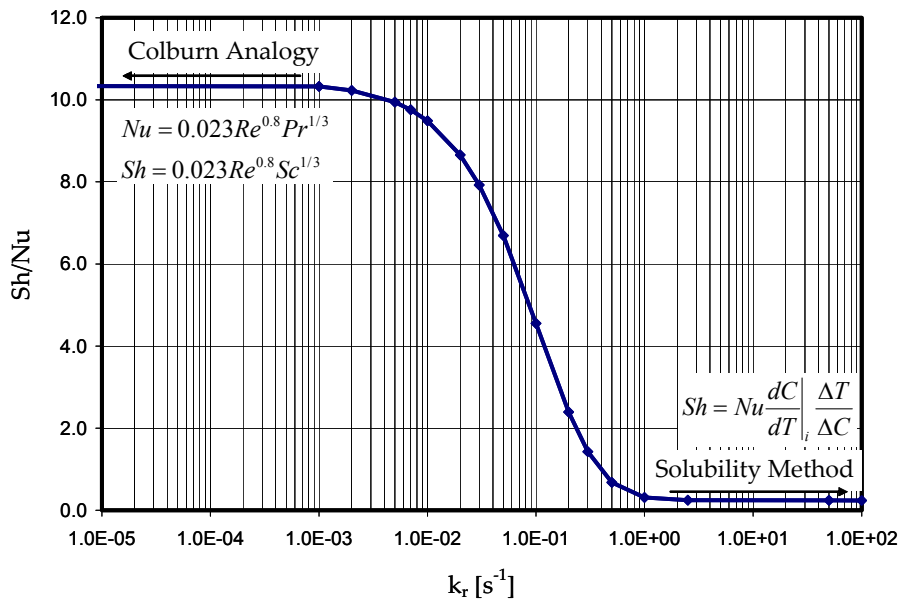


Figure 4.8: The ratio of Sherwood Number to Nusselt number as a function of precipitation rate constant (Re=7350).

We see the Sh/Nu ratio is identical with that of the Chilton-Colburn analogy when the precipitation rate constant is low (less than 10^{-3} s^{-1}), and the Sh/Nu ratio approaches to the solubility method when the precipitation rate constant is greater than 2.0 s^{-1} . Figure 4.8 clearly shows that the convective mass transfer rate can vary depending on the amount of precipitation. Further, the convective mass transfer rate can be bounded by the Chilton-Colburn analogy, as the upper bound, and bounded by the solubility method as the lower bound.

Discussion on the precipitation rate constant

The precipitation rate constant k_r (or equivalently the growth rate of wax nucleus in supersaturated solution) is zero if the temperature is greater than the wax appearance temperature. If the temperature is lower than the wax appearance temperature, we can estimate the growth rate of particles when diffusion is the rate determining step as (Marchisio et al., 2002),

$$G = \underbrace{k_d A_p \rho_n}_{k_r} (C - C_{ws}(T_i)), \quad (4.22)$$

where k_d is the mass transfer coefficient from bulk to the individual nucleus surface, A_p is the surface area of a nucleus and ρ_n is the number density of wax nuclei. The mass transfer coefficient k_d can be calculated from the following equations (Fogler (2005), Armenante and Kirwan (1989) and Marchisio et al., (2002)),

$$Sh_p = 2 + 0.6 Re_p^{0.5} Sc_p^{1/3} \cong 2 \quad (4.23)$$

$$k_d = \frac{Sh_p D_{wo}}{d_p} \quad (4.24)$$

The critical nucleus size is obtained as $0.0123 \mu\text{m}$ for Venkatesan (2003)'s turbulent flow cases from the critical nucleation theory provided in Appendix C and, due to the very small nucleus size, the particle Sherwood number is found to be close to 2 as shown in Equation (4.23). The details of the calculation of the critical radius and the range of the number density, growth rate constant, k_r , and its temperature dependency are given in Appendices B, C and D.

Computational model (Finite Difference Method combined with the wax prediction model by Singh et al., 2000)

The following algorithm is used for wax deposition model with the precipitation kinetics described in the previous section.

- [1] Generate computational grids with given deposit thickness as a function of axial distance at a given time t .
- [2] Solve Equations (4.12)-(4.13) for laminar flow, or Equations (4.19)-(4.20) for turbulent flow to get axial temperature and concentration profiles.
- [3] Calculate the Sherwood number using Equation (4.11) and concentration profile obtained in [2].
- [4] Integrate equations (4.2) and (4.3) to get new deposit thickness ($\delta(t + \Delta t)$) and wax fraction ($\bar{F}_w(t + \Delta t)$).
- [5] Repeat [1]-[4] until time reaches the final time.

Note that, in this computational model, we obtain the temperature profile numerically using equation (4.12) and, therefore, the energy balance equation given in the governing equation (4.3) is not required.

Results and Discussion

Before we substantiate the usefulness of the computational wax deposition model in field scale pipelines, we first need to verify the accuracy of the theoretical model in the laminar lab-scale experiment (Singh et al., 2000), the turbulent lab-scale experiments (Venkatesan, 2003), and then turbulent large scale flow loop experiments (Lund, 1998). After this verification, we will apply the computational wax deposition model to make prediction in a field scale pipeline ($D=0.3\text{m}$, $L=60\text{km}$).

Lab-scale laminar flow loop result

A lab-scale flow loop experimental result (Singh et al., 2000) is elected to be compared with the improved wax deposition model with the precipitation kinetics. A model wax-oil system (3:1 mixture of mineral oil (Blandol) and Kerosene and 0.67 wt.% of food grade wax with carbon numbers $C_{23}\text{-}C_{38}$) was used for the lab-scale ($ID = 1.44\text{ cm}$, Length = 2.44 m) flow loop experiments. The cloud point temperature of the sample was $13.9\text{ }^\circ\text{C}$, the inlet temperature was $22.2\text{ }^\circ\text{C}$ and wall temperature was $7.2\text{ }^\circ\text{C}$.

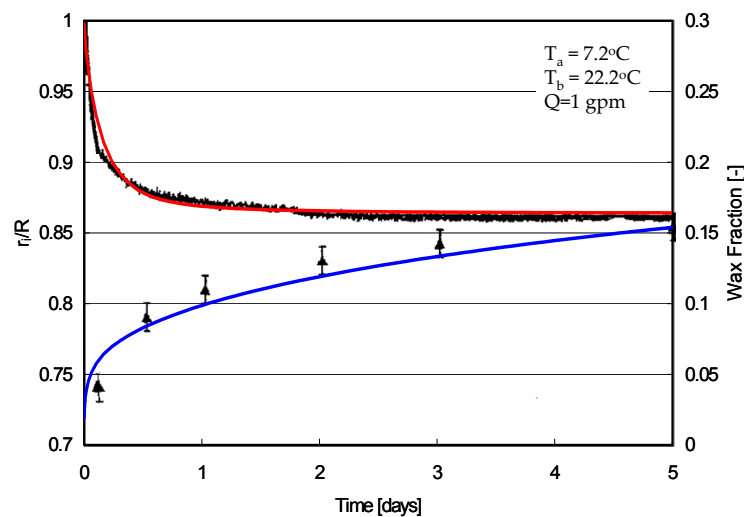


Figure 4.9: Comparison between theory and experiment for the wax deposition under a flow rate of 1 gpm and wall temperature of $7.2\text{ }^\circ\text{C}$ ($Re=535$).

Figure 4.9 compares the effective radius and wax fraction obtained by using the computational wax deposition model with the flow loop experiments by Singh et al. (2000). One can see there is excellent agreement between the theoretical prediction and the flow loop experiment of both the effective radius as well as the wax fraction. The precipitation rate constant k_r at the cloud point temperature in this case was obtained as 0.006 s^{-1} from equations (4.22)-(4.24), which indicates that the degree of supersaturation in this laminar boundary layer is high. In other words, very few of the wax molecules are precipitating in the boundary layer (see Figure 4.5). This high supersaturation in the boundary layer explains the success of Singh et al. (2000)'s wax deposition model which used the independent heat and mass transfer analogies (i.e. Hausen and Seider-Tate correlations) in their model.

Lab-scale turbulent flow loop results

In this section, lab-scale turbulent flow loop experimental results (Venkatesan, 2003) are compared with the computational wax deposition model with the precipitation kinetics. A model wax-oil system (50:50 mixtures of kerosene and a mineral oil (Blandol) and a wax with carbon numbers C_{21} - C_{41}) was used for lab-scale flow loop experiments. The cloud point temperature of the sample was $23.1 \text{ }^\circ\text{C}$, the inlet temperature was $25.6 \text{ }^\circ\text{C}$ and wall temperature was $4.4 \text{ }^\circ\text{C}$. The test section of the flow loop is 2.4 meter long and the inner diameter of the tube is 2.225 cm. The details of the experiments are given in Venkatesan (2003).

Figure 4.10 shows the temporal variation of effective radius due to the growth of wax deposit and its fraction. One observes that the wax deposit grows rapidly initially

due to the large thermal driving force at the beginning of the experiments and then reaches a plateau after about one day. The growth of wax deposit stops when the oil-deposit interface temperature reaches the cloud point temperature at which the convective flux in Equation (4.2) becomes almost negligibly small. One observes in Figure 4.10 that the wax deposition model with precipitation kinetics predicts the wax deposit thickness and its wax fraction successfully. In these calculations, the precipitation rate constant k_p at the cloud point temperature is 0.754 s^{-1} and the local mass transfer coefficient k_d (equation (4.24)) is 0.0017 m/s . The number density and the critical radius used in this prediction are given in Appendices B, C and D is also compared with theoretically maximum value and microscopic observation.

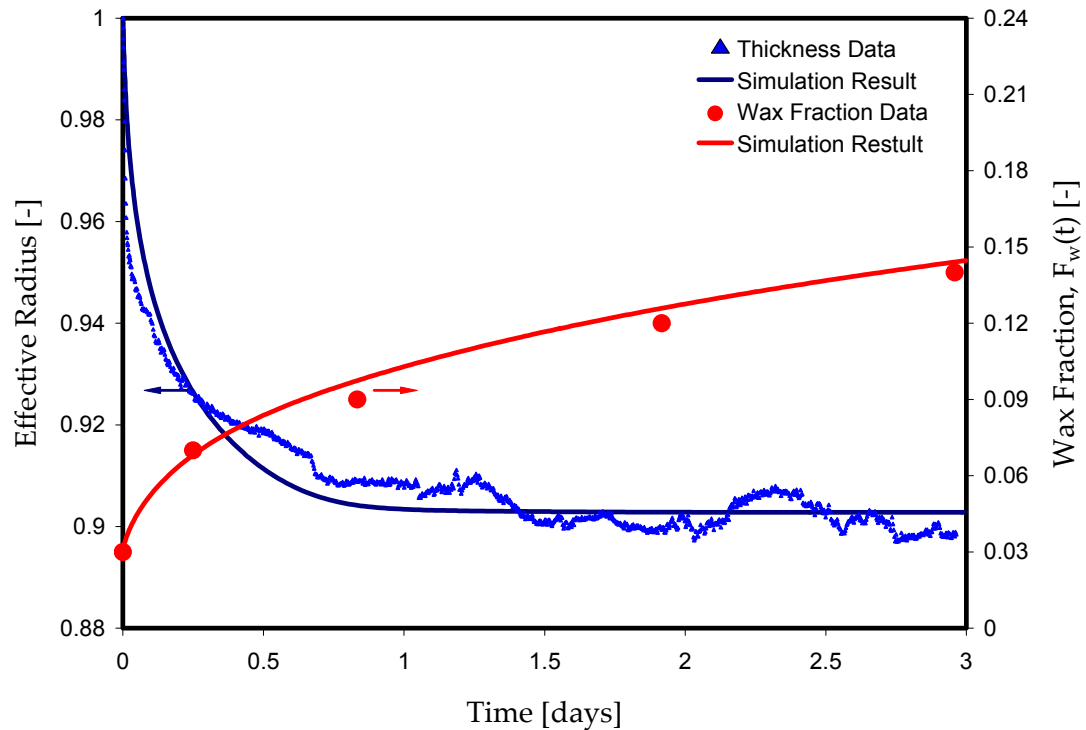


Figure 4.10: Wax deposit growth and aging under turbulent flow conditions ($Re=7350$).

Figure 4.11 compares the computational wax deposition prediction developed in this research with previous mass transfer rate calculation methods such as the Chilton-Colburn analogy and the solubility method (Venkatesan and Fogler, 2004). The Chilton-Colburn analogy overpredicts the growth rate at the beginning of the deposition whereas the solubility method underpredicts the deposit thickness. Both the Chilton-Colburn analogy and the solubility method give the same final thickness because the final thickness is solely determined by the energy balance and the growth of deposit stops when the oil-deposit interface temperature reaches the cloud point temperature (Singh et al., 2000). This discrepancy between the Chilton-Colburn analogy and Solubility method may not be significant in the lab scale flow loop situations where the thermal driving force is extremely large in order to minimize the experimental running time. However in field situations where there pipe dimensions are larger and there is insulation on the pipelines, the discrepancy shown in Figure 4.11 can give a significant overprediction if the wax model is based on the Chilton-Colburn analogy or underprediction if wax model is based on the solubility method.

The oil flow rate strongly affects wax deposition phenomena (Singh et al. 2000; Venkatesan, 2003). As the flow rate increases the boundary layer thickness is reduced and as a result the interface temperature reaches the cloud point temperature more rapidly resulting in a thinner deposit. Figure 4.12 shows the deposit thickness for flow rates of 10 gpm, 15 gpm, and 20 gpm. One notes that sloughing can occur at higher flow rates (especially $Q=15\text{gpm}$).

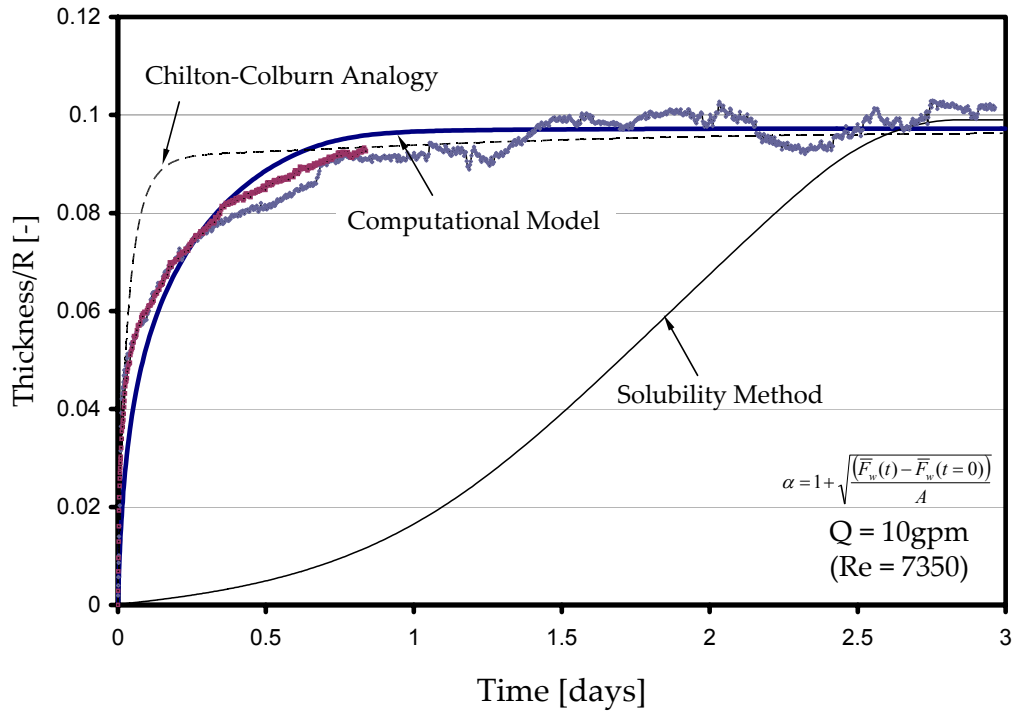


Figure 4.11: Comparison between the Chilton-Colburn analogy, Solubility method and computational model with precipitation kinetics (Re=7350) $A = \frac{\bar{F}_w(t_{final}) - \bar{F}_w(t=0)}{(\alpha_{final} - 1)^2} = 0.0045$.

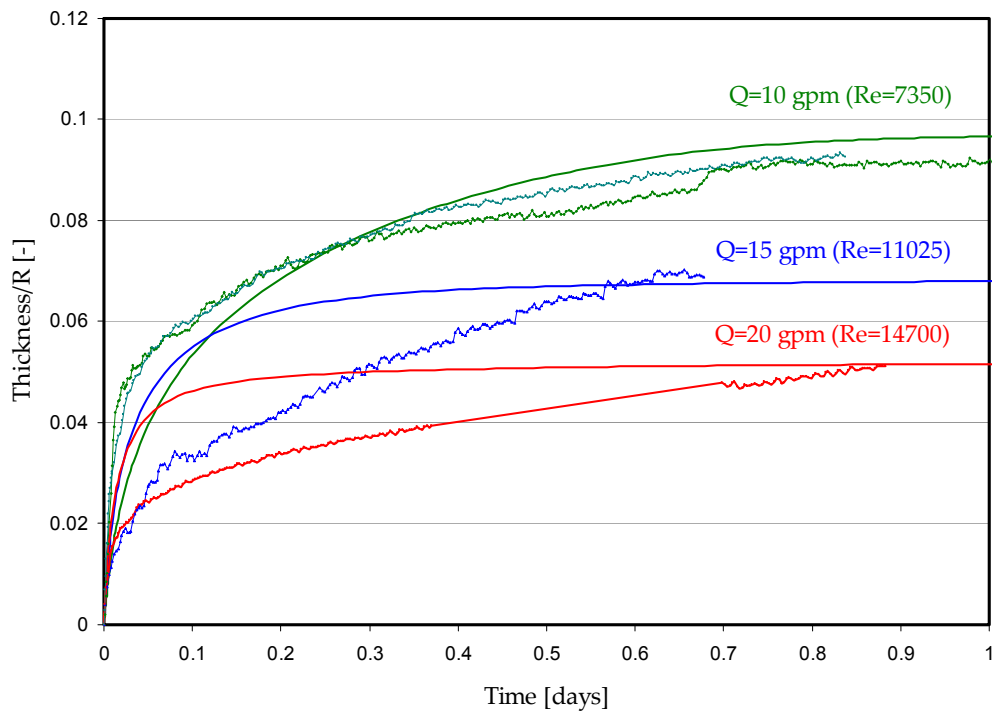


Figure 4.12: Comparison between model prediction and flow loop experiments for various flow rates (Q=10gpm, 15gpm and 20gpm).

Large-scale flow loop results (Lund, 1998)

We now apply the computational wax deposition model to a large scale turbulent flow loop experiments (Lund, 1998). Unlike the lab-scale flow loop systems, the bulk temperature of the large scale flow loop changes with respect to the axial location as is the case in field pipelines. This application is meaningful because large scale flow loop experiments help make the transition from lab scale experiments to field scale pipeline systems. Furthermore, unlike the lab-scale tests discussed in the previous sections, the sample oil used in this case study is not a model wax-oil but a waxy crude oil (Mobil oil corporation's South Pelto crude oil). The test section of the flow loop consists of 50m U-shaped pipe inside of a PVC jacket with inside diameter of 10.2 cm. The temperature difference between the inlet crude oil and the inlet coolant flow was 25°C. Table 4.1 summarizes the operating conditions used for the flow loop test (Lund, 1998).

Table 4.1. Input parameters for the baseline case TU flow loop calculation

ID (cm)	Length (m)	Flow Rate (BOPD)	T_{bulk} (°C)	C_b (%)	Coolant heat transfer coefficient, h_o (W/m ² K)	Time (hours)
4.36	50	1,500	40.6	5	810	24

Figure 4.13 shows the growth of the deposit thickness as a function of time. One can observe the computational wax deposition model results developed in this study match the experiments of Lund (1998). The overprediction of the Chilton-Colburn analogy and the underprediction of the Solubility method are also shown in Figure 4.13. Figure 4.14 compares the experimental results and theoretical predictions of wax fraction (aging) in the deposit after a 24 hours test run.

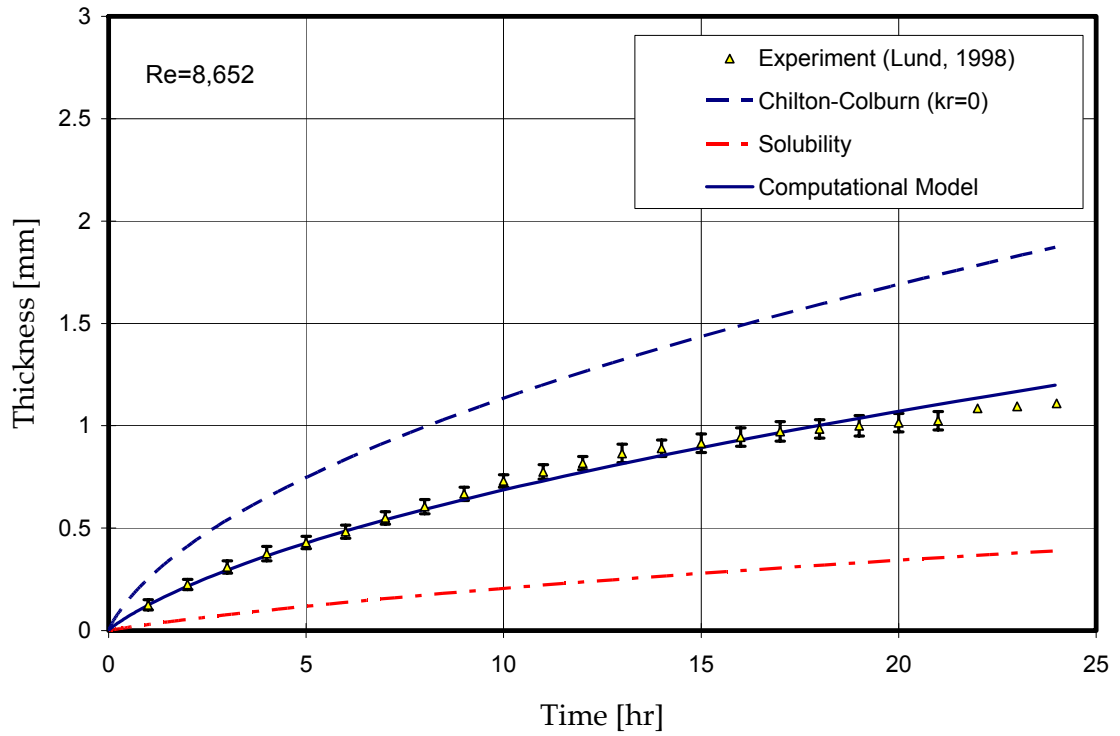


Figure 4.13: Deposit thickness versus time under turbulent flow. Theoretical predictions with the Chilton-Colburn analogy, the solubility method (Venkatesan and Fogler, 2004) and the theoretical model with precipitation kinetics.

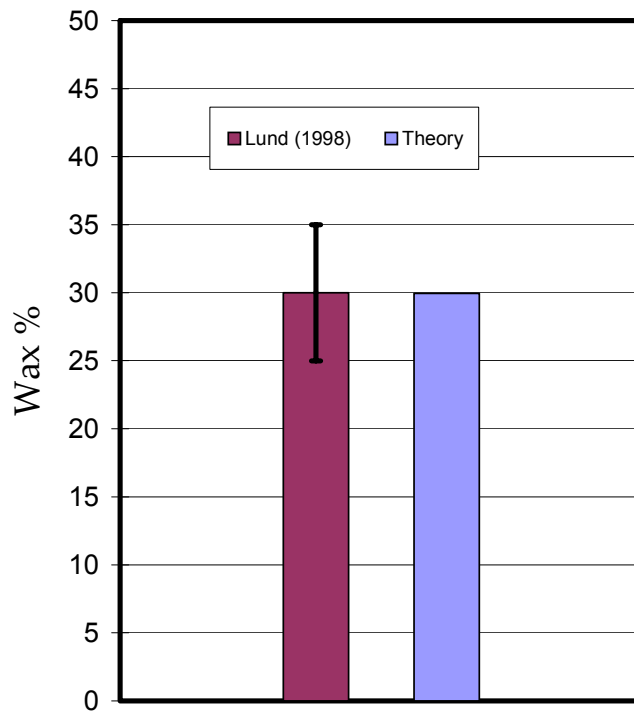


Figure 4.14: Wax % in the deposit after 24 hours (Lund, 1998).

Field pipeline results

The radial thermal gradient in the flow loop experiments is generally much greater than that of the field situation because the field pipelines are insulated to avoid wax deposition. In the flow loop systems there is no designated insulation between the oil flow and coolant flow in order to minimize the experimental time (i.e. several days at most). Therefore, in the flow loop systems, the internal thermal resistance ($1/h_i$) is most important than the external thermal resistance ($1/h_o$). On the contrary, in the field pipeline systems the external thermal resistance is dominant due to insulation and low external convective heat transfer rate in the ocean floor. Consequently the wax deposition modeling for the field pipeline system requires additional boundary conditions for the insulation and for the external convective heat transfer as shown in equation (4.25) and Figure 4.15.

$$-k_{ins} \left. \frac{\partial T}{\partial r} \right|_{insulation} = h_o (T - T_{sea}) \quad (4.25)$$

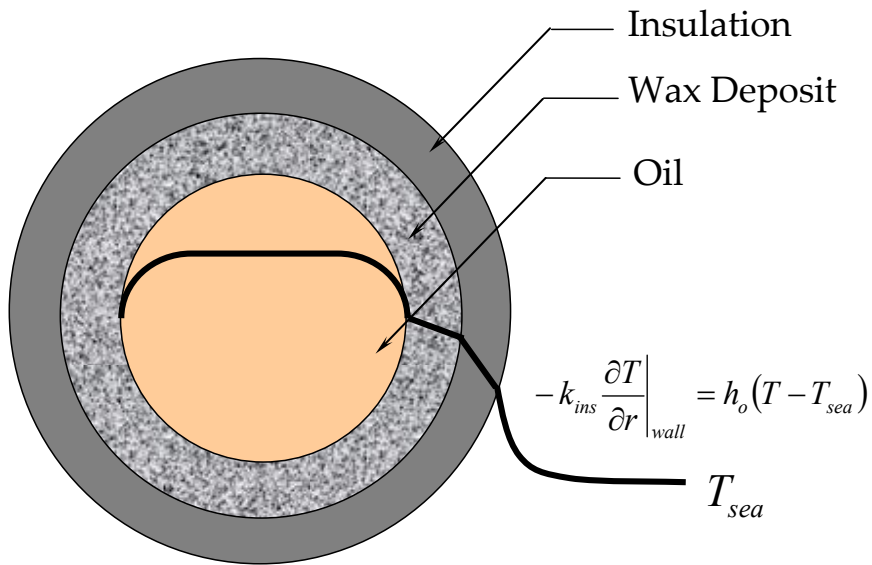


Figure 4.15: Sketch of radial temperature profile in a field pipeline.

Table 4.2 summarizes the input parameters used for the baseline calculation of the wax deposition in a field pipeline.

Table 4.2. Input parameters for the baseline case for a field scale pipeline system

ID (m)	Length (km)	Flow Rate (BOPD)	T_{bulk} ($^{\circ}C$)	T_{sea} ($^{\circ}C$)	C_B (%)	Insulation (cm)	h_o (W/m^2K)	Time (months)
0.35	70	25,000	70	4	5	2.54	50	2

The computational model requires pipe dimensions (e.g. diameter, length, and insulation type, and external convective heat transfer coefficient), operating conditions (e.g. flow rate, ocean floor temperature and pipe inlet temperature), and oil properties (e.g. wax %, density, heat capacity, solubility, and viscosity) as input variables. In this case study, physical properties of the South Pelto crude oil given in Lund (1998) are used.

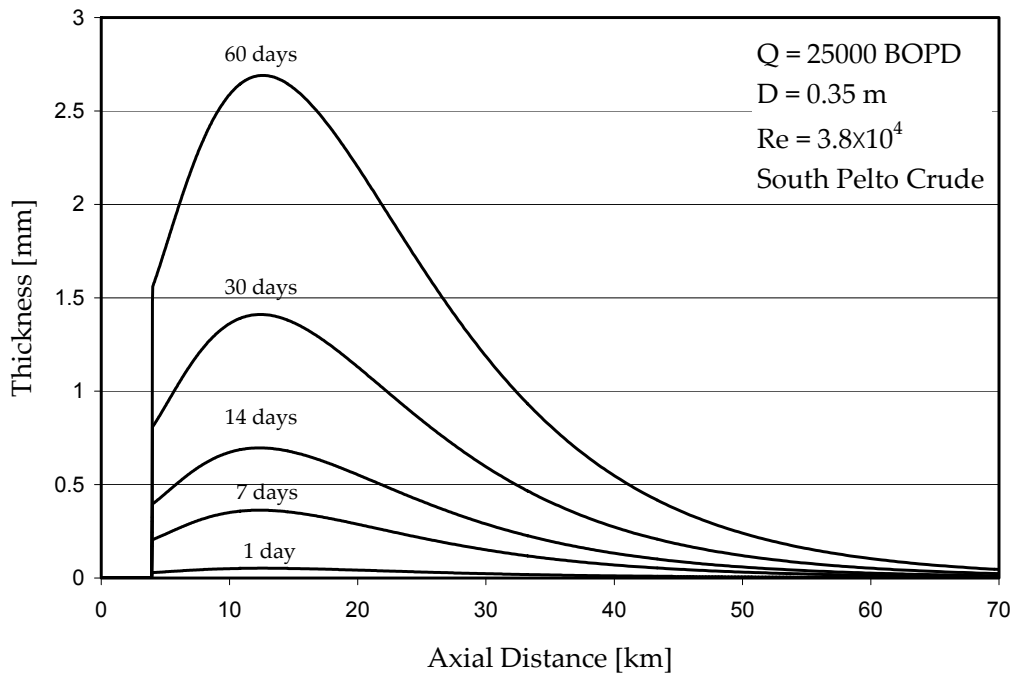


Figure 4.16: Growth of wax deposit for the baseline case at $t = 1$ day, 7 days, 14 days, 30 days and 60 days.

Figure 4.16 shows the axial profile of the deposit thickness for the baseline case for continuous production over a two month period. If the inner wall temperature is higher than the cloud point temperature (0-4 km in Figure 4.16), no wax deposition occurs. From 4 km to 12 km, there is no bulk precipitation because the bulk temperature is higher than the cloud point temperature. Wax deposition occurs in the boundary layer as the inner wall temperature is lower than the cloud point temperature. Hence the temperature difference between the bulk and inner wall makes wax deposit increase rapidly in this portion of the pipeline because the convective mass transfer rate term, $k_M (C_b - C_{ws}(T_i))$ is high. At axial distances greater than 12 km, both the bulk temperature and wall temperature are lower than the cloud point temperature and as a result the bulk precipitation begins and continues to precipitate as bulk temperature decreases further in downstream of the pipeline. Once wax molecules precipitated out in the bulk phase because the solubility limit is below the cloud point temperature, they do not contribute to either the growth or aging of the wax gel (Singh et al., 2000).

Figure 4.17 shows the axial profile of the wax fraction in the deposit. As given in equation (4.3), aging of wax deposit is directly proportional to $(dC_{ws} / dT) \times (dT / dr)$ at the interface. Therefore the wax fraction is maximum near the pipeline inlet where radial temperature gradient is a maximum. The wax gel strength strongly depends on the wax fraction of the gel (Lee et al., 2007) and therefore, both the gel thickness and wax fraction profile are important for the remediation of the gel deposit.

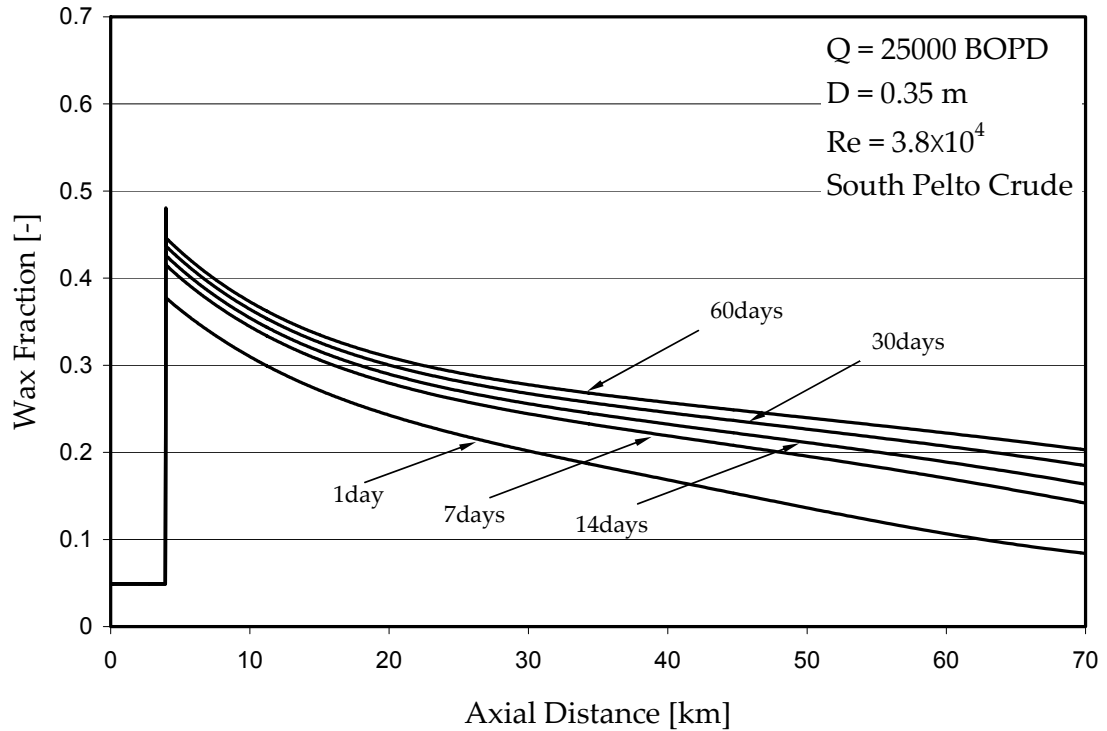


Figure 4.17: Aging of wax deposit for the baseline case.

Effect of solubility on wax deposition in field pipelines

Because the solubility of waxes is a function of temperature, it plays an important role in wax deposition in field scale pipelines where the temperature of oil changes significantly. In this section, the effect of solubility on the wax deposition in field pipelines is investigated by comparing wax deposition with three oils: South Pelto crude oil (5 wt% wax, $T_{\text{cloud}} = 49\text{ }^{\circ}\text{C}$), Garden Banks condensates (3 wt% wax, $T_{\text{cloud}} = 34.4\text{ }^{\circ}\text{C}$) and the model oil described in section 3.2 (3 wt% wax, $T_{\text{cloud}} = 23.1\text{ }^{\circ}\text{C}$). Figure 4.18 shows that the solubility curves of two crude oils are concave downward while the solubility curve for the model oil is concave upward (Venkatesan and Fogler, 2004). Hence the solubility of model oil rapidly decreases at the cloud point temperature

whereas the solubility of the crude oils gradually decreases at the cloud point temperature.

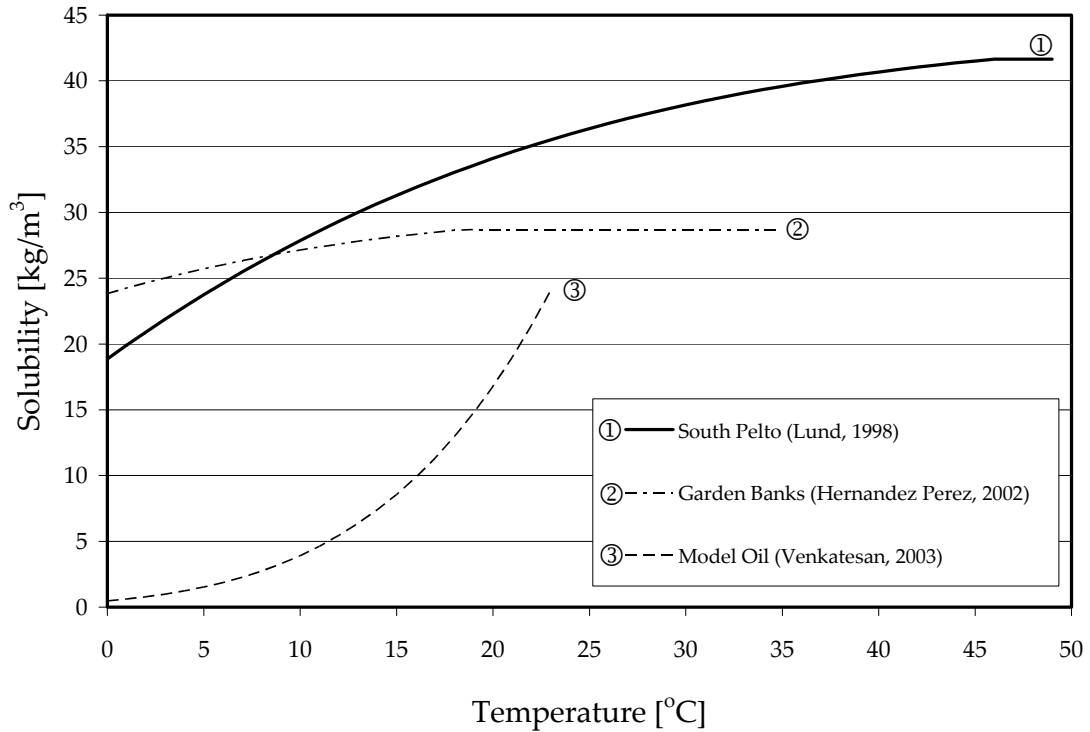


Figure 4.18: Solubility as a function of temperature for South Pelto crude oil (Lund, 1998), Garden Banks condensates (Hernandez Perez, 2002) and model oil (Venkatesan, 2003).

Further, the solubility of the model oil decreases to approximately zero at the sea water temperature (4 °C), whereas most wax molecules are still soluble in the crude oil even at 0 °C. This difference in solubility curves between the model oil and crude oils attributed to the differences in the n-paraffin carbon number distributions between the model oil (Gaussian distribution) and the real crude oils (decreasing exponential n-paraffin distribution) (Paso, 2005).

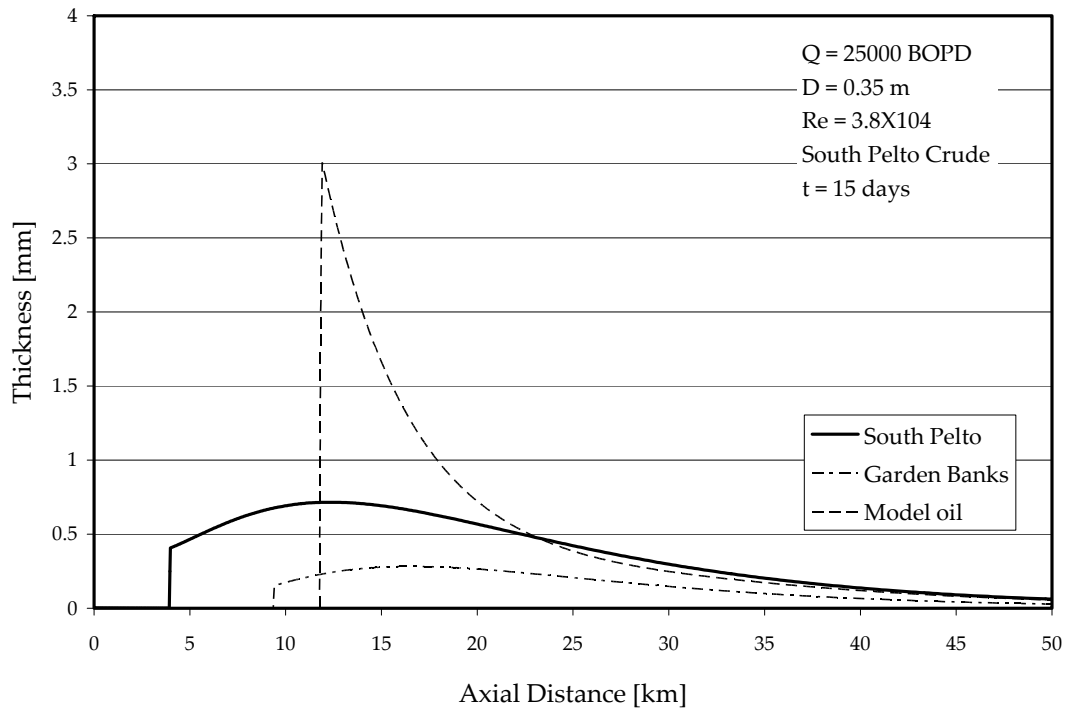


Figure 4.19: Axial thickness profiles for various oils. The input parameters used for these calculations of the wax deposition in a field pipeline are same as that of the baseline case as summarized in Table 4.2.

Figure 4.19 shows the axial profiles of the deposit thickness for three different oils after 15 days of continuous production. The different axial starting locations of wax deposit are due to the differences in the cloud point temperatures of the oils. Unlike the South Pelto oil and Garden Banks condensates, the wax deposition prediction for the model oil results in a high peak. The existence of the high peak for the model oil system is due to the temperature dependency of the solubility curve as shown in Figure 4.18. When the bulk temperature is higher than the cloud point temperature and the inner wall temperature is below the cloud point temperature, the difference between the bulk concentration and the concentration (or solubility) at the oil-deposit interface for the case of the model oil is greater than that of the crude oils because of the concave upward solubility curve. The concentration difference between the bulk and interface is the

driving force of the growth of wax deposit (i.e. convective mass transfer rate, $k_M(C_b - C_{ws}(T_i))$). As the bulk oil temperature further decreases below the cloud point temperature, wax molecules in the bulk phase start to precipitate, and the driving force (i.e., $k_M(C_b - C_{ws}(T_i))$) rapidly decreases to the deposit-oil interface concentration.

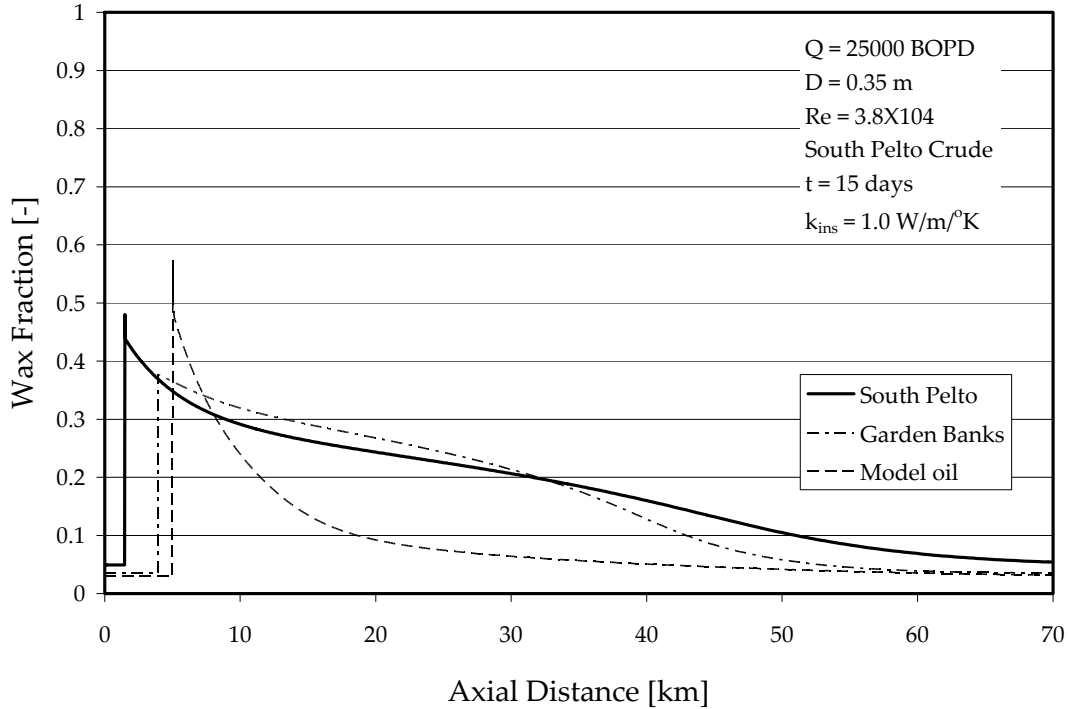


Figure 4.20: Axial wax fraction profiles for various oils. The input parameters used for these calculations of the wax deposition in a field pipeline are same as that of the baseline case as summarized in Table 4.2.

Figure 4.20 shows the axial profiles of wax fraction in the deposit for three oils. The wax fraction for the case of the model oil rapidly decreases with respect to axial distance due to the decrease of both the tangent of the solubility curve (dC_{ws} / dT) and the radial temperature gradient (dT / dr) at the oil-deposit interface. As aging of wax deposit is directly proportional to $(dC_{ws} / dT) \times (dT / dr)$ at the interface between the oil and the deposit, the aging rate is at a maximum near the pipeline inlet where the radial

temperature gradient is at a maximum. Unlike the model oil, the tangent of the solubility of crude oils increases as the temperature decreases and therefore the wax fraction in the deposit decreases more gradually than the model oil case.

Summary

In this research, a general wax deposition predictor was combined with fundamental heat and mass transfer analysis. The numerical solution of coupled heat and mass transport equations revealed that the convective mass transfer rate (i.e. the Sherwood number) can be significantly reduced by the precipitation of wax molecules in the turbulent boundary layer. Furthermore, the analysis showed that the computational model can be bounded by the solubility model (Venkatesan and Fogler, 2004) as the lower bound and the Chilton-Colburn analogy (Chilton and Colburn, 1934) as the upper bound. Comparing with the results of lab scale and large scale turbulent wax deposition experiments, this study also has revealed that to the wax deposition model with precipitation kinetics with the combined heat and mass transfer rate can successfully predict the thickness and aging of wax component in the deposit under various turbulent conditions.

Nomenclature

A_p	Surface area of a nucleus [m^2]
A_j^c	Defined in Eq. (4.15a) [s^{-1}]
A_j^T	Defined in Eq. (4.17a) [s^{-1}]
B_j^c	Defined in Eq. (4.15b) [s^{-1}]
B_j^T	Defined in Eq. (4.17b) [s^{-1}]
C	Wax concentration [kg/m^3]

C_b	Bulk concentration of wax [kg/m ³]
C_p	Heat capacity [J/kg/°C]
C_{wall}	Wax concentration, $= C_{ws}(T_{wall})$ [kg/m ³]
C_j^c	Defined in Eq. (4.15c) [s ⁻¹]
C_j^T	Defined in Eq. (4.17c) [s ⁻¹]
D_e	Effective diffusivity [m ² /s]
D_{wo}	Molecular diffusivity of wax in oil [m ² /s]
D_j^c	Defined in Eq. (4.15d) [kg/m ³ /s]
D_j^T	Defined in Eq. (4.17d) [°C/s]
d_p	Diameter of a nucleus [m]
\bar{F}_w	Wax fraction in the deposit [-]
h_i	Inner convective heat transfer coefficient [W/m ² /°C]
k	Thermal conductivity [W/m/°C]
k_d	Volume diffusion coefficient from bulk to the nucleus surface [m/s]
k_M	Inner convective mass transfer coefficient [m/s]
L	Pipe length [m]
$m_{deposit}$	Mass of the wax deposit [kg]
R	Radius of a pipe [m]
r	Radial coordinate [m]
r_i	Effective radius of a pipe [m]
T	Oil temperature [°C]
v_{avg}	Average velocity [m/s]
v_z	Axial velocity [m/s]
α	Aspect ratio of the wax crystals in the deposit (width to thickness) [-]
α_T	Thermal diffusivity $\frac{k}{\rho C_p}$ [m ² /s]

β	$\frac{k_r \Delta H_f}{\rho C_p}$ [(°C/s)/(kg/m ³)]
δ	$R - r_i(t)$ [m]
ρ	Density of oil [kg/m ³]
ρ_{gel}	Density of the wax deposit [kg/m ³]
ρ_n	Number density of nucleus [1/m ³]
ΔH_f	Heat of solidification of wax [J/kg]
ΔC	$C_b - C_{ws}(T_i)$ [kg/m ³]
ΔT	$T_b - T_i$ [°C]

Dimensionless Numbers

Le	Lewis number ($\equiv Sc / Pr$)
Nu	Nusselt number ($\equiv \frac{h_i(2r_i)}{k}$)
Pr	Prandtl number ($\equiv \nu / \alpha$)
Re	Reynolds number ($\equiv DV / \nu$)
Sc	Schmidt number ($\equiv \nu / D_{wo}$)
Sh	Sherwood number ($\equiv \frac{k_M(2r_i)}{D_{wo}}$)
$Sh_{solubility}$	Sherwood number obtained by solubility method (Equation (4.9))
Sh_p	Sherwood number at the surface of a nucleus (Equation (4.23))

References

- Aris, R., "On the Permeability of Membranes with Parallel but Interconnected Pathways," *Math. Biosci.*, **77**, 5 (1985).
- Armenante, P.M. and D.J. Kirwan, "Mass Transfer to Microparticles in Agitated Systems," *Chem. Eng. Sci.*, **44**, 2781 (1989).
- Bern, P. A., V.R. Withers, and J.R. Cairns, "Wax Deposition in Crude Oil Pipelines," Proc. Euro. Offshore Petrol. Conf. and Exhib., London, 571 (1980).
- Brown, T.S., V.G. Niesen, and D.D. Erickson, "Measurement and Prediction of the Kinetics of Paraffin Deposition," Proc. SPE Technical Conf. and Exhib., Houston, 353 (1993).
- Burger, E.D., T.K. Perkins, and J.H. Striegler, "Studies of Wax Deposition in the Trans Alaska Pipeline," *J. Pet. Tech.*, **33**, 1075 (1981).
- Chilton, T.H. and A.P. Colburn, "Mass Transfer (Absorption) Coefficients Prediction from Data on Heat Transfer and Fluid Friction," *Ind. Eng. Chem.*, **26**, 1183 (1934).
- Creek, J.L., H.J. Lund, J.P. Brill, and M. Volk, "Wax Deposition in Single Phase Flow," *Fluid Phase Equilibria*, **158**, 801(1999).
- Cussler, E.L., S.E. Hughes, W.J. Ward, and R. Aris, "Barrier Membranes," *J. Memb. Sci.*, **38**, 161 (1988).
- Deen, W.M., Analysis of Transport Phenomena, Oxford University Press (1998).
- Dirand, M., V. Chevallier, E. Provost, M. Bouroukba, and D. Petitjean, "Multicomponent Paraffin Waxes and Petroleum Solid Deposits: Structural and Thermodynamic State," *Fuel* **77**, 1253 (1998).
- Dirand, M., M. Bouroukba, V. Chevallier, D. Petitjean, E. Behar and V. Ruffier-Meray "Normal Alanes, Multialane Synthetic Model Mixtures, and Real Petroleum Waxes: Crystallographic Structures, Thermodynamic Properties, and Crystallization," *J. Chem. Eng. Data* **47**, 115-143 (2002).
- Falla, W.R., M. Mulski, and E.L. Cussler, "Estimating Diffusion through Flake-filled Membranes," *J. Memb. Sci.*, **119**, 129 (1996).
- Fogler, H.S., Elements of Chemical Reaction Engineering, Prentice Hall, 4th ed. (2006).
- Fung, G., W.P. Backhaus, S. McDaniel, and M. Erdogmus, "To Pig or Not To Pig: The Marlin Experience with Stuck Pig," Proc. of 2006 Offshore Technology Conference, 2006, Houston, TX.

- Hausen, H., "Darstellung des Wärmeüberganges in Rohren durch Verallgemeinerte Potenzbeziehungen," *VDI Z.*, **4**, 91 (1943).
- Hayduk, W. and B.S. Minhas (1982), "Correlations for Prediction of Molecular Diffusivities in Liquids," *Can. J. Chem. Eng.*, **60**, 295 (1982)
- Hernandez Perez, O., M.S. Thesis, University of Tulsa, 2002
- Lee, H.S., R. Venkatesan, and H.S. Fogler, "Development of a Wax Deposition Model based on Combined Convective Heat and Mass Transfer Analysis under Turbulent Conditions," Proc. 8th International Conference on Petroleum Phase behavior and Fouling, June 10-14, 2007, Pau, France
- Lee, H.S., P. Singh, W.H. Thomason, and H.S. Fogler, "Waxy Oil Gel Breaking Mechanisms: Adhesive versus Cohesive Failure," *Energy and Fuel*, (2007), accepted
- Lund, H.-J., M.S. Thesis, University of Tulsa, 1998
- Majeed, A., B. Bringedal, and S. Overa, "Model Calculates Wax Deposition for N. Sea Oils," *Oil Gas J.* **88**, 63 (1990).
- Marchisio, D.L., A.A. Barresi, and M. Garbero, "Nucleation, Growth, and Agglomeration in Barium Sulfate Turbulent Precipitation," *AIChE J.* **48**, 2039 (2002).
- Nguyen, A.D., H.S. Fogler, and C. Sumaeth, "Fused Chemical Reactions. 2. Encapsulation: Application to Remediation of Paraffin Plugged Pipelines," *Ind. Eng. Chem. Res.* **40**, 5058 (2001).
- Nguyen, A.D., M.A. Iwaniw, and H.S. Fogler "Kinetics and mechanism of the reaction between ammonium and nitrite ions: experimental and theoretical studies," *Chem. Eng. Sci.* **58**, 4351 (2003).
- Nguyen, A.D., H.S. Fogler, and C. Sumaeth, "Fused Chemical Reactions. 3. Controlled Release of a Catalyst To Control the Temperature Profile in Tubular Reactors," *Ind. Eng. Chem. Res.* **43**, 5862 (2004).
- Nguyen, A.D., and H.S. Fogler "Facilitated Diffusion in the Dissolution of Carboxylic Polymers," *AIChE J.* **51**, 415 (2005).
- Oosthuizen, P.H. and D. Naylor, *An Introduction to Convective Heat Transfer Analysis*, McGraw Hill, (1999).
- Paso, K., M. Senra, Y.-B. Yi, A.M. Sastry and H.S. Fogler, "Paraffin Polydispersity Facilitates Mechanical Gelation," *Ind. Eng. Chem. Res.* **44**, 7242 (2005).

- Ribeiro, F.S., P.R.S. Mendes, and S.L. Braga, "Obstruction of Pipelines due to Paraffin Deposition during the Flow of the Crude Oil," *Int. J. Heat Mass Transfer* **40**, 4319 (1997).
- Seider, E.N., and C.E. Tate, "Heat Transfer and Pressure Drop of Liquids in Tubes," *Ind. Eng. Chem.* **28**, 1429 (1936).
- Singh, P., and H.S. Fogler, "Fused chemical reactions: The Use of Dispersion to Delay Reaction Time in Tubular Reactors," *Ind. Eng. Chem. Res.* **37**, 2203 (1998).
- Singh P., R. Venkatesan, H.S. Fogler, and N.R. Nagarajan, "Formation and Aging of Incipient Thin Film Wax-oil Gels," *AIChE J.* **46**, 1059 (2000).
- Singh P., R. Venkatesan, H.S. Fogler, and N.R. Nagarajan, "Morphological Evolution of Thick Wax Deposits during Aging," *AIChE J.* **47**, 6 (2001).
- Svendsen, J.A., "Mathematical Modeling of Wax Deposition in Oil Pipeline Systems," *AIChE J.* **39**, 1377 (1993).
- Todi, S., Ph.D. Thesis, University of Utah, 2005
- Van Driest, E.R. "On Turbulent Flow near A Wall," *J. Aero. Sci.* **23**, 1007 (1956)
- Venkatesan, R., Ph.D. Thesis, University of Michigan, 2003
- Venkatesan, R. and H.S. Fogler, "Comments on Analogies for Correlated Heat and Mass Transfer in Turbulent Flow" *AIChE. J.* **50**, 1623 (2004).
- Venkatesan, R., N.R. Nagarajan, K. Paso, Y.-B. Yi, A.M. Sastry and H.S. Fogler, "The Strength of Paraffin Gels Formed under Static and Flow Conditions" *Chem. Eng. Sci.* **60**, 3587 (2005).

CHAPTER V

CONCLUSIONS

The objectives of the research presented in this dissertation were to establish a fundamental understanding of wax deposition and gelation phenomena and use this understanding to develop theoretical models to simulate both the wax deposition and gel breaking phenomena in subsea pipelines. This research has concluded that the gel failure strength measurement by the controlled stress rheometer can successfully predict the required gel breaking pressure of a gelled pipeline if the cooling rate is low and if the gel failure mechanism is adhesive failure. Also, a rigorous combined convective heat and mass transfer analysis including wax precipitation in the boundary layer proved that the convective mass transfer rate in wax deposition process is bounded by the solubility method (Venkatesan and Fogler, 2004) as the lower bound and the Chilton-Colburn analogy method (Chilton and Colburn, 1934) as the upper bound. The knowledge gained from this work can be used to forecast wax deposition in field pipelines and therefore, serve as a basis for the selection and designing of a proper wax remediation technique. The main conclusions drawn from this work are summarized below.

Gel Breaking Phenomena

In this research, we have investigated the gel breaking mechanism at various temperatures and cooling rates using a model pipeline, a controlled stress rheometer and a cross-polarized microscope. This study has revealed that the controlled stress rheometer

and classical restart pressure drop equation can successfully predict the required gel breaking pressure of a gelled pipeline if the cooling rate is low and the gel breaking occurs at the pipe wall (adhesive failure). Furthermore, we have experimentally shown that there exists a delineation point between cohesive and adhesive failures when the measured gel strength is plotted as a function of cooling rate. Using the controlled stress rheometer experiments and the cross-polarized microscope, this study has also investigated the possible reasons why there exists a delineation point between cohesive and adhesive failures. Based on the results of model pipeline experiments and compressibility of the wax-oil system, a theoretical model has been developed that can explain the gel breaking process in pipelines. The gel breaking model incorporates the pressure propagation phenomenon and can predict the required time to break the gel. These results can be utilized to predict the restart time and the restart pressure in field pipelines.

Wax Deposition Phenomena

In this research, a general wax deposition predictor combined with fundamental heat and mass transfer analysis has been developed. The numerical solution of coupled heat and mass transport equations revealed that the convective mass transfer rate (i.e. the Sherwood number) can be significantly reduced by the precipitation of wax molecules in the turbulent boundary layer. Furthermore, the results of the analysis proved that the convective mass transfer rate can be bounded by the solubility model (Venkatesan and Fogler, 2004) as the lower bound and the Chilton-Colburn analogy (Chilton and Colburn, 1934) as the upper bound. Comparing with the results of lab scale and large scale

turbulent wax deposition experiments, this study also has revealed that to the wax deposition model with precipitation kinetics with the combined heat and mass transfer rate can successfully predict the thickness and aging of wax component in the deposit under various turbulent conditions.

References

- Chilton, T.H. and A.P. Colburn, "Mass Transfer (Absorption) Coefficients Prediction from Data on Heat Transfer and Fluid Friction," *Ind. Eng. Chem.*, **26**, 1183 (1934).
- Lee, H.S., P. Singh, W.H. Thomason, and H.S. Fogler, "Waxy Oil Gel Breaking Mechanisms: Adhesive versus Cohesive Failure," *Energy and Fuel*, (2007), accepted.
- Venkatesan, R. and H.S. Fogler, "Comments on Analogies for Correlated Heat and Mass Transfer in Turbulent Flow" *AIChE. J.*, **50**, 1623 (2004).

CHAPTER VI

FUTURE WORK

The research described in this thesis points to several topics for future research. In this chapter, five significant problems are identified for extending the results of this research:

1. Single Phase Wax Deposition under Low Heat Flux Conditions
2. Multiphase Wax Deposition Experiments and Modeling
3. Impact of Wax Inhibitors on Paraffin Precipitation Kinetics
4. Impact of Surface Roughness on Wax-Oil Gel Breaking Mechanism
5. Restart of Non-uniformly Gelled Pipeline

A few specific directions are prescribed, and some expected results are described.

Single Phase Wax Deposition under Low Heat Flux Conditions

In Chapter IV, a new computational wax deposition model has been developed and used to predict various scales of laminar and turbulent flow loop experiments. However, there are some differences in wax deposition between even very large scale flow loop experiments and field scale pipelines because of some limitations that exist in flow loop experiments. For example, in order to minimize the experimental time, virtually all the flow loop experiments have been performed with higher thermal gradients than that of field situations. This high thermal gradient in the boundary layer results in a higher degree of supersaturation in the mass transfer boundary layer than seen

in the field. Thus, the precipitation kinetics proven to be successful in the flow loop systems may need to be adjusted to the field pipelines. Further, the crystal aspect ratio within the gel, α , in the current model may need to be confirmed for the low heat flux and turbulent flow regime found in field conditions. Therefore, a set of single phase flow loop experiments with low thermal gradient are proposed. As a result of this low heat flux, the flow loop experiments should be performed for a longer period of time (i.e. months scale) in order to obtain reproducible and reliable results and to check the capability of the computational wax deposition model for longer times. As shown in Table 6.1, the typical thickness of wax deposit with high heat flux is about 1-2 mm after 24 hours. Therefore, to perform a low heat flux (for example $\Delta T < 5^\circ\text{C}$) experiment expecting reproducible results, the expected running time would be 5 to 10 times longer.

Table 6.1: Single phase flow loop experimental conditions with a large scale flow loop system.

	T_{in} ($^\circ\text{C}$)	Re	ΔT ($^\circ\text{C}$)	Thickness @ 24hr (mm)
Matzain (1997)	55	12,403	40	0.5-0.6
Lund (1998)	40	8,000	25	1.7
Oris (2002)	40	11,000	25	1.3

Multiphase Wax Deposition Experiments and Modeling

The next major challenge after predicting wax deposition in single phase flow as described in Chapter IV is the predicting wax deposition in multiphase flow. Flow in subsea pipelines typically involves crude oil, water and gas. In these cases, single-phase models are inadequate to model multiphase systems because they do not account for the effects of the water or gas phases. On the other hand, advances in the understanding of

the wax deposition mechanism and multiphase flow have now made the study of multiphase wax deposition feasible. Thus, it is necessary and practical to study modeling of multiphase wax deposition to learn the fundamentals of this issue and to optimize corrective methods through the fruit of modeling.

Despite great interest in multiphase wax deposition, limited studies have been completed in the last few decades. The first attempt to study wax deposition in gas/oil flow was done by Apte et al. (2001) and Matzain et al. (2002). In their study, several flow regimes for gas/oil flow were observed including stratified flow, gas-centered annular flow, intermittent flow and dispersed gas bubble flow. Wax deposition thicknesses under these flow regimes were measured and a model was established to predict the deposition process. It was believed that the wax deposition is highly flow regime dependent, which is greatly different from single phase oil flow.

However, there are several limitations to the experiments and modeling in their work. First, the heat-transfer method used to measure deposition thickness is inadequate for multiphase testing because of the difficulty in identifying a heat transfer coefficient of the gas/oil fluid mixture (Chen et al., 1997). Second, the gas/oil fluid was treated as one phase in modeling wax deposition where one heat transfer coefficient was used to describe the heat transfer characteristics of the gas/oil mixture. As a result, the original model deviated dramatically from the experimental data. In order to fix this problem, several material properties were tuned without any convincing physical explanations or ability of applying these parameters to other situations. However, even after tuning these properties, the model could only predict the initial build up of the deposit. The computational wax deposition model developed in Chapter IV would be a useful starting

point to overcome these limitations of earlier models because the computational model directly calculates local heat and mass transfer rates without using any averaged (lumped) heat and mass transfer correlations.

The first multiphase flow studies will focus on water/oil flow in the different flow regimes: stratified flow, intermittent flow, dispersed phase flow and annular flow as shown in Figure 6.1. Modeling of the stratified flow regime requires large scale flow loop experiments to develop an experimental and theoretical description of the multiphase deposition process. Once the stratified flow analysis is completed, then wax deposition modeling will be extended in other flow regimes.

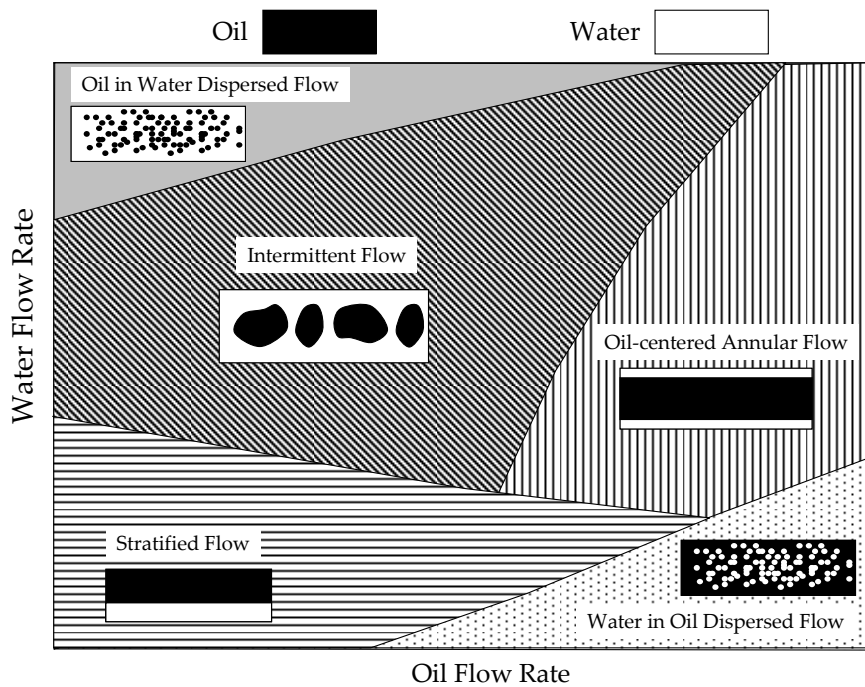


Figure 6.1: General flow regimes seen in water/oil flow for various flow rates.

Impact of Wax Inhibitors on Paraffin Precipitation Kinetics

In Chapter IV, the effects of precipitation kinetics on the mass transfer rate and ultimately on the wax deposition process were elucidated. The precipitation rates of waxes out of crude oils, especially in the presence of natural inhibitors such as

asphaltenes, can be much slower. Also, in the field situations, chemicals such as wax inhibitors or pour point depressants are frequently injected to suppress wax deposition. Thus, it is important to study the impact of wax inhibitors on the precipitation kinetics in order to model the deposition of such systems accurately.

Cross-polarized microscopy used in Chapter III is one way of measuring the precipitation rate. A crude oil or model oil sample can be cooled at various cooling rates and the rate of wax precipitation measured with or without shear. The morphology of the gel formed during the cooling process can be observed by constructing 3-D images (Venkatesan (2003) and Paso (2005)). As the cooling rate is increased, the apparent wax appearance temperature will decrease if the precipitation kinetics are slower than the cooling rates used. The sample can also be shock-cooled to a temperature below the WAT and the rate at which waxes precipitate can be measured to determine the kinetics.

DSC measurements of heat of crystallization and rheological measurements of the viscosity as a function of temperature under various cooling rates will also be useful tools to elucidate the precipitation rate.

Impact of Surface Roughness on Wax-Oil Gel Breaking Mechanism

In Chapter III, we show that there are two gel breaking mechanisms in a pipeline (cohesive and adhesive failures) and that a delineation point exists when the measured gel strength is plotted as a function of cooling rate. This delineation point between cohesive and adhesive failure would change if the surface roughness is changed. The adhesive strength will increase as the surface roughness increases because of the greater contact area between wax-oil gel and the wall. The predicted trends with the rougher surfaces are

shown with a dashed line in Figure 6.1. A further increase in roughness ($> 250 \mu\text{m}$) would prevent any adhesive failure caused by slip at the surface. The failure would then only be cohesive. Typical pipeline roughness varies from 15 to 90 μm , depending on the pipe type. Consequently, the goal of this work is to study the gel adhesive and cohesive characteristics for different surface roughness. To accomplish this, sandpaper with different roughness will be attached to the rheometer plate. After measuring yield stress using the controlled stress rheometer, the yield stress will be compared with gel breaking experiments described in Chapter III with various surface coating materials (e.g. Teflon) to study the influence of surface roughness.

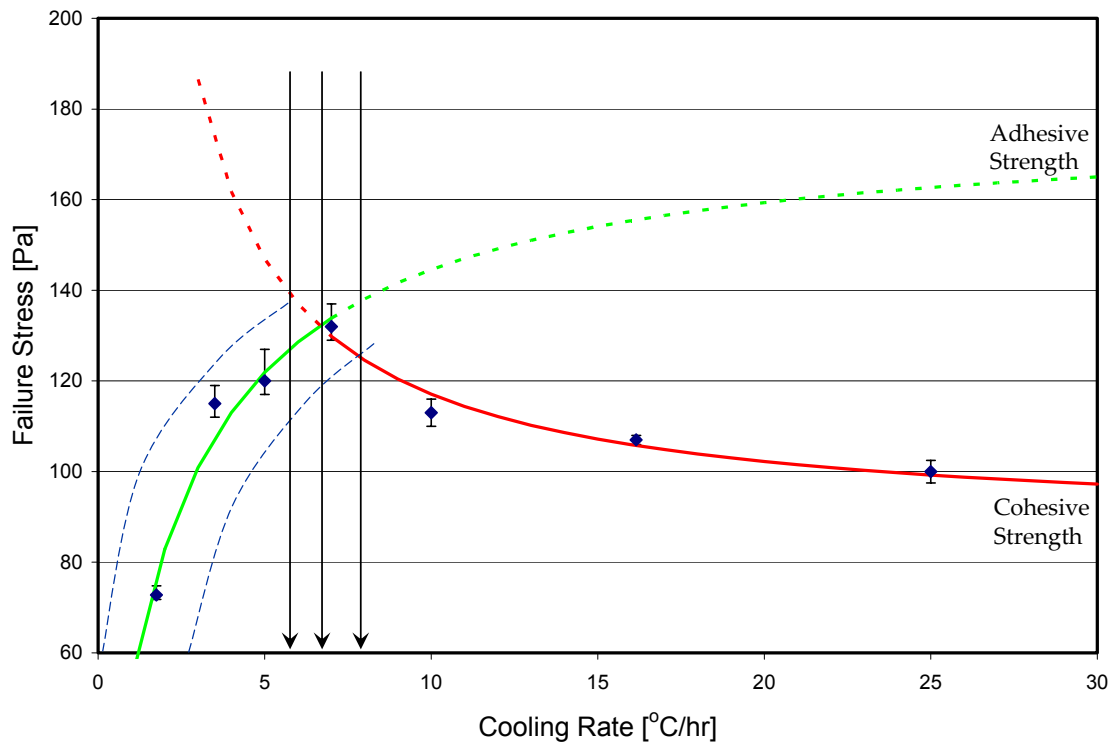


Figure 6.2: Preliminary sketch of effect surface roughness on the delineation point.

Restart of Non-uniformly Gelled Pipeline

Wax-oil gel has radial and axial variations in the thermal and shear history experienced in the field pipelines. During a shutdown, the oil in the pipeline cools down from the pipe wall towards the centerline. As there is a temperature gradient during this cooling process, a concentration gradient is also established, similar to the scenario during deposition under flow conditions. The concentration gradient drives a diffusive flux of wax molecules towards the wall. As a result, the solid wax content of the final gel is higher near the pipe wall than near the center. Thus, the yield stress is not uniform across the cross section. The varying cooling rates across the cross section also contributes to this non-uniformity in yield stress. Consequently, a model that describes the cooling and gelation process needs to be developed in order to scale up the restart model accurately.

In spite of the importance of the research, very little scientific research on the modeling of gelation, under static conditions both experimentally and theoretically have been completed. The proposed model will be a modification of the flow deposition model developed earlier (Singh et al., 2000) and in this thesis. This model can be developed in conjunction with the computational model proposed earlier in Chapter IV. The outputs of the model would include the radial temperature and solid wax content distribution as a function of time. Rheological experiments can then be performed to study the yield stress of these gels as a function of the thermal history and wax content. Creep tests are recommended to study the yield stress. Incorporating these rheological results into the model will then provide the radial distribution of the yield stress. In order to predict the restart pressure from this yield stress distribution, auto-destruction and compression have

to be modeled as outlined by Verschuur et al. (1971). Thus, the aim of this work is to develop a model for the restart pressure in field scale pipelines as a function of several variables:

$$\Delta P_{restart}^{field-scale} = f(\tau_y, \text{cooling rate, compressibility, etc}) \quad (6.1)$$

An expected result of this work is that the breakage of the gel does not necessarily happen close to the pipe wall, although the shear stress exerted at the wall is the highest when applying the restart pressure. This phenomenon is due to the fact that the yield stress at the wall is also the highest. For very large diameter pipelines with ineffective insulation, the breakage is likely to occur at a radial location where the yield stress and the applied shear stress match. As a result, some gel may be left adhered onto the pipe wall if sufficient restart pressure is not applied. If there is a good insulation for small diameter pipelines, because of the low thermal gradient in the wax-oil gel, radial yield stress variation is negligible as is the case described in Chapter III.

References

- Apte, M.S., A. Matzain, H.-Q. Zhang, M. Volk, J.P. Brill, and J.L. Creek, "Investigation of Paraffin Deposition During Multiphase Flow in Pipelines and Wellbores - Part 2: Modeling", *J. of Energy Resources Tech.* **123**, 150 (2001)
- Bern, P.A., V.R. Withers, and J.R. Cairns, "Wax Deposition in Crude Oil Pipelines", Proceedings - European Offshore Petroleum Conference and Exhibition, London, (1980).
- Brauner, N., D.M. Maron, and J. Rovinsky, "Two-Fluid Model for Stratified Flows with Curved Interfaces", *Int. J. of Multiphase Flow* **24**, 975 (1998).
- Brown, T. S., V.G. Niesen, and D.D. Erickson, "Measurement and Prediction of the Kinetics of Paraffin Deposition", Proceedings - SPE Technical Conference and Exhibition, Houston, (1993).
- Chen, X.T.; T. Butler, M. Volk, and J.P. Brill, "Techniques for Measuring Wax Thickness during Single and Multiphase Flow", Proceedings - SPE Annual Technical Conference and Exhibition, Houston (1997).
- Joseph, D.D., and R. Bai, "Core Annular Flows", *Ann. Review of Fluid Mech.* **29**, 65 (1997).
- Lee, H.S., P. Singh, W.H. Thomason, and H.S. Fogler, "Waxy Oil Gel Breaking Mechanisms: Adhesive versus Cohesive Failure," *Energy and Fuel* (2007), accepted.
- Majeed, A., B. Bringedal, and S. Overa, "Model Calculates Wax Deposition for North Sea Oils", *Oil & Gas J.* **88**, 63 (1990).
- Matzain, A., M.S. Apte, H.-Q. Zhang, M. Volk, J.P. Brill, and J.L. Creek, "Investigation of Paraffin Deposition During Multiphase Flow in Pipelines and Wellbores - Part 1: Experiments", *J. of Energy Resources Tech.* **124**, 180 (2002)
- Paso, K., Ph.D. Thesis, University of Michigan 2005.
- Paso, K., M. Senra, Y.B. Yi, A.M. Sastry, and H.S. Fogler, "Paraffin Polydispersity Facilitates Mechanical Gelation", *Ind. Eng. Chem. Res.* **44**, 7242 (2005).
- Ribeiro, F.S., M. P.R.S. Mendes, and S.L. Braga, "Obstruction Of Pipelines Due To Paraffin Deposition During The Flow Of Crude Oils", *Int. J of Heat and Mass Transfer* **40**, 4319 (1997)

- Russel, T.M.F., and M.E. Charles, "The Effect of Less Viscous Fluid in the Laminar Flow of Two Immiscible Liquids", *The Canadian Journal of Chemical Engineering* **37**, 18 (1959)
- Sarica, C; Volk, M, Paraffin Deposition Research and Model Development, DOE Research Report Literature, Final Technical Report, (2004)
- Singh, P., and H.S. Fogler, "Fused chemical reactions: The Use of Dispersion to Delay Reaction Time in Tubular Reactors," *Ind. Eng. Chem. Res.* **37**, 2203 (1998).
- Singh, P., R. Venkatesan, H.S. Fogler, and N.R. Nagarajan, "Formation and Aging of Incipient Thin Film Wax-Oil Gels", *AIChE J.* **46**, 1059 (2000).
- Thomason, W.H., "Start-Up and Shut-in Issues for Subsea Production of High Paraffinic Crudes", 2000 Offshore Technology Conference, Houston, TX (2000).
- Venkatesan, R., Ph.D. Thesis, University of Michigan, 2003.
- Venkatesan, R., P. Singh, and H.S. Fogler, "Delineating the Pour Point and Gelation Temperature of Waxy Crude Oils", *SPE J.* **7(4)**, 349 (2002).
- Verschuur, E., A.P.D. Hartog, and C.M. Verheul, "Effect of Thermal Shrinkage and Compressibility on Yielding of Gelled Waxy Crude Oils in Pipelines", *J. Inst. of Pet.* **57(554)**, 131 (1971)
- Volk, M., and C. Sarica, "Paraffin Deposition Research and Model Development", DOE Research Report Literature, Semi-Annual Report (2003)

APPENDICES

APPENDIX A

CALCULATION OF THE EFFECTIVE DIFFUSIVITY OF WAX IN OIL

A wax deposit is not a pure solid phase but a gel-like mixture and acts as a porous medium. Therefore, in order to calculate the diffusion influx at the oil-deposit interface, a proper effective diffusivity must be used. The gel consists of wax crystallites trapping the oil in the gel. The wax molecules must diffuse around these crystallites and it diffuse through the gel. Diffusion in heterogeneous media (e.g. membrane wall, nano composite polymer wall and so on) can be predicted by Aris (1986)'s model using serial mass transfer resistances in a porous medium.

$$\begin{aligned}
 D_{eff} &= \frac{D_{wo}}{1 + R_2 + R_3 + R_4} \\
 &= \frac{D_{wo}}{1 + \frac{\alpha^2 F_w^2}{1 - F_w} + \frac{\alpha F_w}{\sigma} + \frac{4\alpha F_w}{\pi(1 - F_w)} \ln \left[\frac{\pi \alpha^2 F_w}{\sigma(1 - F_w)} \right]}
 \end{aligned} \tag{A.1}$$

where, F_w is the volume fraction ($\equiv (2d)^2 a / \langle (2d + s)^2 (a + b) \rangle$), $\alpha = d / a$, and $\sigma = s / a$. As given in Figure A.1, R_2 in the denominator is the resistance to diffusion of the tortuous path parallel to wax crystals (Platelets), R_3 is the resistance to diffusion of the slits path and R_4 is the constriction of the solute to pass into and out of the gel (Falla, W.R., M. Mulski, E.L. Cussler, "Estimating Diffusion through Flake-filled Membranes," *J. Membr. Sci.* **119**, 129 (1996)).

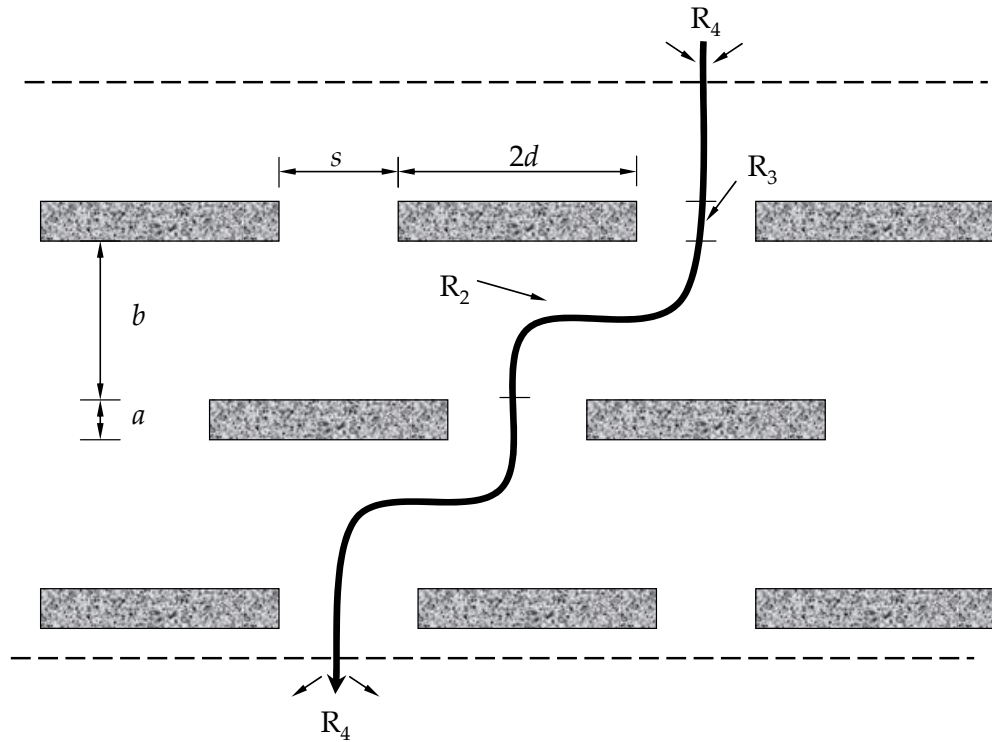


Figure A.1: Diffusion occurs through regularly spaced slits or pores.

If we neglect R_3 and R_4 the Aris model is converted to Cussler's effective diffusivity model (Cussler et al., (1988)). Figure A.2 compares two effective diffusivity models as a function of wax fraction. One observes that the models start to deviate significantly when the wax fraction is greater than 10%.

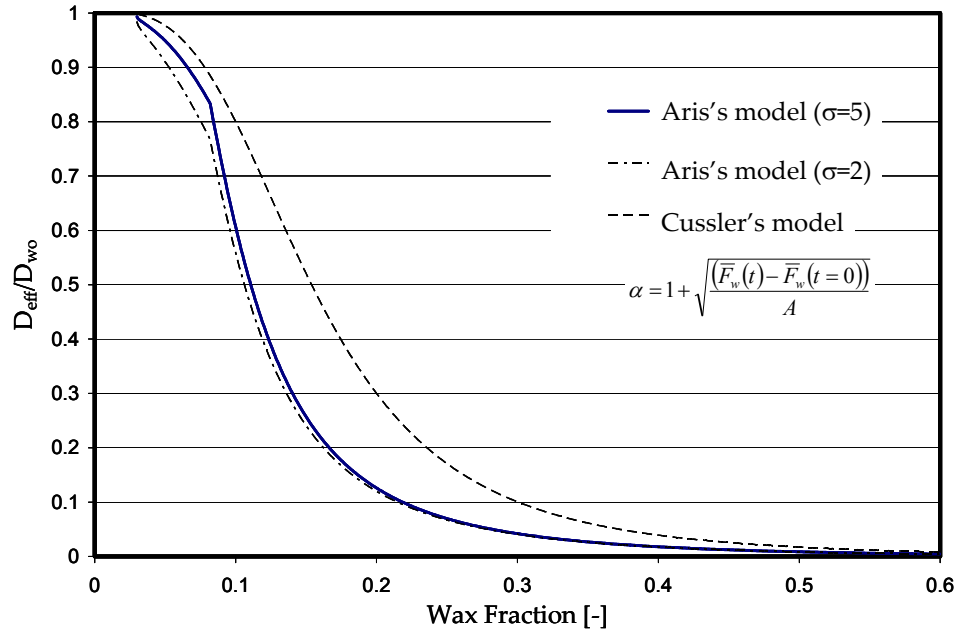


Figure A.2: Comparison between Aris's and Cussler's effective diffusivity model as a function of wax fraction in the deposit $A = \frac{\bar{F}_w(t_{final}) - \bar{F}_w(t=0)}{(\alpha_{final} - 1)^2} = 0.0045$.

APPENDIX B

TEMPERATURE DEPENDENCY OF THE PRECIPITATION RATE CONSTANT $k_r(T)$

A correlation proposed by Hayduk and Minhas (1982) is used to predict the molecular diffusivity of waxes in oil.

$$D_{wo} = 13.3 \times 10^{-12} \times \frac{T^{1.47} \mu^\gamma}{V_A^{0.71}} \frac{m^2}{s} \quad (\text{B.2})$$

where T is absolute temperature (K), μ is solvent viscosity (mPa.s) defined in (B.3), V_A is molar volume of the wax (cm^3/mol), and γ (dimensionless) is a function of V_A defined in (B.4)

$$\mu = \mu(T_{cloud}) \exp \left[\frac{E}{R} \left(\frac{1}{T_{cloud}} - \frac{1}{T} \right) \right] \quad (\text{B.3})$$

$$\gamma = \frac{10.2(\text{cm}^3/\text{mol})}{V_A} - 0.791 \quad (\text{B.4})$$

The average molecular weight of wax molecules used in this work is 400. The density of the wax is 0.9 gm/cm^3 . Hence, the molar volume of wax is $V_A = 430 \text{ cm}^3/\text{mol}$ and $\gamma = \frac{10.2(\text{cm}^3/\text{mol})}{430} - 0.791 = -0.767$.

As given in Equation (4.22), the precipitation rate constant can be obtained as,

$$k_r = k_d A_p \rho_n = \left(\frac{Sh_p \cdot D_{wo}}{d_p} \right) A_p \rho_n = D_{wo} \left(\frac{Sh_p}{d_p} \right) A_p \rho_n \quad (\text{B.5})$$

Equation (B.5) divided by the precipitation rate constant at the cloud point temperature yields,

$$\frac{k_r(T)}{k_r(T_{cloud})} = \frac{D_{wo}(T)}{D_{wo}(T_{cloud})} = \left(\frac{T}{T_{cloud}}\right)^{1.47} \left[\exp\left\{\frac{E}{R}\left(\frac{1}{T_{cloud}} - \frac{1}{T}\right)\right\}\right] \quad (\text{B.6})$$

$$\frac{k_r(T)}{k_r(T_{cloud})} = \left(\frac{T}{T_{cloud}}\right)^{1.47} \left[\exp\left\{\frac{\gamma E}{R}\left(\frac{1}{T_{cloud}} - \frac{1}{T}\right)\right\}\right] \quad (\text{B.7})$$

$$\ln\left[\frac{k_r(T)}{k_r(T_{cloud})}\right] = 1.47 \ln\left(\frac{T}{T_{cloud}}\right) + \left\{\frac{\gamma E}{R}\left(\frac{1}{T_{cloud}} - \frac{1}{T}\right)\right\} \quad (\text{B.8})$$

Figures B.1 and B.2 show the temperature dependency of the precipitation rate constant.

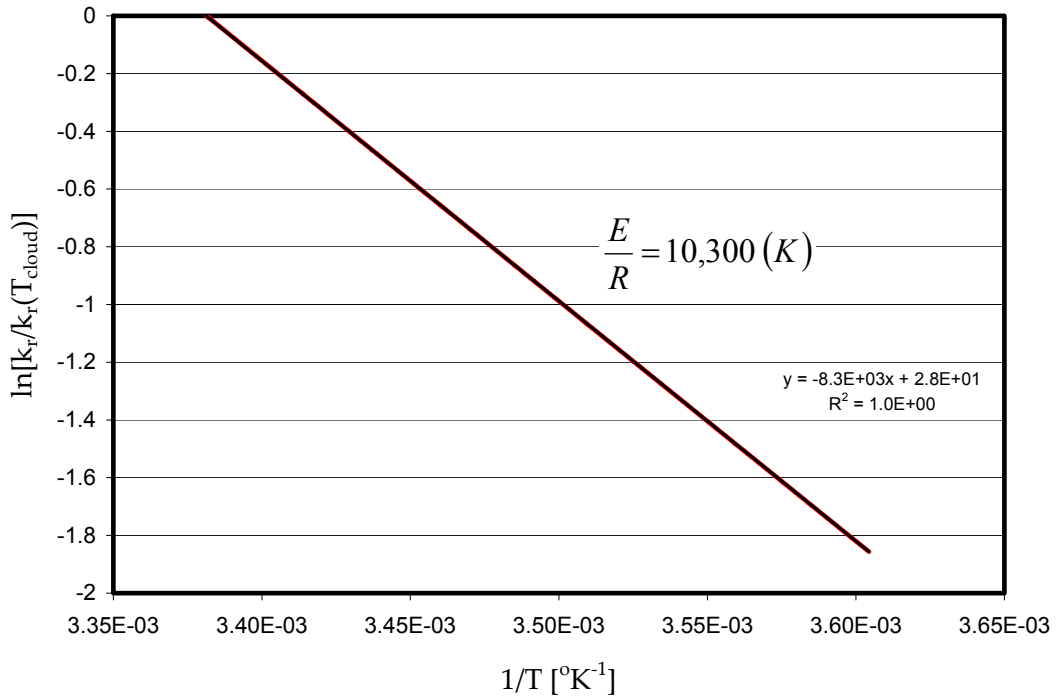


Figure B.1: The precipitation rate constant as a function of temperature,

$$\ln\left[\frac{k_r(T)}{k_r(T_{cloud})}\right] \text{ vs. } 1/T$$

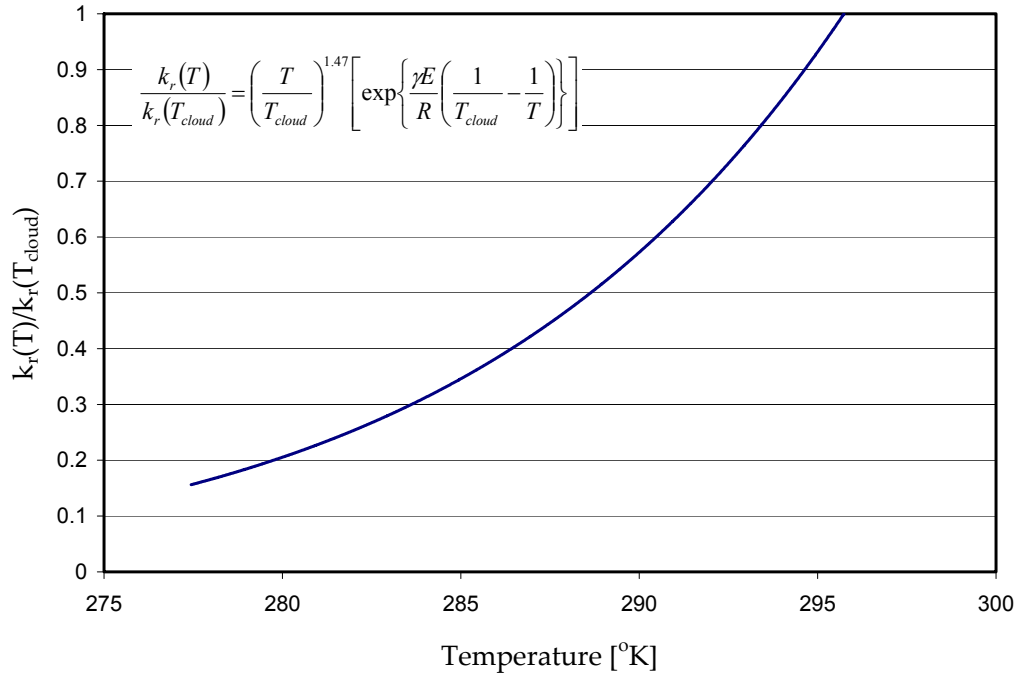


Figure B.2: The precipitation rate constant as a function of temperature,

$$\frac{k_r(T)}{k_r(T_{cloud})} \text{ vs. } T.$$

APPENDIX C

CALCULATION OF THE CRITICAL NUCLEUS SIZE

In this section, we calculate the critical nucleus size that are used to estimate a theoretical range of precipitation rate constant, k_p . The critical nucleation state is an unstable equilibrium, i.e., crystals smaller than the critical size dissolve. Gibbs free energy change is maximum at the critical nucleus size with respect to the number of wax molecules, g .

$$\frac{\partial(\Delta G / kT)}{\partial g} = 0 = \frac{2}{3} g^{-1/3} \theta - \ln S \quad (C.1)$$

where $\theta = \frac{\sigma_f s_1}{kT}$, σ_f is the surface tension between wax and oil (dyne/cm), S is the degree of supersaturation, and s_1 is the surface of wax molecule (cm^2). By rearranging equation (C.1), we can get the number of wax molecules in a critical nucleus for the case of wax deposition model for Venkatesan (2003)'s flow loop experiments.

$$\begin{aligned} g^* \equiv n^* &= \left(\frac{2}{3} \frac{\theta}{\ln S} \right)^3 \\ &= \left(\frac{2}{3} \frac{\theta}{\ln((C - C_{ws})/C_{ws})} \right)^3 \\ &= \left(\frac{2}{3} \frac{7.07}{\ln(5)} \right)^3 = 25.07 \end{aligned} \quad (C.2)$$

From equation (C.2), we can calculate the critical nucleus size as,

$$d_p = (g^*)^{1/3} d_1 = (25.07)^{1/3} 4.2 \times 10^{-3} \mu\text{m} = 0.0123 \mu\text{m} \quad (C.3)$$

Average end-to-end distance of an n-Alkane molecule used in this calculation is $d_1 = 42 \text{ \AA}$ (Dirand *et al.*, 2002). By using equation (C.3), mass of a critical nucleus can be calculated as follows.

$$\begin{aligned} m_p &= \frac{\pi}{6} d_p^3 \rho_{wax} = \frac{\pi}{6} (1.23 \times 10^{-8} \text{ m})^3 (880 \text{ kg} / \text{ m}^3) \\ &= 8.56 \times 10^{-22} \text{ kg} / \text{ particle} \end{aligned} \tag{C.4}$$

APPENDIX D

THE PRECIPITATION RATE CONSTANT AT THE CLOUD POINT TEMPERATURE

In this section we discuss the precipitation rate constant at the cloud point temperature, $k_r(T_{cloud})$ used in the improved wax prediction model. By providing two limiting cases that give maximum and minimum of number density, we show the number density back calculated from $k_r(T_{cloud})$ based on wax flow loop experiments can be bounded by two limiting cases.

(1) Maximum number density

Maximum possible number density is obtained with the assumption that all the supersaturated wax molecules precipitate with the critical nucleus size. In other words, there are no extra wax molecules remaining in the liquid phase besides the solubility limit.

$$\begin{aligned}\rho_n &= \frac{N}{V} = \frac{C - C_{ws}}{m_p} = \frac{(25 - 5) \text{ kg} / \text{m}^3}{8.56 \times 10^{-22} \text{ kg} / \text{nucleus}} \\ &= 2.34 \times 10^{22} \text{ nucleus} / \text{m}^3\end{aligned}\tag{D.1}$$

(2) Minimum number density

Number density of wax crystals obtained from a microscopic observation shown in Figure D.1 (Venkatesan *et al.*, 2005) can give a lower bound because crystals in this case have grown up in the gel without shearing (i.e. molecular diffusion) and therefore the crystal size is about 1000 times bigger than the critical nucleus size.

$$\rho_n = \left(\frac{3\% \text{ wax}}{5\% \text{ wax}} \right) \left(\frac{\text{number of crystals}}{\text{Unit length}} \right) = \left(\frac{3}{5} \right) \left(\frac{11}{0.27 \text{ mm}} \right)^3$$

$$= 4.06 \times 10^{13} \text{ particle} / \text{m}^3$$

(D.2)

Note that a correction factor (3/5) is multiplied in Equation (D.2) in order to correct the difference of two wax concentrations-microscopic observation ($C_w=5\%$) and the wax flow loop test ($C_w=3\%$).

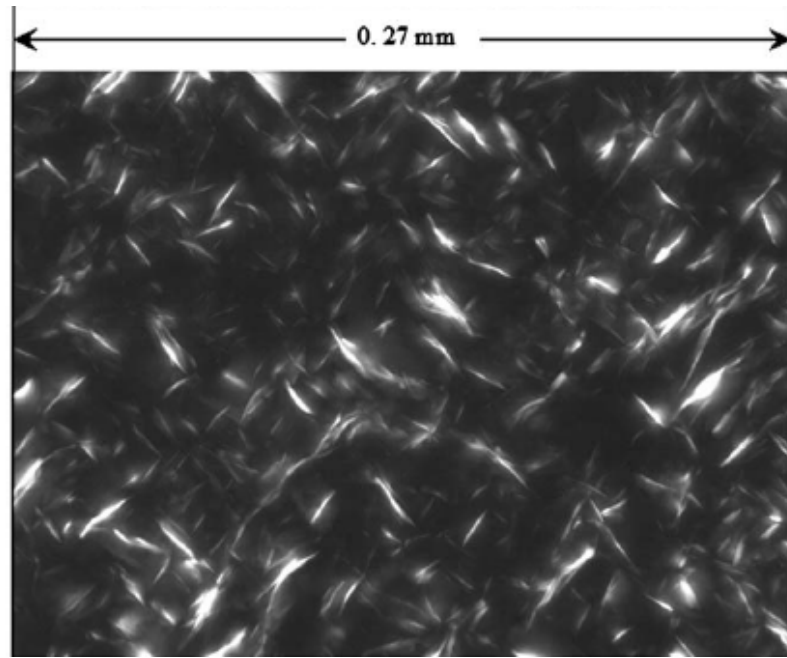


Figure D.1: Image of a 5% wax in oil mixture cooled down at the cooling rate of $6^\circ\text{C}/\text{min}$. The maximum crystal length is about $17 \mu\text{m}$ and average size is about $13.5 \mu\text{m}$ (Venkatesan *et al.*, 2005).

(3) Number density estimated from the back calculation

The precipitation rate constant at the cloud point temperature obtained from the back calculation using turbulent flow loop experiments (Venkatesan, 2003) is

$$k_r(T_{cloud}) = 0.754 \text{ s}^{-1}. \text{ By using Equations (4.22) and (4.24),}$$

$$\begin{aligned}
k_r(T_{cloud}) &= k_d A_p \rho_n = k_d (\pi d_p^2) \rho_n \\
&= \frac{Sh_p \cdot D_{wo}}{d_p} (\pi d_p^2) \rho_n = 0.754 \text{ s}^{-1}
\end{aligned}$$

$$\begin{aligned}
\rho_n &= \frac{k_r(T_{cloud})}{\frac{Sh_p \cdot D_{wo}}{d_p} (\pi d_p^2)} = \frac{0.754 \text{ s}^{-1}}{\frac{2 \cdot 10^{-11} (\text{m}^2 / \text{s})}{0.0123 \cdot 10^{-6} (\text{m})} \left(\pi (0.0123 \cdot 10^{-6})^2 (\text{m}^2) \right)} \\
&= 9.5 \times 10^{17} \text{ nucleus} / \text{m}^3 \tag{D.3}
\end{aligned}$$

By comparing Equations (D.1)-(D.3) one can see that the number density used in wax prediction (D.3) is in between the maximum (D.1) and minimum (D.2).

APPENDIX E

EFFECTS OF THERMAL INSULATION ON THE WAX DEPOSITION IN FIELD PIPELINES

In this appendix, we discuss the effects of thermal insulation of field pipelines on the wax deposition phenomena.

(1) Effect of insulation thickness

Figure E.1 shows the effect of the insulation thickness on wax deposition and Figure E.2 shows the corresponding bulk temperature profiles. As we decrease the insulation thickness (i.e., increase the heat transfer), the wax deposit thickness increases and initial location of wax deposit is closer to the inlet of the pipeline. From Figure E.2 one can see the bulk temperature decreases significantly as the insulation thickness decreases and as a result the initial location of wax deposit, axial profile and maximum thickness of wax deposit are significantly affected by the insulation thickness.

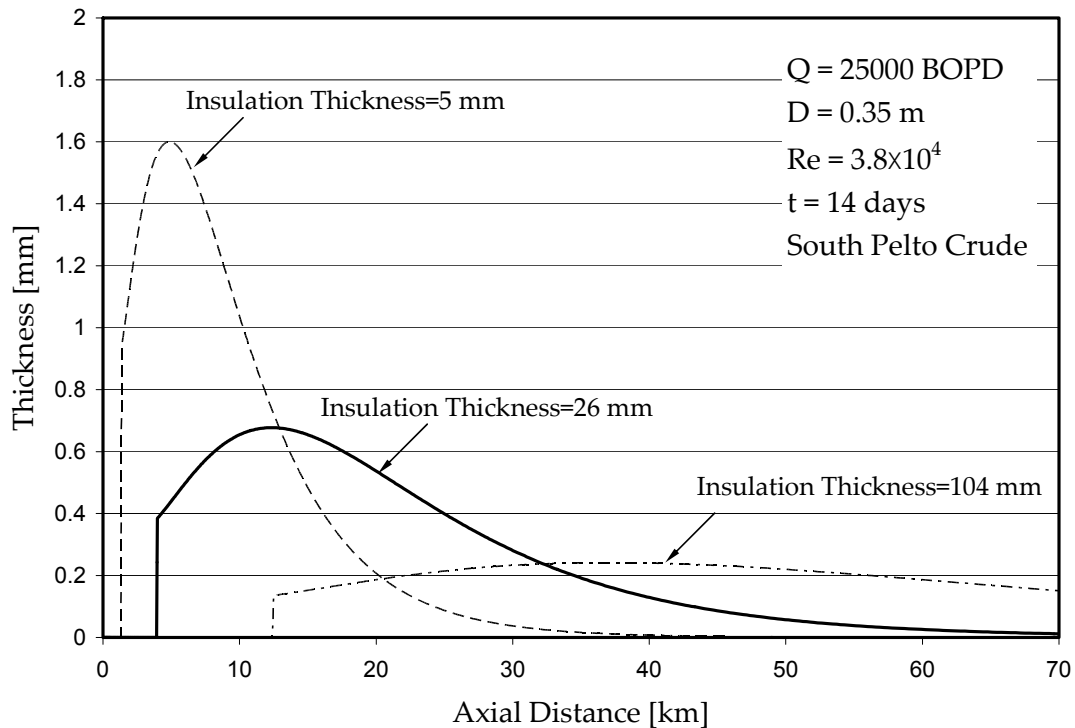


Figure E.1: Axial thickness profile with various insulation thicknesses.

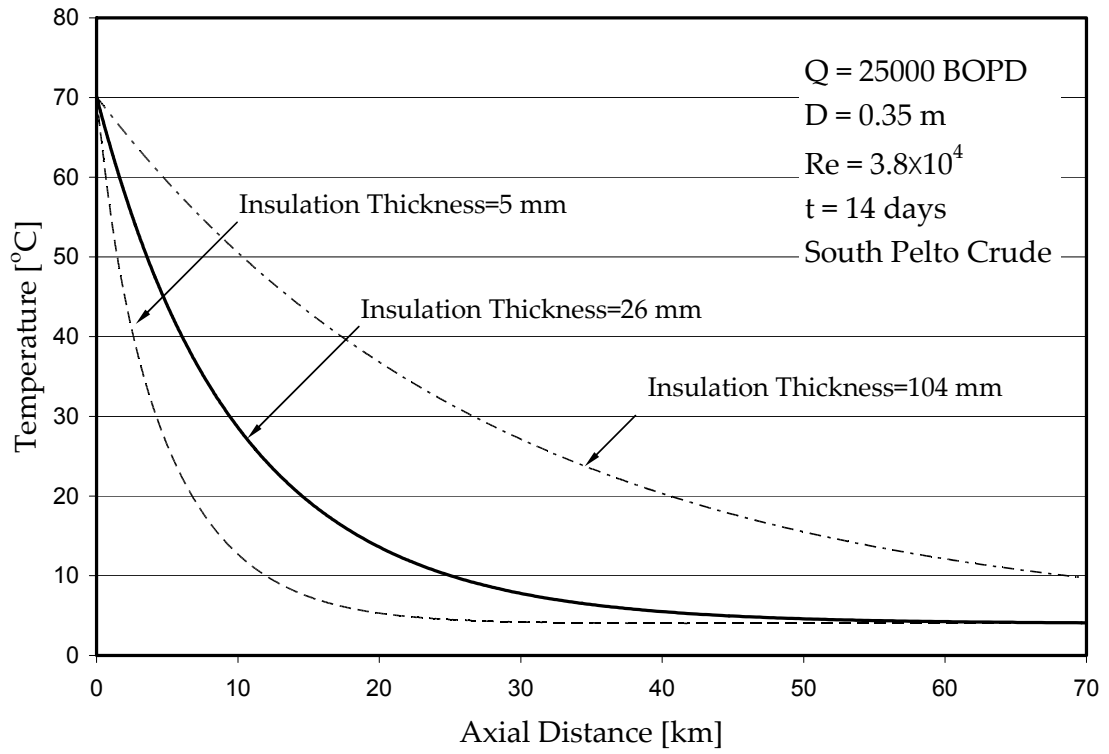


Figure E.2: Axial bulk temperature profile with various insulation thicknesses.

(2) Effect of thermal conductivity of insulation

Figure E.3 shows the axial temperature and thickness profiles for two different types of thermal insulations: a lower thermal conductive insulation ($k_{\text{ins}} = 0.29 \text{ W/m}^\circ\text{K}$) and a higher thermal conductive insulation ($k_{\text{ins}} = 1.0 \text{ W/m}^\circ\text{K}$). Wax deposition with the higher thermal conductive insulation results in narrower axial distribution than that of the lower conductive insulation. When the thermal conductivity of the insulation is high, the overall heat transfer rate increases and, thereby, the wax deposit is thicker and the bulk temperature decreases more rapidly than that of the lower conductive insulation. However, because the bulk temperature rapidly decreases below the cloud point temperature as shown in Figure E.3, the convective mass transfer rate $k_M(C - C_{\text{ws}}(T_i))$ decreases due to the decrease of bulk wax concentration resulting from the bulk precipitation, which does not contribute wax deposition.

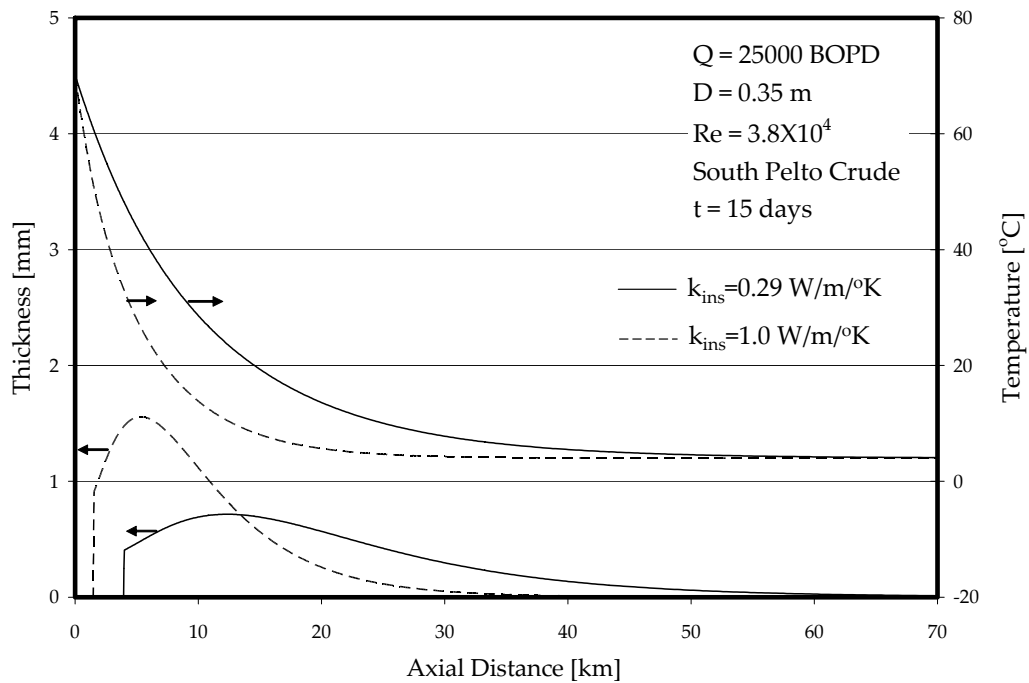


Figure E.3: Axial thickness and temperature profiles with two insulation conductivities ($k_{\text{ins}} = 0.29 \text{ W/m}^\circ\text{K}$ and $k_{\text{ins}} = 1.0 \text{ W/m}^\circ\text{K}$).